Noise Spectroscopy of Hybrid Perovskite Solar Cells

A Thesis

submitted in partial fulfillment for the degree of

MASTER OF SCIENCE

(ENGINEERING)

By

APOORVA SINGH

CHEMISTRY AND PHYSICS OF MATERIALS UNIT

JAWAHARLAL NEHRU CENTRE FOR ADVANCED SCIENTIFIC RESEARCH

(A DEEMED UNIVERSITY)

Bangalore – 560064, India

May 2017

Dedicated to my parents

Declaration

I hereby declare that the matter embodied in the thesis entitled ***"Noise Spectroscopy of Hybrid Perovskite Solar Cells"*** is the result of the work carried out by me under the supervision of Prof. K. S. Narayan, at Molecular Electronics Laboratory, in Chemistry and Physics of Materials Unit, Jawaharlal Nehru Centre for Advanced Scientific Research, Bangalore, India. It has not been submitted for the award of any degree or diploma or associateship of any other university or institute.

In keeping with the general practice in reporting scientific observations, due acknowledgement has been made whenever the work described is based on the findings of other investigators.

(Apoorva Singh)

JAWAHARLAL NEHRU CENTRE FOR ADVANCED SCIENTIFIC RESEARCH

Bangalore – 560064

K. S. NARAYAN
Professor
Dean (Research and Development)
Phone: +91 80 2208 2822/2548
E-mail: narayan@jncasr.ac.in
Fax: + 91 80 2208 2766

May 23th, 2017

Certificate

I hereby certify that the matter embodied in this thesis entitled *"**Noise Spectroscopy of Hybrid Perovskite Solar Cells**"* is the result of the work carried out by Mr. Apoorva Singh at the Molecular Electronics Laboratory, in Chemistry and Physics of Materials Unit, Jawaharlal Nehru Centre for Advanced Scientific Research, Bangalore, India, under my supervision and it has not been submitted for the award of any degree or diploma or associateship of any other university or institute.

Prof. K. S. Narayan

(Research supervisor)

Acknowledgements

This thesis is the outcome of the support and encouragement I have received both in the laboratory and outside. Many people have been instrumental in the process of production of this work. However, the guidance and learning received under my research supervisor are inexplicable. I would like to express my sincere gratitude to Professor K.S. Narayan for giving me the opportunity to carry out research in the Molecular Electronics Lab. He has not only suggested a very exciting research problem but also supported in all possible way in every aspect of experiments to discussions. Scientific learning attained under his supervision is a humble and life changing experience.

The atmosphere in JNCASR is immensely motivating, especially for excelling in scientific pursuit. I would like to thank Professor C.N.R. Rao for his kind words of encouragement. The commitment he shows to science is contagious, and his mere presence in the vicinity is inspiring.

I would thank my collaborators Dr. Pabitra Nayak, Dr. Zhiping Wang, Dr. Jacob Wang and Professor Henry J. Snaith from the University of Oxford for providing the perovskite solar cells and all the discussions leading to the conclusion of this work. I would further like to offer my gratitude to the CPMU chairman Professor Chandrabhas Narayan and instructors of all my credited and audited course work Prof. N.S. Vidhyadhirja (special thanks for the discussions related to research problem), Prof. Rajesh Ganapathy, Prof. G.U. Kulkarni, Prof. K.S. Narayan, Prof. Shivaprasad, Prof. Umesh Waghamare, Dr. Soma Biswas (IISc) and Prof. L. Umanad (IISc). Classroom learning from all them was uplifting.

I would like to thank all my past and present lab mates Dr. Satyaprasad, Dr. Murthy, Dr. Ravichandran, Dr. Prashant, Dr. Rahul, Dr. Suman, Vikas, Rishav, Shreyas, Pratik, Manasa, Nisha, Azhar, Swathi, Raaghesh, Anaranaya, Ganesh, Deepak, Sumukh, Sukanya, Abdul and Krishna for their amiable support, fruitful discussions and providing a very healthy lab environment. I thank Manjunath MN and Mr. Rajkumar for their timely assistance.

I thank the hostel wardens, Prof. T. K. Maji, Prof. Ranjini Viswanatha, hostel office, Dhanvantri staff, mess staff, and all other working staff at JNC and students' residence for making life pleasant and easier. I am thankful to JNC for providing me the financial assistance during my stay. I thank Sr. administrative officer Mr. Jayachandra and other administrative staffs for their services. I thank the Academic, Library, Accounts and complab for their assistance. I also appreciate the efforts of garden staffs for maintaining this beautiful campus.

I thank all my friends from the Volleyball group, dramatics society, music society and cultural committee especially Manoj, Divya, Pradeep and Prem Kumar. I would like to thank Samarth, my ex-roommate, and friend with whom I started my research journey in JNC. It was a great experience while working in a team as a students' representative; I thank Atif, Sambhavi, Siddharth, Aishwarya, Brijesh, and Chhavi. The friendship developed during this phase will be a souvenir from JNC.

I extend my gratitude to my teacher from IET, MJP RU Professor A.K.Gupta for his guidance. I also thank my old friends from school and undergrads Chandrakant, Ankit, Aman, Shubham Mishra, Dharamveer, Akanksha, Rishab Dev, Hemant, Anand, Arpit, Shubham, Amit, Adarsh, Monika, Shashank, Deepak, Abhishek, Navneet, Anurag, Mayank, and Shivesh. These are the people I have grown up with, and they have shaped my thinking. I finally offer my respect and gratitude to my parents and sisters Ritu and Rekhu and all my relatives for their patience, love, support, and encouragement.

May, 2017

Apoorva Singh JNCASR, Bengaluru

Synopsis

In the field of thin film photovoltaics, the organic-inorganic hybrid methylammonium lead halide perovskites have received a significant amount of attention owing to their superior charge generation and transport properties. They typically exhibit a high absorption coefficient, large carrier diffusion lengths, mobilities and lifetimes which are comparable to that of inorganic semiconductors. Power conversion efficiencies of perovskite solar cells have now reached above 22% and show great potential for applications in tandem solar cells. Further, they are easy to fabricate, low cost, and roll-to-roll processable. Despite its remarkable photovoltaic properties, the stability of perovskite layer is a major challenge, which is an impediment to the commercialization of these devices. Multiple extrinsic and intrinsic factors such as oxygen, moisture, light exposure, temperature variation and electric field have been reported to accelerate degradation of perovskite layer. The scientific literature lacks the clear understanding of the multitude of defect evolvement processes and their role in carrier transport mechanisms in perovskite-based devices. Thus requiring a reliable tool, which could probe the stability of the device against different degradation causing processes (preferably at an early stage) and could also provide valuable insight into the transport dynamics.

In this thesis, the utility of noise spectroscopy, as a quantitative tool, to gauge and understand the extent of degradation in these devices is emphasized. The noise in any system is a direct manifestation of the events happening at the microscopic levels. Deviations from a constant magnitude (time independent), steady state response upon continuous photoexcitation are reflected in the photocurrent fluctuations. A multidimensional stochastic variable can be formed mainly due to the charge carrier trapped at different energy states.

The **first** part of the thesis comprises details of the materials and methods employed and noise measurements strategies used in the study perovskite solar cells. The experimental set-up is meticulously designed with proper shielding (use of the faraday cage) and grounding. The typical device under measurement is always kept inside a customized vacuum chamber under positive nitrogen pressure to keep the ambient device conditions constant during the

experiment. JV characteristics and efficiencies under 1 Sun illumination were measured out using a solar simulator AM1.5. Trans-impedance amplifier (for amplification of current signal), the dynamic signal analyzer (DSA) and digital storage oscilloscope (DSO) are primarily used to record the time series signal. Further processing is done on a desktop PC. Accurate frequency response in the relevant ranges of the frequencies is obtained from statistical averaging and by giving sufficient record time.

In the **second** part of the thesis, different architectures of the perovskite solar cells, which include two conventional and one inverted structure have been studied. Devices are kept under short circuit condition in the dark. They are then photo-excited with exposing light of different intensities from low to high. Noise signals have been analyzed using the Hooge's empirical relation. Fluctuations in the number of charge carriers and fluctuations in the mobilities have been identified as the primary sources of noise. The salient features include: (i) Universal $1/f^{\alpha}$ behavior observed for frequencies (f) < 1 kHz (ii) The magnitude of the exponent α and the frequency range over which 1/f response is visible has a strong correlation with the transport processes and the associated disorder in the system (iii) for a given device, the noise signals shows characteristic dependence on the intensity of optical excitation. The intensity dependent noise feature also shows a significant dependence on the device architecture. In addition to the 1/f noise, the generation and recombination noise, which originates from the trapping and de-trapping events of the carriers, is also observed in the inverted device structure. Also, model ionic systems have been studied to qualitatively understand the noise feature related to the ionic transport. The observed noise spectra have no observable frequency dependence (white noise), the noise levels are significantly lower than that in the case of perovskite solar cells.

The **third** section of the thesis deals with the degradation studies in the perovskite solar cells. Noise magnitude for degraded cells is orders of magnitude higher than that for the efficient devices. The Noise magnitude, relative to the input current signal, directly correlates to the performance parameters, the noise magnitude increases with further degradation. A consistent *1/f* behavior over large frequency bandwidth (50 kHz) is observed in the degraded cells. The evolution of the noise features with degradation of the cell provides valuable information for predicting the trajectory of decay in efficiency or the useful lifespan.

In the **final** part of the thesis, large area photocurrent scanning has been performed in conjugation with the noise spectroscopy under localized excitation. Regions with large

differences in photo response were selected for local noise analysis from the large area photocurrent maps. Noise studies carried out in these regions correlates well with the macroscopic studies and suggests a significant dependence of the noise feature on photocarrier generation efficiency. Implementation of this method on large area cells, at different stages of performance, provides crucial information regarding the initiation and propagation of degradation. The observations suggest that the degradation process initiates from the periphery of the cell and progresses inwards.

In this thesis, an attempt is made to understand the noise features associated with the charge transport and degradation in hybrid perovskite solar cells. The noise fluctuations measured in the photocurrent signal correlates well with the performance parameters of the cell. A general trend of increase in noise amplitude and *1/f* behavior spanning over a wide frequency range, as a function of aging, is established. High-resolution spatial mapping of the photocurrent in typical devices and the associated variation of the noise spectrum confirms the outlined trend.

Publication

- *Insights into the microscopic and degradation processes in hybrid perovskite solar cells using noise spectroscopy*, **Apoorva Singh**, Pabitra K. Nayak, Suman Banerjee, Zhiping Wang, Jacob Tse-Wei Wang, Henry J. Snaith and K.S. Narayan.

  (Manuscript under review) (2017)

Contents

List of figures

Abbreviations

HOIP	Hybrid organic-inorganic perovskite
PCE	Power conversion efficiency
S-Q	Shockley-Queisser
OPVs	Organic photovoltaics
DSSCs	Dye-sensitized solar cells
MSSC	Meso-superstructures solar cells
FTO	Fluorine-doped tin oxide
ETL	Electron transferring layer
HTM	Hole transporting materials
FWHM	Full width half maxima
FF	Fill factor
DSA	Dynamic signal analyser
TIA	Trans-impedance amplifier
DUT	Device under test
g-r	generation-recombination
FFT	Fast Fourier transform
PSD	Power spectral (spectrum) density
NPSD	Normalized power spectral (spectrum density)

Notations

k_B	Boltzmann Constant (JK^{-1})
T	absolute temperature (K)
q	electronic charge (C)
f	frequency (Hz)
N	charge carrier density (cm^{-3})
μ	mobility ($cm^2V^{-1}s^{-1}$)
σ	Conductivity (Scm^{-1})
V_{oc}	Open circuit voltage
J_{sc}	Short circuit current
$S_I(f)$	Current power spectral density (A^2Hz^{-1})
$S(f)$	Normalized or relative power spectral density (Hz^{-1})

Chapter 1

Hybrid Perovskite Solar Cells and Noise Spectroscopy: An Introduction

By 2040, the world energy requirement is expected to increase by 48% with major need coming from the developing nations, China and India.[1-3] World population growth, increasing industry densities, vehicles and increase in per head consumption are the main reasons for this increasing energy requirement. Currently, per capita consumption of energy (a measure of development index) of USA and Canada is twice of Europe and more than 800 times of some of the developing countries.[4] We have been relying on the conventional sources such coal, petroleum and natural gas for quite some time now, as our primary energy source. However, it is not long before that they will be exhausted sometime, considering their limited quantity.

Electricity is the most important form of energy usage. According to two "IEA- key world energy statistics 2016", 40.8 % of the electricity is generated by coal, 21.6 % from natural gas, 16.4 % from hydro energy, 10.6 % from nuclear energy and 4.3 % from oil. Electricity generation from other sources like wind and solar is just 6.3 %. In general, today oil is used for major energy production. However, oil and natural gas are on the verge of depletion. At the current rate, by the mid of this century, they will be left with the meager amount. Moreover, this will further increase the demand for coal, and also fossil fuels are then expected to run out by the end of the century. An indispensable fact which also needs to be considered is the pollution and the Carbon emissions from these sources. It can be seen that there is an urgent need of reducing dependency on the fossil fuels and look for other energy resources. The importance of sustainable development is being realized, and efforts are made towards the proliferation of green renewable forms of energy. As stated by Al Gore (an environmentalist and Nobel peace prize winner 2007) *"As more and more people understand what's at stake,*

they become a part of the solution, and share both on the challenges and opportunities presented by the climate crises."

Solar energy is the cleanest form of the energy, and importantly it is in abundance and is underutilized. In fact, all the other forms of energy sources one or the other way depends on the Sun. The solar energy thus has the greatest potential to provide a viable solution for the energy crises without threatening the environment. Photovoltaic technology is dominated by Si-based p-n junction solar cells however they have a theoretical limit of the power conversion efficiency (η %) known as "Shockley-Queisser (S-Q) limit"[5]. Meanwhile, the quest for newer approaches such as organic photovoltaics (OPVs), dye-sensitized solar (DSSCs) cells, etc. are in progress. Amidst all these advancements in photovoltaics, very recently (last five years); the world has witnessed the emergence of a new type of PV technology in the form of hybrid organic-inorganic perovskite (HOIP) solar cells.[6]

1.1 Advancements in photovoltaics: Generations of solar cells

French physicist Edmond Becquerel, in the year 1839, first experimentally demonstrated the photovoltaic effect. Since then, many developments including the important discovery of photoelectric effect added to the understanding.[7,8] In April 1954, Daryl Chapin, Calvin Souther Fuller and Gerald Pearson practically demonstrated the working photovoltaic cell in public[9]. In subsequent decades, efforts were made to minimize the cost and improve the efficiency. The advancements in solar cell technology can be classified into three generations.

1.1.1 First generation solar cells

First generation solar cells are mainly based on Si wafer. They are the one dominating the commercialized solar panel industry because of consistent performance of 15-20 %, and much higher stability than non-silicon solar cells. They are very robust and durable. Several other solar cells made up of contemporary materials such as GaAs are found to be more efficient. However, silicon cells continue to be the more popular to be used in residential locations as a rooftop. Depending upon the type of the silicon used to make the module, first generation solar cells are further classified as *monocrystalline, polycrystalline and amorphous silicon cells.* Monocrystalline silicon solar cells are derived from large single crystals.[10] Controlled conditions are required to grow the single crystal effectively.[11] This makes the process to be

complex and energy intensive, even though the efficiencies are high. The product cost is amongst the highest in silicon-based solar cells.

Polycrystalline silicon is relatively much easier to grow than monocrystalline. This brings down the cost of production however the efficiencies do not remain as high as mono-crystalline.[12] Unlike mono-crystalline and polycrystalline, amorphous silicon solar cells need not be grown as a crystal rather they can be deposited a thin film on a substrate like glass, plastic or metals.[13,14] This makes them a suitable candidate to be used as flexible electronic devices.[15] Efficiencies are much lower than the crystalline one however they can be produced in bulk and cost of production is low. Also, progress is being made to combine the advantages of different types of solar cell technology. These are classified as hybrid silicon solar cells. For instance combination of highly efficient monocrystalline solar cells sandwiched between amorphous silicon results in better efficiency along with improved thermal stability.[16]

1.1.2 Second-generation solar cells

The second generation of solar cells forms the family of thin film solar cells. They are mainly derived from copper indium gallium telluride (CIGS) and cadmium telluride (CdTe). These solar cells consist of semiconductor layers of thickness ranging from hundreds of nanometers to a few microns, which is much lower than the crystalline Si cells which can be several hundred microns thick. In general, their performance is in the range of 10-15 %. Lower material consumption and non-involvement of silicon wafer reduce the cost up to some extent than the first-generation solar cells. However, high-temperature treatments and vacuum processes involved still keep the production cost comparable to Si-based cells. Involvement of scarce elements is another limiting factor for cost.[17-19]

1.1.3 Third generation solar cells

Most of the current research in the field of photovoltaics revolves around the third generation of solar cells. They use organic materials like small molecules or polymer along with new materials like nanomaterials, quantum dots, conductive plastics and organic DSSCs.[20-22] Perovskite-based solar cells come under this category. The third generation also involves experimental multi-junction tandem solar cells which hold the record for highest efficiency. OPVs are simple, inexpensive and production is easy. They are solution processed, and their fabrication is further simplified by the capability of the roll to roll printing which is a well-established industrial process. This process is inexpensive so that these flexible devices can be

produced at much lower costs than the previous generation cells and attempts are made to improve the light absorption capabilities, by designing the material to be able to absorb in infra-red to absorb additional. Some of the companies have started to emerge aiming at the commercialization of this third generation solar cells. However, their stability is one of the major factors which is an impediment to the commercialization.[23]

Figure 1.1: *Highest Power conversion efficiencies for the third generation of solar cells*.

1.2 Hybrid organic-inorganic perovskite solar cells

Crystalline material with the formula ABX_3 are classified as perovskite where A and B represent cations, and X is an anion. The ideal perovskite structure exists in simple cubic crystal form with corner sharing BX_6 octahedral network. Ions 'A' are present in the interstices, and there exists a bond angle of 180° in B-X-B.[24] It is possible for a given perovskite structure to adopt a structure with lower symmetry at lower temperatures. At these lower temperatures (~ 160 K), distortion of the BX_6 octahedra may result in tetragonal or orthorhombic phase.[25,26]

1.2.1 HOIPs

In hybrid organic-inorganic perovskites (HOIPs), 'A' is an organic cation which is monovalent. Recently lead halide HOIPs have emerged as highly efficient optoelectronic materials. According to Goldschmidt tolerance factor,[27] formations or non-formation of the perfect cubic crystal is governed by the size restrictions of the ions. First three-dimensional organic–inorganic hybrid perovskite was discovered by replacing cesium in $CsPbX_3$ (X = Cl, Br or me) with methyl ammonium cations (MA = $CH_3NH_3^+$) by Dieter Weber, in 1978.[28,29] Synthesis of HOIPs is carried out by various methods such combining a metal salt such as PbI_2 with an organic halide salt like MA iodide in one step and spin-coating of the solution of the both the salts. Co-evaporation and a two-step process of first forming the metal salt film followed by the exposure of organic halide are other common synthesizing techniques. The

most common material for fabricated high-efficiency HOIP solar cells is the $CH_3NH_3PbI_3$.[7,30-32]

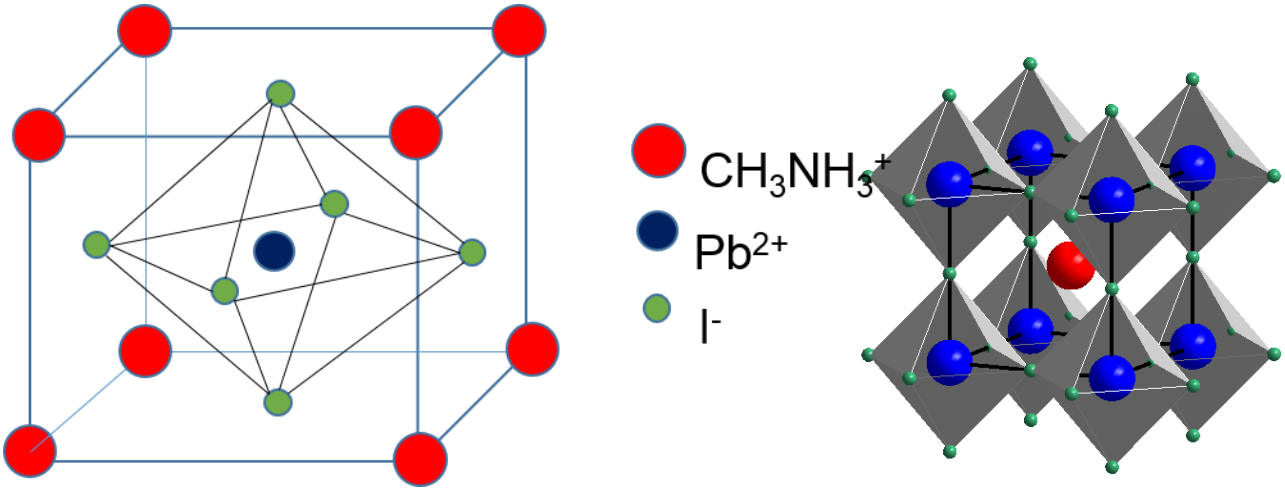

Figure 1.2: *Crystal structure of primitive unit cell of perovskite*

1.2.2 Evolution of perovskite solar cells

Perovskite solar cells are basically evolved from the dye-sensitized solar cells (DSSCs).[33,34] Three major components are involved in DSSCs composition. Mesoporous n-type TiO_2 is sensitized with a dye which is light absorbing, and this is filled in with electrolyte, redox active. To absorb most of the incident Sunlight, porous TiO_2 is needed to deliver sufficient internal surface area for adequate dye absorption. However, thick films of the order 10 µm are required for complete light absorption over the entire absorbing region of the dyes. This becomes impractical for solid-state DSSCs (ssDSSCs), where the thickness is limited to less than 2 µm due to some factors.[35] Alternatively, inorganic absorbers like quantum dots or extremely thin semiconductor absorber layers can enable complete light absorption in relatively much thinner films and potentially extend the photo activity into the near infrared region (NIR).[36,37]

The first perovskite sensitized solar cells were reported between 2006 to 2008 by Miyasaka and co-workers. $CH_3NH_3PbI_3$ and $CH_3NH_3PbBr_3$ were employed as absorbers along with an iodide tri-iodide redox couple. Polypyrrole carbon black composite solid-state hole conductor was also used in some cases. Measured power conversion efficiency (PCE) varying between 0.4 and 2 % for solid state electrolyte and liquid electrolyte cells respectively were reported. It was in 2009 when first peer-reviewed journal publication of a perovskite sensitized solar cell came, employing the iodide/triiodide redox couple and $CH_3NH_3PbI_3$ absorber resulted in 3.5 % efficient sensitized solar cell.[38] Further optimization of the titania surface and processing of perovskite by N.G. Park and co-workers reported an improved 6.5 % perovskite liquid electrolyte solar cell.[39] However, one of the drawbacks of this electrolyte –based perovskite

sensitized is that the perovskite absorber decomposes or dissolves in the electrolyte resulting in rapid degradation within a few minutes.[39] Need for the optimization of the perovskite absorber solution with a solid state hole conductor was felt. Providentially, methyl ammonium tri-halogen plumbates (salts containing lead) do not crystallize in nonpolar organic solvents.

Attempts were made to come up with new approaches, and improved efficiencies (8-10 %) were achieved with solid state perovskite cells employing Spiro-OMeTAD.[40,41] Perovskite absorbers have much greater power absorbing capability over a broad range than the dye. This enables complete light absorption in films as thin as 500 nm. This is significant as previously light absorption, and photocurrent generation was constrained by the thickness limitation of 2 μm in solid state cells.[35]

1.2.2.1 Meso-superstructures solar cells (MSSC)

A breakthrough, crucial for shaping the future research interest in perovskite came in 2012, from Snaith and co-workers.[40] During the process of investigating the charge –transport properties of the perovskite solar cells, they noticed a significantly faster charge extraction rates for the perovskite sensitized solar cells than the conventional DSSCs. There could be two possibilities for this faster extraction either there are surface states that influenced by perovskite affecting trap site density in the TiO_2, or substantial fraction of long-range electron transport is occurring through the perovskite. The latter, fast transport through the perovskite was counter-intuitive as perovskite absorber coated upon the internal surface of the mesoporous TiO_2 was least expected to be continuous to sustain long-range electron transport. Also, in previous reports perovskite absorber has been shown to exist in the form of isolated quantum dots, and many still classify these perovskite-sensitized solar cells as quantum- dot sensitized solar cells.[37]

However, cells were constructed by replacing mesoporous TiO_2 with insulating Al_2O_3 with a very similar meso-morphology with an aim to study and figure out whether or not electron transport occurs through the perovskite phase. Surprisingly, not only the charge transport was found to be faster, and photocurrent unaffected with the TiO_2 replacement, but for one to one comparison, open circuit voltage (V_{oc}) increased by 200 to 300 mV which resulted in 10.9 % efficiency solar cell.[42] Difference between the optical band gap of the absorber and the V_{oc} can be quantified as the fundamental loss in energy[43]. Interestingly, this was found to be extremely low, which meant the potential for greater efficiency improvement in future.

An entirely new approach to photovoltaics was started with this discovery as quoted by *Henry Snaith: "Concerning the nature of the technology, there no longer remain any of the original components of the DSSC; therefore, we can consider this an "evolutionary branching point", where a new technology has emerged that we have termed a meso-superstructure solar cell (MSSC), due to the presence of the mesoporous scaffold acting as a superstructure, upon which the photoactive layer is coated."*[42]

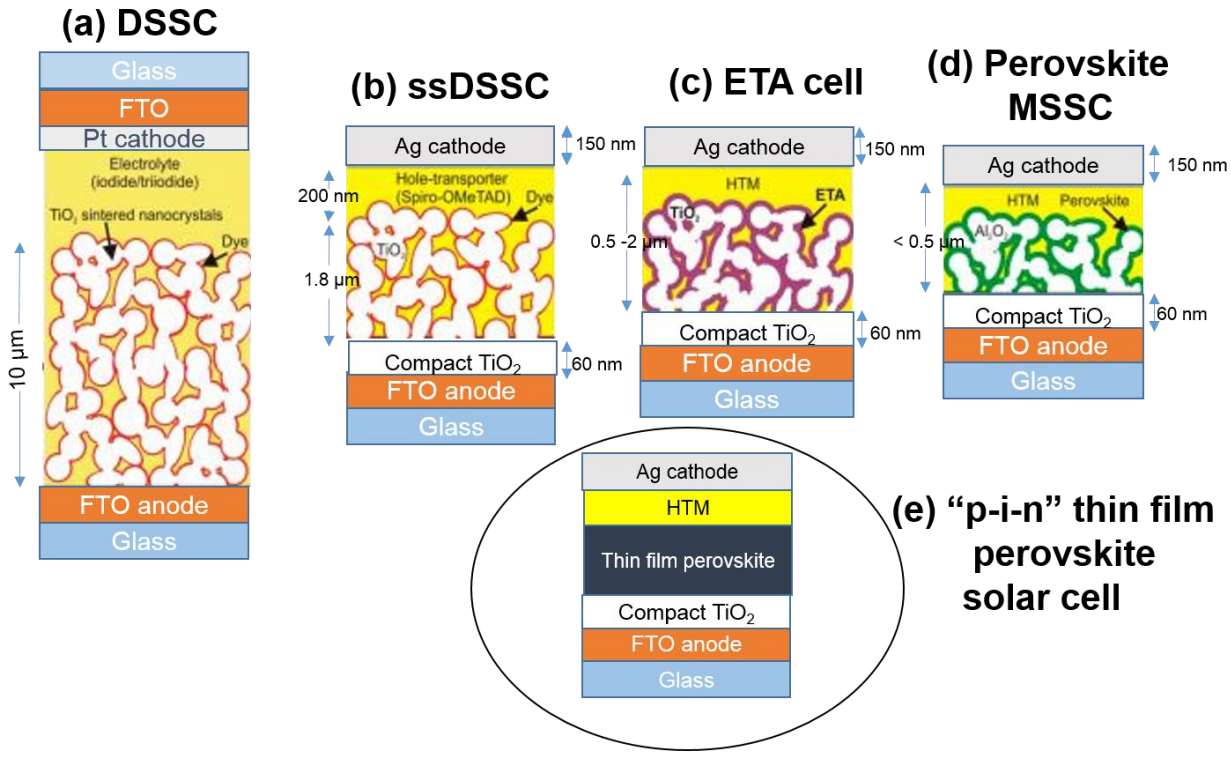

Figure 1.3: *Historic evolution in the development of perovskite solar cells: (a) electrolyte-based mesoscopic DSSCs*[33] *(b) the electrolyte is replaced with an organic p-type hole conductor in the ssDSSC*[44,45] *(c) dye is replaced by extremely thin layer absorbers (ETA) forming ETA cells*[46,47] *(d) ETA is replaced with a perovskite absorber and a porous insulating scaffold is used to replace n-type TiO_2, resulting in perovskite MSSC*[40] *(e) development towards thin film perovskite solar cells, where there is no requirement of porosity, and the device takes on the structure of an intrinsic and or ambipolar perovskite sandwiched between charge extracting contacts.*[42]

1.2.2.2 Standard device architectures

With multiple research groups working in the field of perovskite solar cells, various combinations of device structures have been tried out.[48-51] They can be broadly classified into three categories:

(i) Planar structure (regular TiO_2 based)

(ii) Inverted structure

(iii) Mesoporous based

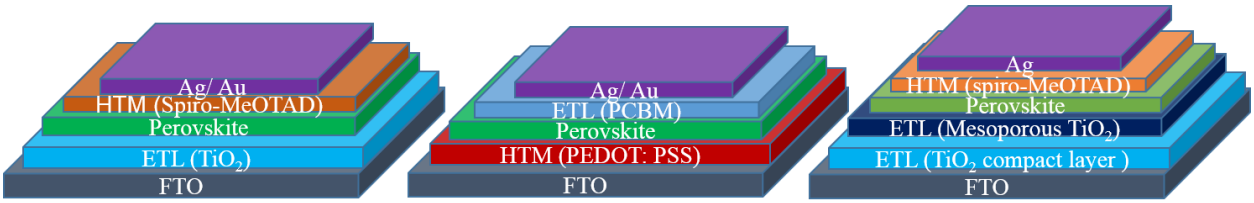

(a) Regular TiO_2 based (b) Inverted (c) Mesoporous based

Figure 1.4: *Standard device architectures for the fabrication of perovskite solar cells*

The planar structure, also known as regular architecture is the most common mesoscopic HOIP device architecture. Its configuration is FTO / TiO_2 / perovskite / spiro-MeOTAD / Au. To start with a good electron transferring layer (ETL) is deposited on Fluorine-doped tin oxide (FTO) or any other substrate such as indium tin oxide (ITO), this is followed by the deposition of perovskite layer over which a hole transporting material is laid and at last, Au or Ag is coated as counter electrode.[52]

Inverted device structure made up of PEDOT: PSS was first proposed by Chen and co-workers.[53] PEDOT: PSS is coated directly on the transparent conducting substrate over which perovskite is deposited followed by C_{60} based derivatives such as PCBM coated as ETL. The motivation for this structure is the ambipolar properties, specifically the superior p-type performance perovskite which is significantly influenced by the p-n junction heterojunction concept in organic solar cells. Other HTM like poly-TPD are also tried out instead of PEDOT: PSS in inverted architecture.[54]

Mesoporous TiO_2 based devices have the most stable architecture. Here in addition to the compact TiO_2 an additional mesoporous TiO_2 layer is introduced.[55-57]

1.3 Properties of HOIP: Reasons for unprecedented interest

Lead halide HOIP has recently gained popularity as highly efficient optoelectronic material and is being researched and developed for photovoltaics, light emitting diodes, field effect transistors, photodetection and laser devices. With just over five years of research, solar cells with hybrid perovskite-based absorbing material prepared by simple low-temperature solution processing techniques which initially shows 4 % efficiency are now capable of delivering efficiencies above 20 % is quite extraordinary.[38,58] Just to help appreciate this rapid development, best single inorganic cell (GaAs) took about 60 years of research to reach record efficiency of 29 % starting from 4 % in 1956.[59,60]

1.3.1 Free carrier generation and exciton binding energy

$MAPbI_3$ is calculated to have fundamental band gap of ~ 1.7 eV, and experimentally it is found to have an optical bandgap of ~ 1.6 eV.[61] This difference in optical and fundamental band gap is given by the exciton binding energy (E_B) which is close to the optimal value of ~1.1- 1.5 eV for a single p-n junction solar illumination under standard AM 1.5G condition within the Shockley-Queisser model.[62] Like any other perovskites, HOIPs undergo a phase transition at lower temperatures, they first adopt a tetragonal and then an orthorhombic structure upon further temperature reduction. At room temperature, it exists in cubic phase. All the three phases are *direct band-gap semiconductors* with a fundamental band gap similar to cubic phase.[63,64]

1.3.2 High absorption coefficient

Optical bandgap in a material is used to quantify the absorption onset in materials and is defined as the lowest photon energy needed to create a neutral electron-hole pair. The electrostatic attraction between the photo-generated electrons and holes contributes to the E_B which renders the optical gap smaller than the fundamental bandgap. E_B determines the fraction of free charge carrier present under typical optoelectronic device conditions, and for efficient charge carrier separation in solar cells, the value of E_B should be small.

In solar cells involving direct bandgap semiconductors, the charge carriers are efficient as light absorption can proceed without the phonons assistance. In PV devices, the carrier generation profile depends on the absorption coefficient; the absorber layer can be significantly thinner

than the observed diffusion length. The absorption coefficient of ~ 10^5 cm^{-1} in HOIPs is among the materials capable of yielding solar cells with $\eta > 10$ %. Nearly 100 % of the absorbed light is captured within a 300 nm thick layer. There is an exponential part of the absorption coefficient curve and near the optical band edge, known as Urbach tail. The materials like low crystallinity, the disordered and amorphous materials show this exponential tail as they have localized states extended in the band gap. The sharp and clear absorption onset is expressed in the small Urbach tail and energy. This value for HOIPs is 15 meV which is comparable to 11 meV in Si and eight meV in GaAs, which results in a low density of sub-bandgap states near the band edge.[65]

1.3.3 Mobilities, effective masses, lifetimes and diffusion lengths

HOIPs have a low effective mass of the order of ~ 0.10- 0.15 m_o, resembling values for Si and GaAs.[66] Measured diffusion lengths and mobilities depend upon inversely on the effective mass are proven to be modest in comparison with the high-quality semiconductor materials such as GaAs and Si. Mobilities of 1-30 cm^2 V^{-1} s^{-1} and diffusion coefficients of 0.05-0.2 cm^2 s^{-1} are found for polycrystalline films. In single crystals mobilities exceeding 100 V^{-1} s^{-1} are observed. However, it is limited by the scattering processes in HOIP materials.[67-70]

Long carrier lifetimes ranging from 100 ns to >1 μs (under one sun illumination) appear to be responsible for efficient carrier collection. The values are comparable to low doped; surface passivated GaAs. This explains why despite modest mobilities, the long carrier lifetimes result in long diffusion lengths, several times longer than the absorption depth resulting in efficient carrier collection.[70-72]

1.3.4 Ease of production, low cost, and flexibility

In addition to the high optoelectronic performances, perovskite solar cells possess inherent properties of other third generation solar cells such OPVs. They can be fabricated on a flexible substrate and are easy to process via solution processing at low temperatures. The cost of bulk production is expected to be really low on considering the less energy involved in the production and abundance of the material in the earth.

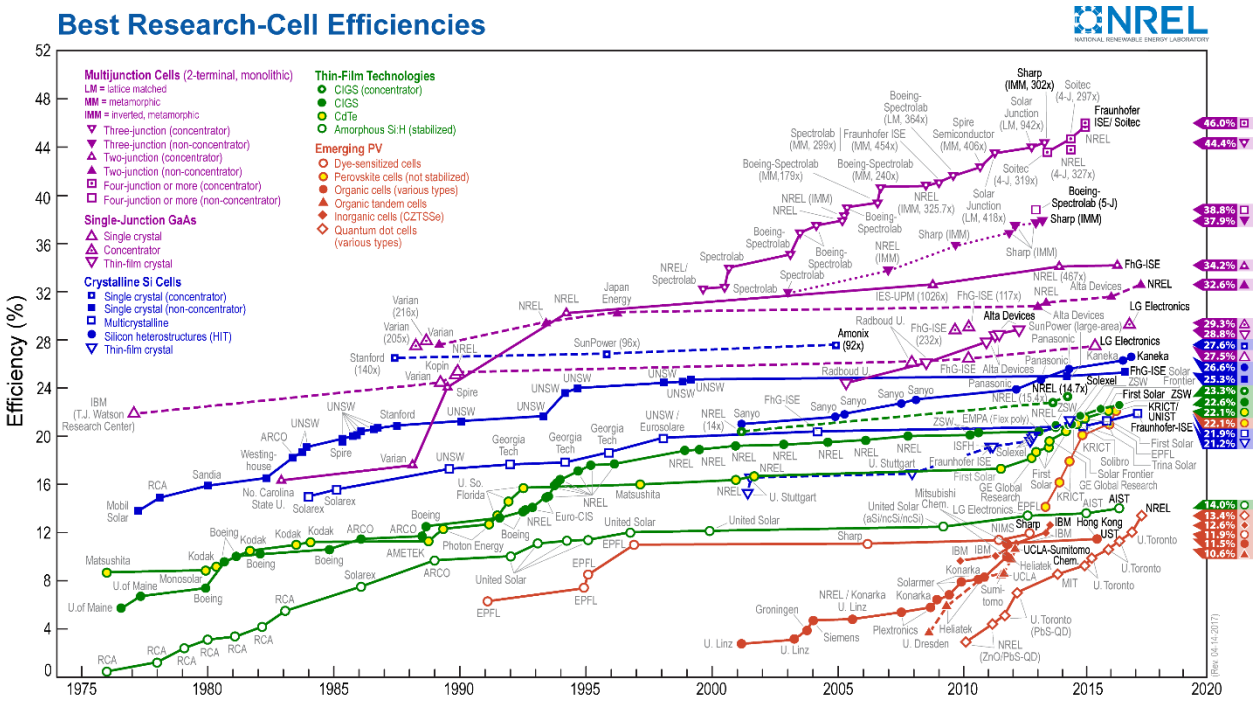

Figure 1.5: *Chart depicting record efficiencies of different types of solar cells. (courtesy NREL)*

1.4 Carrier transport in optoelectronic semiconductors

Material's absorption coefficient determines the carrier generation profile under optical excitation. Free and excitonically bounded carriers are resulted due to carrier generation and are dependent on exciton binding energy (E_B), the temperature of the sample and carrier density. In the absence of an electric field free carriers diffuse with diffusion coefficients $D_{n,p}$, and in the presence of the non-zero field, additional drift with mobility $\mu_{n,p}$ will also contribute to carrier transport.

Einstein's relation: $\mu_{n,p} = e\, D_{n,p} / k_B T$ relates this diffusion and drift parameters. Here, e is the absolute electron charge; k_B is the Boltzmann constant and T is the temperature. Effective mass relates the band structure of the crystal to the mobility and diffusion coefficients. Defects and lattice vibrations result in scattering that limits the carrier transport. Before carriers recombine, they have an average recombination lifetime τ during which they diffuse or drift. Recombination rates determine the lifetime depending upon the type of radiation processes (Radiative or non-radiative). These processes depend on the carrier density, trap density, dopant concentration and other factors.

The average distance traveled by carriers before recombination is given by the carrier diffusion length and can be expressed as $L_{n,p} = ([k_B T/e]\ \mu_{n,p}\, \tau)^{1/2} = (D_{n,p}\, \tau)^{1/2}$. Diffusion length reduces

several important parameters of material quality to a single value; thus L is a very useful parameter analyzing transport in semiconductors.[59]

'Carrier generation' by the absorption of light and the 'charge separation' are the necessary processes for the efficient solar energy conversion. Electrons undergo excitation in the absorber perovskite. The role of ETL is to separate out electrons by providing a conductive path to electrons while blocking holes. Similarly, HTM allows transport of the hole with no impedance and rejects electrons. This results in separate Fermi levels of the electrons and holes to equilibrate with the Fermi levels in the metal contacts., generate an external voltage, and to extract the carriers, yielding a photocurrent in the external circuit.

1.5 Degradation, instability and unusual properties

Although efficiencies of hybrid perovskite solar cells have rapidly reached high values, however, these HOIP suffers from the serious drawback of fast degradation. In earlier versions of the devices (2011), an unencapsulated device PCE would get reduced by 80 % in just within 10 minutes[39] because of the perovskite quantum dots tend to dissolve gradually into the redox electrolyte. Decomposition of perovskite to PbI_2 in the presence of moisture is another major challenge. Extreme caution is required while device handling because of the presence of toxic Pb also. With efforts, stability is getting improved for instance a mesoporous TiO_2 based device without encapsulation had shown stabilities of over 2000 h in air and dark and in a recent work a perovskite with 19.5 % efficiency with a stability of 500 h under prolonged illumination has been demonstrated.[73] Although, improvements in stability and degradation rates are vigorously pursued to ensure the commercial feasibility of these hybrid perovskite solar cells, this work is still way far from complete. For a technology to be feasible in real world application, consistent performance for a decent time scale is imperative. In HOIP solar cells, there are still various issues related to degradation, the interface and the stability of the device which are required to be addressed to achieve good reproducibility and durability with high PCE and performance.

In addition to the degradation, there are many puzzling transport properties which require deeper understanding. Some of the unusual charge transport properties observed in HOIPs which are different from other direct band semiconductors such as GaAs are described here.

Hysteresis

Hysteresis in perovskite solar cells, first reported by Hoke *et al.*.[74] is readily observed in photocurrent –voltage curves. Hysteresis is the dependence of the curve in the direction (forward or reverse scan) and/or speed of the bias scan. It is hypothesized that the interface between the perovskite and charge transporting layers (one or both) can be related to hysteresis. Amidst various arguments, ion migration currently is the most accepted reason for the observed hysteresis. Though it's not very clear that which ions migrate, the evidence of ion migration is strong. Ion blocking nature of the contacts at the interface results in a build-up of the ionic charge which shields the applied and built-in fields. Redistribution of ions within the device takes place because of the ion migration; this produces an electric field which either aid or counter-act the charge carrier extraction. The performance of the cell will be hampered by the low charge extraction. Band offsets at the relevant interfaces are also likely to get affected, as charge accumulation on one side of the interface will result in shifting of the energy levels or bands of the component containing the charge. Another viewpoint regarding the origin of hysteresis is that it is due to the ferroelectric effect which is well known to exist in oxide perovskites and some metal-organic frameworks materials. However, the exact reason for the origin of hysteresis is still open for discussion.

Another unusual effect observed in the case of HOIP solar cells is the observance of giant switchable photovoltaic effect. [75,76] Application of small electric field of <1 V μm^{-1} can repeatedly switch the direction of photocurrent. This effect of switchable photocurrent is generally seen in the devices based on ferroelectric materials. The HOIP devices can reach switchable photocurrent as high as 20.1 mA/cm^2 under one sun illumination, which is four orders of magnitude larger than that measured in other ferroelectric photovoltaic devices. In addition to this, there are several effects observed in perovskite solar like, some of the light-induced effects which can be easily explained by the regular semiconductor theories. So it can be seen that there are still many aspects of HOIP solar cells which require a clearer understanding of the intrinsic processes. The detailed energy band diagram of perovskite solar cell is shown in figure 1.6.

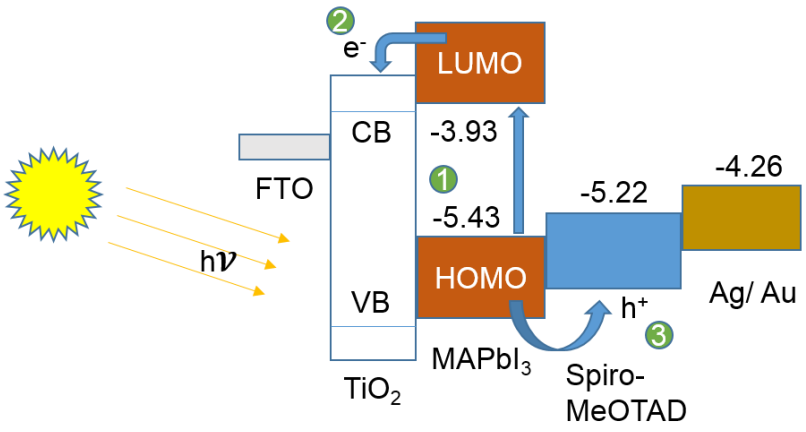

Figure 1.6: *Energy band diagram for perovskite solar cell*

1.6 Sources of degradation

The degradation of perovskite solar cells has been attributed to multiple external factors including exposure to moisture, oxygen and *UV* light [77] along with temperature variations[78]. Ion migration, electromigration, and interfacial reactions are some of the internal intrinsic factors which appear to play a critical role in the degradation[52,79,80]. Irreversible reactions occurring at the interface of hole transfer layer and the perovskite layer have also been cited as a factor for the deterioration of the devices[81]. Metal migration from the electrode into the hole transporting layer (HTL) has also been suggested as a mechanism for lowering the performance parameters[82].

The formation of HOIP material depends on the chemical composition of the precursors and the controlling parameters of the reactions, such as the pressure and the temperature of the system. It has been shown that low-temperature conversion to the HOIP dominates given by equation (1.1) -(1.3) on the other hand, there is a formation of additional PbI_2 at a higher annealing temperature (equation (1.2)).[83]

$$PbCl_2 + 3CH_3NH_3I \rightarrow CH_3NH_3PbI_3 + 2CH_3NH_3Cl \quad (1.1)$$

$$PbCl_2 + 3CH_3NH_3I \rightarrow PbI_2 + CH_3NH_3I + 2CH_3NH_3Cl \quad (1.2)$$

$$CH_3NH_3PbI_3 \rightarrow PbI_2 + CH_3NH_2 + HI \quad (1.3)$$

Up to 300 ^oC, it has been confirmed that there is no decomposition of the $CH_3NH_3PbI_3$ crystal lattice.[26,84] However, above this temperature organic ingredients, start to decay, and the mechanism is governed by equation (3). In contrast, studies show that $CH_3NH_3PbI_3$ starts to

transform to PbI_2 at lower temperatures till 140 ^oC.[83] As observed from the XRD measurements, excess organic CH_3NH_3Cl formed in the process is found to sublime leaving behind $CH_3NH_3PbI_3$ on the mesoporous TiO_2 film. These measurements suggest that the formation HOIP films is a multistage process consisting of vaporization of solvent, perovskite crystallization and excess sublimation of organic CH_3NH_3Cl (equation (4)). Composition and morphology of the film are determined by the rates of these simultaneously occurring processes.

$$PbCl_2 + 3CH_3NH_3I \rightarrow CH_3NH_3PbI_3 + 2CH_3NH_3Cl\ (g) \quad (1.4)$$

However, solution mixture is observed to be of light yellow color though the initial CH_3NH_3I and PbI_2 is white indicating the possibility of formation of a new phase due to a chemical reaction.[85] So, equation (4) is expected to have several intermediate steps.

$$PbCl_2 + 3CH_3NH_3I \rightarrow PbI_2 + CH_3NH_3I + CH_3NH_3Cl \quad (1.5)$$

$$PbI_2 + 3CH_3NH_3I + 2CH_3NH_3Cl \rightarrow CH_3NH_3PbI_3 + 2CH_3NH_3Cl\ (g) \quad (1.6)$$

$$PbI_2 + xCH_3NH_3I + yCH_3NH_3Cl \rightarrow (CH_3NH_3)_{x+y}PbI_{2+x}Cl_y(\text{intermediate phase}) \rightarrow$$

$$CH_3NH_3PbI_3 + 2CH_3NH_3Cl\ (g) \quad (1.7)$$

Equation (5) suggests the formation of mixed phases of PbI_2 (light yellow color in appearance), CH_3NH_3I, CH_3NH_3Cl and some unreacted $PbCl_2$ in the spun film. Equation (6) and (7) are the possible outcome of the reactions during the annealing.[86] CH_3NH_3I reacts with PbI_2 to give dark brown $CH_3NH_3PbI_3$ and the excess CH_3NH_3Cl breaks away from the film (exact reason of this escape is still unclear). There is a possibility of appearance of an intermediated phase as indicated by equation (7) during the early stage of annealing or during spin coating.[85]

1.6.1 Oxygen-induced degradation

In the presence of organic molecules, UV illumination can activate the diffusion of molecular oxygen.[87-89] This facilitates the formation of peroxide or superoxide compound that attacks and degrades the active layers.[90] Interstitial defects and oxygen vacancies result in a non-stoichiometric composition (TiO_{2-x}). One oxygen vacancy and two under-coordinated Ti(III) is created by the elimination of bridging oxygen atoms. Thermal annealing frequently leads to elimination of bridging oxygen atoms from the lattice.[91]

Formation of Ti(III) ($3d^1$) trap state in HOIP solar cells is because of the transfer of one electron to the Ti(IV) ($3d^0$) of TiO_2 from the perovskite. Smaller bandgap between Ti(III) and Ti(IV) helps in smooth electron transfers into Ti(IV) from Ti(III). The under-coordinated Ti(III) created from the oxygen vacancies reside in the sub-band gap states and act as deep trap sites. Moreover, they attract molecular oxygen in the ambient conditions, leading to the formation of $\alpha(Ti(IV)^{+}O_2^{-})$. Similarly, electrons in sub-band gap states may form $\beta(Ti(IV)^{+}O_2^{-})$.[91-93] Oxygen-induced defects in TiO_2 are one of the major cause of device degradation.[94,95]

1.6.2 Light-induced degradation

The performance of HOIP solar cells can get seriously affected by the illumination due to the generation of many possible fading processes upon exposure during prolonged operation. Localized trapping sites are generated by electron recombination and affect the depletion layer and band excitation of TiO_2.[96-98] This may result in the oxidation of halogen atoms in the perovskite or the HTM during UV illumination. In addition to UV, oxidation, heat and visible light can also contribute to the degradation. However, UV illumination is considered to be the major contributor to the degradation.[99,100]

1.6.3 Moisture induced degradation

Moisture is one of the main causes responsible for degradation in unencapsulated perovskite solar cell devices. While optimized level of moisture can be beneficial for the formation of good quality (high optical performance) film growth, however, at higher humidity levels HOIP films may decompose to PbI_2.[101] Degradation due to moisture may be correlated to the transformation of $MAPbI_3$ to its MAI salt and metal halides, thus, removal of metal halide can also cause degradation of HOIP based devices. In a report by Wang and co-workers[102], it is shown that during the process of assembling and testing, atmospheric moisture can directly degrade these materials.

1.6.4 Temperature-induced degradation

The temperature dependent decomposition of methylammonium iodide may result in the formation of HI and CH_3NH_2. NH_2 CH_3 can remain within the perovskite network and then perturb the photovoltaic processes.[103] Lead halides as a degradation byproduct severely deteriorate the device performance because of their light absorption ability, poor optical

behavior, and high bandgap. Furthermore, the expansion and compression mechanisms in the dimensional changes of the perovskite structure at low and high temperatures are not still clear. High temperature can also cause the diffusion of interlayers, metal counter electrode diffusion, degradation of ohmic contacts and device architecture degradation,[99,104] hence, the mechanisms of these phenomena should be reported with great care.

1.6.5 Thermal and electric field induced intrinsic degradation

One of the important sources of degradation in HOIP solar cells is the degradation originated from the interface. This can be correlated to the intrinsic deprivation in the devices. The probable origin of this degradation is (i) Flow of components (temperature induced) due to thermal evaporation during deposition and illumination of light during operation. This migration of the components of the materials induced thermally, at the interface results in inter-diffusion phase segregation and separation leading to an inherent strain. (ii) Migrations induced from the electric fields which result in electro-migration and hysteresis effect. Ion migration is especially sensitive to the concentration of mobile vacancies depending on the process.[105]

Effect of electron extraction by TiO_2 from an iodide anion can act as a driving mechanism for decomposition which gets accelerated by the light illumination during operation. The possible decomposition mechanism on the TiO_2 surface can be given by the following equations[106]

$$2I^- \leftrightarrow I_2 + 2e^- \quad (1.8)$$

$$3CH_3NH_3^+ \leftrightarrow 3CH_3NH_2\,(g) + 3H^+ \quad (1.9)$$

$$I^- + I_2 + 3H^+ + 2e^- \leftrightarrow 3HI\,(g) \quad (1.10)$$

1.7 Need for a reliable monitoring tool

From the above discussions, it can be seen that in a very short period, perovskite solar cells have gained a lot of attention from the scientific community. Many hypotheses have been put forward regarding the explanation of the mechanisms in these cells still many controversies, and lack of clarity revolve around this field. Efficiencies of HOIP solar cells have increased rapidly, but a thorough understanding of the transport properties of these materials and their underlying physical mechanisms are only starting to emerge. There is more to be known regarding the carrier transport mechanism and important things to know about the degradation procedures. Moreover, mechanisms like ion migration which are considered to be the main cause of the observed hysteresis in these devices also need to be further explored.

This need for further exploration specially regarding the degradation and stability of the device can be understood by the following statements from a review by Berhe *et al.*[52] *"Despite the understanding of the formation of Omh-perovskite materials for solar cell use, the full advantage of these materials and their devices is still not realized due to the presence of unsolved problems. One typical example is a lack of clear understanding of the mechanism of the active material and device degradations which controls essential processes like the device lifetime and the mechanical stability of Omh-PSC panels. For the successful development of Omh-PSCs, it is essential to understand the degradation behavior of Omh-perovskites and devices in general. The study of Omh-perovskite degradation behavior is a pre-requisite for Omh-PSC applications."* (Omh: organometal halide)

Noise measurements can be a very effective tool in gauging the degradation profile and understanding the carrier transport mechanisms.

1.8 Noise measurement as a nondestructive technique to study solar cells and other semiconductor devices

Electrical noise, in general, is a well-understood phenomenon. In most abstract fields of thermodynamics, statistical mechanics and also in the fields of models that show what the electrons are doing in specific cases, the noise theories are well developed. These theories and models are supported by many experimental works on electronic devices.

Noise spectroscopy is nondestructive, an in-situ technique which has been used for reliability studies in semiconductor devices [107-111]. It has been used to study systems like quantum wires[112], graphene[113], FETs[114], along with different solar cells including silicon[115], organic[116,117], DSSC and hybrid perovskite[118,119]. Moreover, electrochemical systems involving ionic interactions[120] are studied as well.

1.8.1 Conductivity fluctuations

The instantaneous value of conductivity, in any semiconductor device, fluctuates around a mean value (σ). These observed fluctuations in the time series of current or voltage signal is called *"noise"*.[121] In the field of condensed matter the fluctuations are related to measured conductivity of systems like bulk materials, thin films, 2D materials, graphene, nanowires etc.[122] Noise is observed in multiple systems like physical, chemical, biological and physiological. It is also readily observed in astronomy, music and climate and various other systems. These fluctuations in the voltage or the current are random in phase and amplitude. A

random process can be represented in the form of a random function (*V(t)*), where t is the time and is the independent variable. *V(t)* is the sampled voltage signal as a function of time. It is possible to contribution from different sources/ charge carrier transport and are described as a *stochastic process* mathematically.

A random signal may have fluctuations around a mean *rms* value, but over a long sampling durations, random signals are mostly non-stationary. Random processes are in general, depicted as their spectral characteristics/ *spectral densit*y or correlated function and its *amplitude* characteristics, for instance, is the probability density function.

Representation in time domain

According to the central limit theorem, the distribution of the sum of a large number of independent, identically-distributed variables will approximately form a Gaussian (normal) distribution, irrespective of the underlying distribution. The mean (x_i) and the standard deviation (σ_i) or the full width half maxima (FWHM) are the two important parameters for the defining a Gaussian distribution.

Representation in frequency domain

In frequency domain analysis, a signal noise is represented regarding root mean square (*rms*) value of the amplitude of the observed quantity such voltage, current or resistance. Fast Fourier transform (FFT) of the sampled data is performed to obtain the frequency response of the time series data (signal). The magnitude of the FFT gives amplitude spectral density ($V/\sqrt{Hz}$ or $A/\sqrt{Hz}$). The square of the magnitude gives the power spectral density (PSD) ($V^2/\sqrt{Hz}$ or $A^2/\sqrt{Hz}$). The sampled voltage signal can be normalized by the trans-impedance gain in order to obtain current power spectral density, $S_I(f)$. Figure 1.7 shows the typical representative plots of data in time series, power spectral density and normalized histogram.

1.8.2 Noise and power spectral density: mathematical relationship

Spectrum and correlation function

Noise from a quantity X can be written as[109]

$$X(t) = < X > + \Delta X(t) \tag{1.11}$$

Stationary noise can be defined as $< \{\Delta X(t)\}^2 >$ and symbol < > implies averaging over a sufficiently long interval of time. $\Delta X(t)$ can be represented in Fourier series as follows:

$$\Delta X(t) = \sum a_i e^{j2\pi f_i t} + a_i{}^* e^{-j2\pi f_i t} \quad (1.12)$$

Here, a_i are fluctuating amplitudes. Component of noise measured at a frequency f_i is given by:

$$< \Delta X_i > = 0 \quad (1.13)$$

$$< (\Delta X_i)^2 > = 2 < a_i a_i{}^* > \quad (1.14)$$

Fourier component for a given bandwidth (Δf) adds up quadratically. *The measured noise in the unit bandwidth is called the spectral density.*There exists a close relation of power spectral density (PSD) $S_X\ (f)$ to the auto correlation function $\varphi X(t)$. Auto-correlation function defines, how on an average a deviation $\Delta X(t_o)$ will decay. $\varphi X(t)$ is defined as:

$$\varphi\ X(t) = < \Delta X(t_o) \Delta X(t_o + t) > \quad (1.15)$$

The relationship between $\varphi X(t)$ and $S_X\ (f)$ is given by Wiener Khintchine relations:

$$S_X\ (f) = 4 \int_0^\infty \varphi X(t) cos\ 2\pi f t\ dt \quad (1.16)$$

$$X(t) = 4 \int_0^\infty S_X\ (f) cos\ 2\pi f t\ dt \quad (1.17)$$

Basic noise model can be formed using these relations. The correlation function is obtained by the differential equation describing the transitions in the proposed physical model. Fourier transform should be by the observed noise spectrum, both in the magnitude and the shape. The exponential correlation function is the is the simplest. However, one of the most often encountered cases corresponds to the Lorentzian spectrum. If, on an average decay in the deviation ΔX is given by:

$$-d\Delta X/dt = \Delta X/\tau \quad (1.18)$$

The correlation function can then be defined as:

$$\varphi X(t) = < \Delta X(t_o) \Delta X(t_o + t) > = \langle \{\Delta X(t_o)\}^2 \rangle e^{-t/\tau} = \langle (\Delta X)^2 \rangle e^{-t/\tau} \quad (1.19)$$

Then Wiener –Khintchine theorem gives

$$S_X(f) = \langle (\Delta X)^2 \rangle \frac{4\tau}{1 + (2\pi f \tau)^2} \quad (1.20)$$

This is called the Lorentzian spectrum.

Since,

$$\int \frac{1}{1+x^2}\, dx = tan^{-1}x, \tag{1.21}$$

It can be easily obtained that

$$\int_0^\infty S_X(f)df = \langle(\Delta X)^2\rangle \tag{1.22}$$

Usually, $\langle(\Delta X)^2\rangle$ is used for a simple consideration, for example in case of number flucutations $\langle(\Delta N)^2\rangle = N$. The energy of $\langle(\Delta X)^2\rangle$ will be $\frac{1}{2}k_BT$, when the flucutation corrosponds to a energy in a degree of freedom. For low frequency ($f\tau \ll 1$), the spectrum is white and for $f\tau \gg 1$) the spectrum is of the form $1/f^2$.

1.8.3 Noise model for solar cells

In p-n junction, solar cells fluctuations depend on the factor like photo-generation processes and bias voltage. Current fluctuations can be produced from the trapping and recombination mechanism of the charge carrier because of the presence of defect states. Occupation probability of the traps (f_{trap}) can be related to the amplitude of the current fluctuations, *Var [I]*. This variance also gets influenced by the recombination pathways from the conduction band to the valence band resulting in the drop in minority charge carriers stored in the base material. Contributions from the traps can be modeled by two levels of energy, which act as trapping (E_T) and recombination (E_{SRH}) centers. These centers are situated above the intrinsic Fermi level (E_i) and are mainly responsible for the transitions between the defect states and the conduction E_v and valence E_v bands.[115] E_T energetic states with density N_T under photo-generated or injected charge carriers are capable of capturing and emitting electrons from the conduction band. Meanwhile, the E_{SRH} states, with density N_{SRH}, function as Shockley-Read-Hall (SRH) type centers with τ_{SRH} as an associated lifetime.[123]

In forwarding bias condition and at lower frequencies, the SRH recombination processes can be represented by an equivalent circuit. This consists of two parallel connection of a differential resistance R_D and a capacitance C_μ, which represent minority charge carrier contribution in the base material.[124]An RC circuit in series with C_μ along with series (R_s) and shunt (R_{sh}) resistances can be used to model the fluctuating traps with energy level E_T.[125] For a typical solar cell $R_{sh} >> R_D$, so its effect on current transport is negligible. Hence, the recombination mechanism associated with the trap states can be well described by the time constant $\tau_{eff} = R_D C_\mu$. A capacitance contribution C_{trap} may originate because of the density of empty traps into the base material. C_{trap} is related to the variation of f_{trap} in accordance with quasi-Fermi

level under non-equilibrium condition (charge carrier injection). However, the resistance R_{trap} depicts the kinetic factor of the traps and are governed by a characteristic trapping and de-trapping $\tau_{trap} = R_{trap}C_{trap}$.

The capacitance contribution of the fluctuating trap states become significant in the frequency region below $(2\pi\tau_{trap})^{-1}$ and it is possible to follow the charge carrier transfer from the conduction band to empty traps and vice versa from the noise spectroscopy. Fluctuations in the number of charge carrier is considered to be the major source of noise and contributes to a current

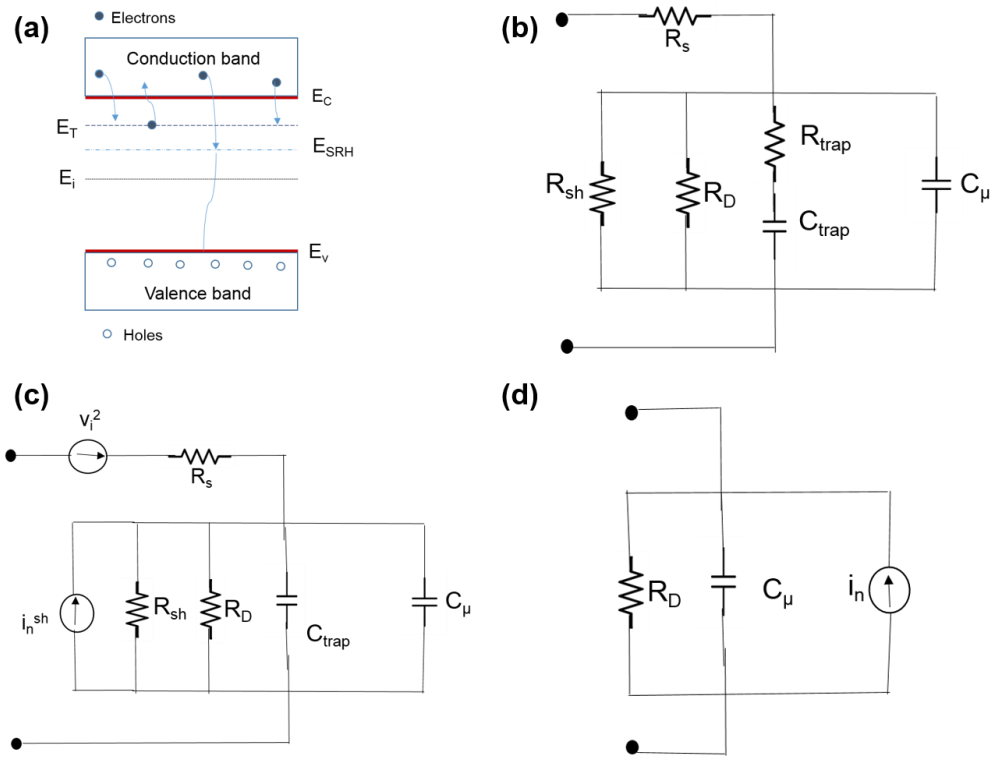

Figure 1.7: *Noise equivalent circuit of the solar cell.* ***(a)*** *Energy band diagram representing the carrier recombination and trapping processes of the silicon materials.* ***(b)*** *Solar cell's an equivalent electrical circuit.* ***(c)*** *An equivalent circuit including noise sources.* ***(d)*** *Simplified equivalent circuit.*

fluctuations that can be measured by the external contacts. A current noise source in the model can evaluate the effect of these traps and can represent the charge carriers transfer between C_{trap} and C_μ (figure 1.7 (d)). Thermal noise contributions v_t^2 and i_n^{sh} from R_s and R_{sh}, respectively and other types of noise (discussed in the next section) such as sh ot noise present in the p-n junction are significantly small for solar cells. Hence, a simple ac equivalent model can be presented, consisting of parallel connection of C_μ, R_D and i_n. Change in number of carriers originated due to dc bias or light absorption result in the generation of noise. A characteristic

1/f frequency spectrum can be observed with a cut-off frequency $f_x = (2\pi\tau_{trap})^{-1}$. Further analytical details regarding the variance due to current fluctuations can be found in the 'Appendix A'.

1.9 Types of noise

Noise is actually an unwanted signal, which for the successful operation of any electronic device should be as low as possible. However irrespective of the attempts to keep the noise level low, a minimum amount of noise is always present in every system. Its low value will result in a high signal to noise ratio (SNR) and lead to a high-performing semiconductor device. On the other hand, a high noise value can put the fundamental limit in the performance and practical application of the device. The fact that the noise can be measured in the semiconductor systems and significant inference can be drawn after the processing and the analysis of noise signal is utilized in studying various systems including solar cells. Depending upon the nature of the spectrum, noise can be categorized in different kinds. Some of the commonly occurring noise types and which can be used as a diagnostic tool are described here.

1.9.1 Thermal noise

Thermal noise also known as Johnson noise, Nyquist or the white noise is fundamental to all device and is caused by the random motion of current carriers.[109,121] Due to the Brownian motion of carriers, there is some spontaneous fluctuations in voltage across a resistor and have a white spectrum given by:

$$S_V = 4\pi kTR \tag{1.23}$$

where *k* is the Boltzmann constant, *T* is the absolute temperature, and *R* is the resistance of the ohmic sample. Thermal noise is often used to calibrate the noise to the setup of the noise measurement. This type of noise is used as a diagnostic tool in cases like (i) measurement of the temperature in hostile environment (ii) measurement of the internal resistance in the base of a bipolar transistor (iii) measurement of the quality of the heat contact between a film resistance and its substrate.

The white noise from a biased film is proportional to *T R* where the film temperature *T* is greater than the substrate temperature T_s. The ratio between the excess temperature ($\Delta T = T - T_s$) and the dissipated power in the film gives the heat resistance. High values of the thermal resistance are an indication of delamination of the layer and an indication of early failure. So

ΔT based degraded mechanisms are indicated by the strong increase in the thermal noise under bias condition. The spectrum of the thermal noise is independent of frequency (this is the reason why it is also called white noise).

1.9.2 Shot noise

Shot noise is always present in diode type of devices. This noise is due to the corpuscular nature of electricity and the random emission of charge carriers across a potential barrier.[126] The spectrum is white and proportional to the elementary charge q of the carriers and the average current I

$$S_I = 2qI \tag{1.24}$$

Deviations from the proportionality between S_I and I at very low current levels at very low current levels, are used to detect parasitic shunt resistors across photodiodes. Onset of multiplication in high fields is easily detected where the increase in S_I is more linear to current. Therefore, shot noise is a well-accepted diagnostic tool for quality evaluation in zener diodes and phot and avalanche diodes. At lower frequencies, shot noise can be obscured by the other types of noise (*1/f*, burst or generation recombination noise). The shot noise is observed at low temperatures when the thermal noise does not dominate.

1.9.3 Burst noise or RTS noise

Burst/ popcorn or random telegraph signal (RTS) noise is an indicator of a single trap activity in a system with only few charge carriers. They are common in small area devices, which are submitted to high fields and current densities. These devices degrade faster and show poor noise behavior. Burst noise is a non-Gaussian type of noise and originates due to fluctuation in the conductance. The spectrum of the burst noise is Lorentzian in nature. They are seen as discrete switching events in the time domain. The waveform is similar to a square pulse of randomly varying duty cycle and pulse width in a random telegraph message.

1.9.4 Generation-Recombination noise

Generation-Recombination (g-r) noise in semiconductors originates from the trapping and trapping in the number of charge carriers which gives rise to their fluctuation in current transport. Traps states in semiconductors are generally electronic states in the forbidden band

gap arising due to various defects and impurities in bulk and at the surface or the interface. The PSD of g-r fluctuation is given by[113,127]

$$S_N(f) = 4(\Delta N)^2 \frac{\tau}{1+(2\pi f\tau)^2} \quad (1.25)$$

where τ is the time constant for the transitions. The spectrum of the g-r noise is Lorentzian. Generation recombination noise is a well understood phenomenon, though it is not always possible to avoid traps, however it is possible for a device to be free from g-r noise in a certain temperature range due to the fact that the energy level is far above or below the fermi level. This results in negligible contribution from such trap states. In high-quality silicon devices g-r noise is often absent but not yet in systems like hetrostructures and compound semiconductors where lattice defects also impose challenge. In principal g-r noise can be reduced by using cleaner preparation techniques, so as to avoid trapping centers.

1.9.5 *1/f* noise

1/f noise or the flicker noise has been extensively last few decades as a tool for the quality or reliability check of a device. As the name suggests, its magnitude is inversely proportional to the frequency that is it has a *1/f* dependence. The *1/f* noise in semiconductor was modelled by Hooge for the equilibrium resistance fluctuations in homogeneous samples and was later applied to other systems for its simplicity. Basic assumption made by Hooge is that the noise arises from the bulk of solid and that results from the lattice scattering of charge carriers. The spectral power, as observed in resistance fluctuation can be depicted as:[107,108,112]

$$\frac{S_R(f)}{R^2} = \frac{\gamma_H}{Nf} \quad (1.26)$$

where γ_H is the Hooge's parameter, N is the number of carriers, I is the current. For the homogeneous ohmic systems, the relation between the current and voltage is linear, Hooge's relation can also be given as:

$$\frac{S_R(f)}{R^2} = \frac{S_v(f)}{V^2} = \frac{S_R(f)}{I^2} = \frac{\gamma_H}{Nf} \quad (1.27)$$

. The electrical *1/f* in occurs in abundance in contacts, resistors, films and in all electronic devices. *1/f* noise is observed not only in electrical conductance but also in physiological, geological and musical systems. In the well-studied field of noise, with an agreement between theory and experiments almost in all cases, *1/f* comes as a slight exception. There is a debate

about whether or not *1/f* noise originates from the same physical phenomena. It is possible that several types of *1/f* noise may require different theories to explain the experimental observations. *1/f* noise may originate from the fluctuations in a number of carriers and or lattice scattering. Nevertheless, analysis of experimentally obtained *1/f* noise spectrum provides a very useful method to gain insight about the carrier transport in any given system along with monitoring the stability of the devices. This fact about *1/f* noise is exploited in this thesis.

1.9.6 $1/f^2$ noise

Unlike g-r and *1/f* noise, where the current serves to measure the already existing conductance noise, the $1/f^2$ noise is considered to originate due to a dc-current induced resistance drift or resistance fluctuations. There exist a threshold current density and a threshold temperature, where $1/f^2$ noise can be observed. Beyond the current density of $2* 10^6$ A cm^{-1} for Al-based line the current initiates electro-migration, resistance drift and fluctuations. The $1/f^2$ noise analysis provides a useful method for quick and accurate measuring of electro-migration activation energies. Voltage noise spectrum can be give as:

$$S_v(f) = \frac{I^\beta C}{f^\alpha T} e^{-E_a/kT} \tag{1.28}$$

Here $\beta \geq 3$ and $\gamma \geq 2$, C is parameter depending upon geometry and technique. E_a is the electro-migration activation energy measured from the noise spectroscopy.

1.10 Analytical model for noise

Current or conductivity fluctuations ($\Delta\sigma = \Delta(qn\mu)$) are related to the fluctuations in charge carrier density (ΔN model) or mobility fluctuations ($\Delta\mu$ model)[112,127]. Especially in the case of solar cells, *1/f* noise is attributed to the carrier number fluctuations due to the random trapping and de-trapping events. Scattering of charge carriers leads to bulk mobility fluctuations[121]. However, it is possible to have a trapping noise model with contribution from both number fluctuations and mobility fluctuations. The current noise spectra are usually analyzed by Hooge's empirical relation and is expressed as

$$S_I(f) = \gamma_H \frac{I^2}{Nf} \tag{1.29}$$

Where, γ_H is hooge's constant (material property), N is the total number of charge carriers and *f* is the frequency (Hz). This relation is ideal when exponent of *f* is close to unity, however for

many systems α in $1/f^{\alpha}$ is found to vary between 1 to3. Another, simplified way of representing Hooge's noise model is given by:

$$S_I(f) = A\frac{I^2}{f^{\alpha}} \tag{1.30}$$

Here 'An' is the noise magnitude coefficient. A more useful and modified form of the Hooge's expression is used for initial analyses,

$$S_I(f) \propto \frac{I^{\beta}}{N\, f^{\alpha}}. \tag{1.31}$$

The exponents of current (β) and frequency (α) deviated from the proposed value of 2 and 1 respectively for many systems. These exponents are obtained by experimental fitting to observe power spectrum density (PSD) plots. The β value is a measure of the mixing of the various noise source in the device and to distinguish between the volume versus surface (interface) origin of the noise source. For surface trapping β ~ 1 and for volume trapping β ~ 1.5-2. The α value is interpreted as the distribution of traps responsible for the carrier number fluctuations. A value close to unity (± 0.2) is indicative of the uniform distribution of trap energies.

Further analyses can be made in terms of relative or normalized power spectrum density (RPSD) by normalizing the power spectrum density by I^{β},

$$S(f) \propto \frac{S_I(f)}{I^{\beta}} \propto \frac{1}{N\, f^{\alpha}}\,. \tag{1.32}$$

Relative or normalized PSD shows an inverse dependence on the number of charge carriers N, implying that noise amplitude is more pronounced when charge carriers are less, and vice versa.

Generation-recombination is another type of noise which originates due to the number fluctuation. It's PSD can be expressed in the Lorentzian form:

$$S(f) = \frac{S_0}{[1 + (2\pi f\tau)^2]} \tag{1.33}$$

where S_0 is the frequency independent portion of $S_I(f)$ observed at $f < 1/2\pi\tau$, and τ is the time constant associated with a specific trapping state.

1.11 Thesis overview

This thesis demonstrates the utility of noise spectroscopy in studying the intrinsic microscopic phenomena, evaluation of defect states and importantly probing degradation in hybrid organic-inorganic methylammonium lead halide perovskite solar cells. The progress in the field of perovskite solar cells is rapid with advancement being made to improve the stability. However, considering the still prevailing multitude of ambiguities in the understanding the carrier transport mechanisms and the challenges to achieving the consistent device performance, the in-situ monitoring of these solar cells devices preferably at an early stage can prove to be really useful.

In the second chapter material and methods along with experimental procedures are introduced. This includes the details of the types of perovskite solar cell structures studied along with other systems such as ionic solutions and dye-sensitized solar cells. Detailed procedures and protocols involved prior, during and after the noise measurement experiments are discussed.

The third chapter starts with the noise measurement results from the different ionic solutions, where an attempt is made to obtain the signature of noise contributions, exclusively from ionic transport. In this sequence, the DSSCs are specifically studied as they comprise of an electrolyte in their device structure. Perovskite solar cells have been studied to probe the variation in the device noise with respect to the history of the bias application in these devices also the noise at low voltage application is measured. Till this point, the noise the noise studies are carried out in dark conditions with just the small applied voltage (< 50 mV) or the bias application for some time (30 s to 120 s) and then starting the measurement.

The outcomes from the different structures of the hybrid perovskite solar cells are presented in chapter four. This chapter forms the main part of the thesis. Multiple devices of two regular structures and one inverted structure are thoroughly studied under different illumination intensities. The results are analyzed to come up with the conclusive trend of the noise at different stages of the device performance including the completely degraded stage. A direct correlation between the noise and the device performance can be seen from these results. Complimentary studies using thermal admittance spectroscopy (TAS) are also carried out to quantitatively observe the change in defect density with degradation.

In the fifth and the final chapter photocurrent scanning by local illumination is performed in these devices. This reveals the areas within a device with relative photocurrent response.

Further, noise is measured locally in these small regions with different photocurrent response. The combination of photocurrent scanning and the local noise measurements can provide a very valuable tool to monitor the stability of large area solar cells. This measurement approach is unique and to best of our knowledge it is for the first time noise is measured locally from illuminating such a small region (< 100 microns). The results and the approach in the thesis suggest the viability of the noise measurement as a non-destructive tool to gauge the stability along with collecting significant insights about the intrinsic processes in perovskite-based solar cells.

Chapter 2

Material Methods and Experimentation

Experiments related to noise measurements are very sensitive, and in order to capture accurate results for the analysis, the measurements should be carefully optimized. In this chapter methods adopted during experimentation and instrumentation involved are discussed in details. The different types of hybrid perovskite solar cells used for the study are also discussed with their specifications and structures.

2.1 Materials and studied device structures

Fabrication

Devices used in these studies were fabricated in Clarendon Laboratory University of Oxford, (U.K.) by Dr. Pabitra Nayak, Dr. Jacob Wang from Prof. Henry Snaith's group and shipped in sealed conditions to Molecular Electronics Lab, JNCASR Bangalore, India for the noise studies. Standard low temperature, solution processed methods used for perovskite solar cells were adapted for the fabrication. This involves spin coating of CH_3NH_3I with PbI_2 either their mixed solution (single step coating) or one by one (two step coating). All deposition processes happen at low temperatures (below 150 ^oC).[31,32,128]

Electrons and holes transferring materials

Different combinations of electron transferring layer (ETL) and hole transferring materials (HTM) are used in the studied device. The ETLs used in the fabrication of different structures HOIP solar cells include (i) titanium dioxide, (TiO_2) (ii) combined layers of TiO_2 and Buckminsterfullerene (C_{60}) and (iii) combined layers of 2,9-Dimethyl-4,7-diphenyl-1,10-phenanthroline (Bathocuproine/ BCP) and phenyl-C61-butyric acid methyl ester (PCBM).

The HTM materials used are (i) 2,2′,7,7′-tetrakis-(N, N-di-p-methoxyphenyl amine)-9,9′-spirobibluorene (spiro-OMeTAD) and (ii) Poly(4-butylphenyl-diphenyl-amine), phenyl-C61-butyric acid methyl ester (Poly-TPD).

Electrodes

FTO is deposited on a glass substrate and is used as the anode in all the structures. Ag/ Au are used as a counter electrode in the devices.

Device Structures

Three different device structures are used in the study. They include two conventional and one inverted structure devices. Device configuration for different structures is listed below:

a) FTO /TiO_2 /Perovskite / Spiro-OMeTAD /Ag (Device type 1)
b) FTO / C_{60} /Perovskite / Spiro-OMeTAD /Ag (Device type 2)
c) FTO / polyTPD / Perovskite / PCBM / BCP / Ag (Device type 3).

Picture of samples with an array of devices is shown Figure 2.1. Figure 2.2 depicts the device structures with details of the layers involved. Device (a) and (b) are of the conventional structure and (c) is of the inverted structure.

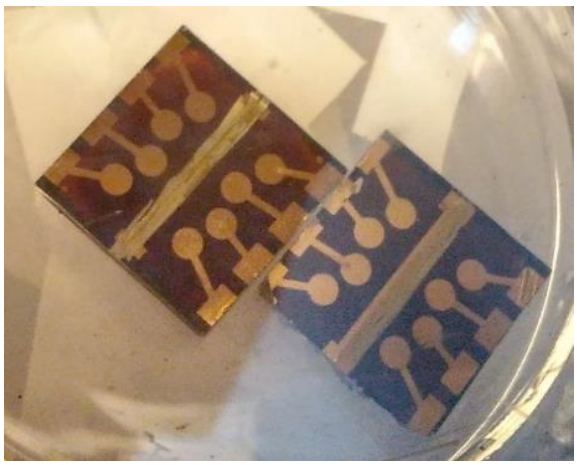

Figure 2.1: *Picture of the typical samples used for the studies*

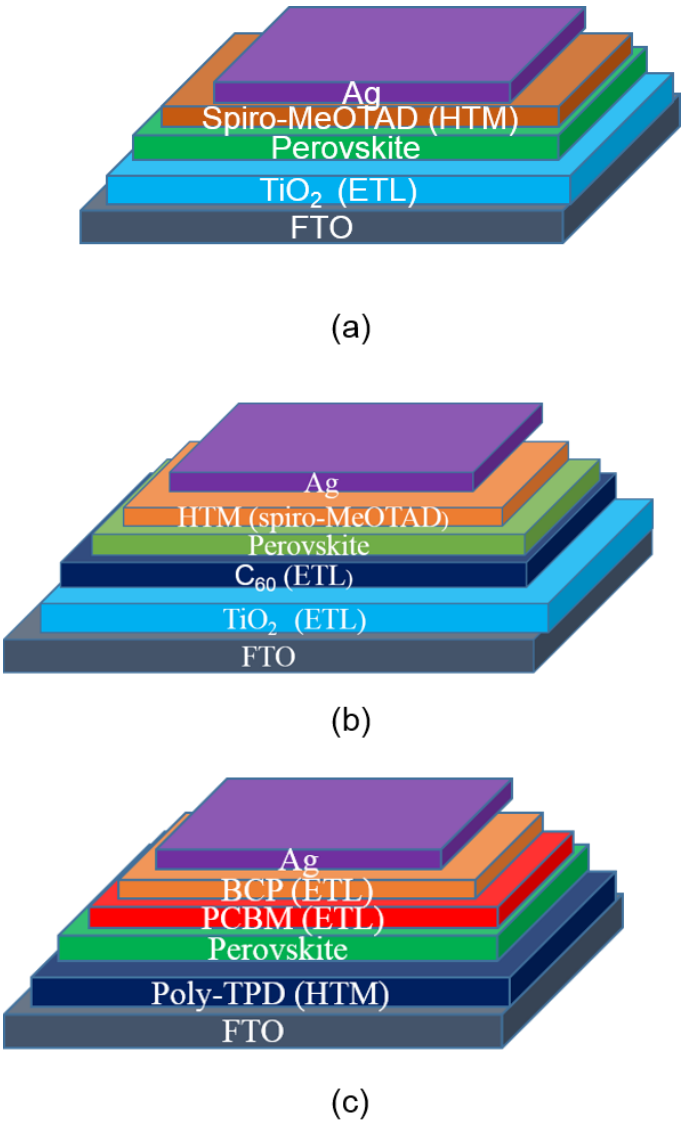

Figure 2.2: *Different structures of perovskite solar cells. (a) FTO /TiO_2 /Perovskite / Spiro-OMeTAD /Ag (b) FTO / C_{60} /Perovskite / Spiro-OMeTAD /Ag (c) FTO / polyTPD / Perovskite / PCBM / BCP / Ag*

Other *systems*

Solutions are made from salts such as KCl, $LiClO_4$, $AgNO_3$, NaCl, PSS (Polystyrene sulfonates), Nafion ($C_7HF_{13}O_5S.C_2F_4$) including PbI_2 and $CH_3NH_3PbI_3$. Noise is studied from these ionic solutions (chapter 3). A suitable concentration of each of these salt is used for the studies. In addition to this, dye-sensitized solar cells (DDSCs) are also used for the studies.

2.2 Instrumentation

The dynamic signal analyzer (DSA) and a low noise trans-impedance preamplifier (TIA) are the two major instruments which are used in the noise measurements. Prior to the noise measurements, solar cell devices are characterized using a solar simulator in order to obtain their respective power conversion efficiencies (PCE). The DC characterization and the settings and configuration that are essential for a reliable noise measurement are discussed in subsequent sections.

2.2.1 DC characterization

Standard PV measurements were carried out on the devices to ascertain the functioning of the cell in an inert atmosphere prior to the noise measurements. *J(V)* characteristics and efficiencies under 1 Sun illumination (100 mW/cm^2) are measured out using a Newport solar simulator (ORIEL SOL 3A TM) under AM (air mass) 1.5 conditions. Corresponding dark *J(V)* characteristics (lamp closed) are also measured. Devices are scanned in forward to reverse bias and vice versa in the range of (-200 mV to 1.2 V). The *J(V)* characteristics are used to measure the PCE of the solar cells. J_{sc} (short-circuit current density) and V_{oc} (open-circuit voltage) are the two important parameters for any solar cells and are obtained from the *J(V)* curves. Overall behavior of the solar cell can be defined by its fill factor (*FF*). This is the ratio of available power at the maximum power point (P_m) to the product of V_{oc} and J_{sc}:

$$FF\ (\%) = \frac{J_{max} \times V_{max}}{J_{sc} \times V_{oc}} \tag{2.1}$$

and the PCE of the solar cell can be calculated as:

$$efficiency\ (\eta) = \frac{J_{sc} \times V_{oc} \times FF}{P_{in}} \tag{2.2}$$

where P_{in} is 100 mW/cm^2.

For other cases, for instance in the characterization of ionic systems, J-V characterization is done by Keithley 4200-SCS parameter analyzer. Automated library functions are used for all the measurements. The values from these measurements have been used for noise analysis. The J(V) characteristics change with sweep rate and the applied bias time.

2.2.2 Transimpedance amplifier (TIA)

A current to voltage preamplifier is used to amplify the (current) signal from DUT. The TIA used in noise studies is SR 570 (Stanford Research Systems). Typical settings for noise measurement are summarized below.

Input current:

The amplifier is connected in series with the device (DUT), and there is a certain limitation to this input current that can be tolerated. Input current to the TIA refers to the mean DC value of current output from DUT that flows through it. The maximum input current to the TIA scales down with gain, from 10 mA at 10^3 gain to 10 nA at 10^9.

Gain:

This is defined as the ratio of the output voltage to the input current. Higher the gain higher will be the amplification of the small random signals riding over the mean current value. But this amplification comes with a compromise, the gain is inversely related to the bandwidth of the amplifier, and so the frequency ranges for analysis decreases with increasing gain. It is advisable to keep the gain at a value which is close to the inverse of the DUT resistance for optimum performance. Gain is referred to as sensitivity in SR 570, a sensitivity of 10^{-3}A/V means a trans impedance gain of 10^3V/A. The gain settings should be adjusted keeping in mind, first, the input DC current and then the frequency range that is required.

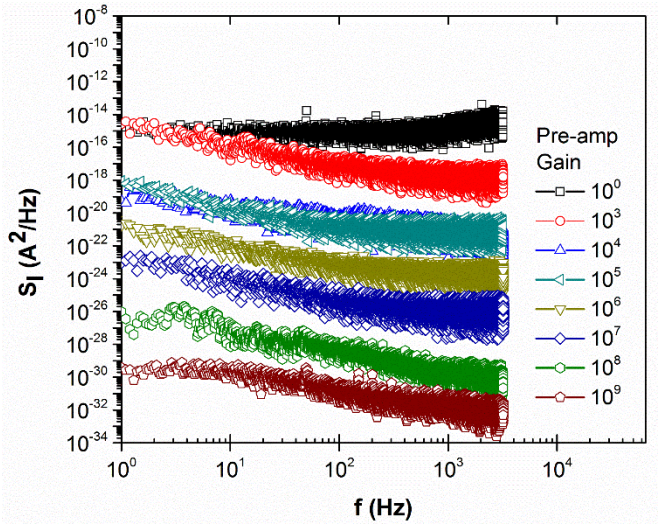

Figure 3: *Noise spectrum with respect to different gains.*

Figure 3 shows the change in noise spectrum with different gains. Lower noise signals can be measured by increasing the gain (amplification) of the TIA. Before the start of the experiment, depending upon the DUT, the gain should be suitably adjusted.

Bandwidth:

The upper 3-db cut-off frequency (or the bandwidth) is limited by gain settings. Like the maximum input current, the bandwidth also reduces with gain. Typically, it reduces from 1.0MHz at a sensitivity of 10^{-3}A/V to 10Hz at10^{-9}A/V in SR 570. The amplifier response is linear for a given bandwidth and rolls off at higher frequencies. This feature should be taken into account to avoid errors in data analysis.

Coupling:

The choice of coupling is optional and is required when the amplifier's DC bias is to be connected in series with DUT in the circuit. For most amplification purposes, the input coupling is "Ground." The voltage output can be AC or DC coupled; DC coupling is the normal mode of operation while in AC coupling a capacitor is placed in the circuit which removes the DC components (frequency close to zero Hz).

Precautions:

Proper care and attention should be given to the amplifier settings before making a measurement. Unmatched settings can lead to instrument failure and/or erroneous results. When the current exceeds the maximum allowable current, an" Overload" condition is reached which is seen as the glowing of a red LED indicator on the display panel. This condition should be avoided as much as possible, and in the occurrence of such an event, the connection from the DUT or the circuit should be terminated immediately to avoid severe instrument damage. The input coupling should be kept at "Ground" by default, and the DC bias kept at the lowest possible magnitude to avoid the accidental flow of large currents, through its input terminals, when low impedance DUTs are connected. Apart from these, other settings that are specific to the experiment like bandwidth, filter cut-off, input current noise, output coupling, etc. should be factored into data analysis.

2.2.3 Dynamic signal analyzer (DSA)

The Agilent 35670A dynamic signal analyzer (DSA) is a low noise 16-bit "FFT" spectrum analyzer that samples and stores voltage signal. Key points regarding the operation of DSA that is fundamental to making a reliable noise measurement, are explained below.

Input coupling:

The input to DSA should be properly configured before sampling. The choice of ground or float coupling is dictated by the physical grounding of the electronic circuit. The noise measurements, in this thesis, have DSA as the single grounding point in the circuit and so the input is ground coupled with the input channel. Apart from that, AC coupling is used to sample the fluctuations or noise in the voltage output from the amplifier. The channel input range (V_{pp}) for voltage signals is user-defined and should be defined by taking into account the largest peak-to-peak values of the input voltage (V_{in}) signals. The ability of DSA to resolve the smallest voltage signal is determined the number of bits (16) of ADC at the front-end and the selected input range. For the minimum possible V_{pp} range of 4 mV at DSA, the lowest value of Vin that can be faithfully detected is given by the relation,

$$V_{in} = \frac{V_{in}(4 \times 10^{-3})}{2^{16}} \approx 6 \times 10^{-8}\, V \qquad (2.3)$$

Thus, the voltage (energy) spectral density would be $\sim 10^{-15}$ V^2/Hz.

The power spectrum density is expected to be in similar range. However it is frequency dependent and decreases at higher frequencies. The channel input digitization noise is a practical bottleneck for measuring low noise signals, and so the signals are amplified before digital sampling to surpass the noise floor of the instrument. Also, it can be seen from above equation that the channel input noise scales up with channel range. The channel range should be such that smaller values don't lead to overload conditions and higher values don't overwhelm DUT noise.

Frequency span:

The bandwidth (BW) of DSA is DC to 102.4 kHz. This means that the higher frequency f_h limit is 102.4 kHz while the lower frequency (f_l) depends on the total sampling time duration (T). The upper frequency can be adjusted in power of 2 descending from 102.4 kHz while the lower frequency is adjusted by the number of resolution lines. The sampling frequency fs is adjusted

by DSA automatically corresponding to f_h while maintaining the Nyquist criterion. The mathematical relations for signal processing by DSA are given below.

$$f_l = 1/T \tag{2.4}$$

$$f_{span} = f_h - f_l \tag{2.5}$$

$$f_s = 2.56 \times f_h \tag{2.6}$$

Usually, f_h is dictated by BW at TIA, but higher frequencies can also be chosen to have higher sampling frequencies for better resolution in frequency response.

Resolution lines:

The ability to resolve two signals at closely spaced frequencies depends on the frequency resolution of the spectrum. The number of resolution lines, in DSA, is responsible for the frequency resolution (f_{res}) in the power spectrum plot. It can take values of 400, 800 and 1600 (used for noise measurements). In onetime capture frame, the lower frequency at DSA is defined by resolution lines.

$$f_l = \frac{f_h(3.2\ kHz)}{lines\ (1600)} = f_l(2\ Hz) \tag{2.7}$$

Also, minimum frequency resolution, $f_{res} = f_l$. Smaller the magnitude of f_{res}. higher is the resolution. The time span (Δt) of capturing one data frame is defined by f_l , as $\Delta t = 1/f_l$. Usually n (~ 50) frames are captured for averaging the plots and in that case, $T = n\Delta t$.

Data processing:

After getting configured for data analysis, the instrument is used in two modes. In the first mode, the time series capture of data (voltage v/s time) is stored in the buffer memory and subsequently transferred to a desktop for further analysis. A maximum number of data points that can be saved in one capture is determined by the buffer memory. In the second mode, the power spectrum is computed and averaged as per the user-defined settings and then stored on the desktop. For the time series data, all of the digital signal processing for computing the frequency response is done in Matlab (R2008b). The code used for this purpose is given in Appendix B.

Precautions: Like the TIA, the instrument channel should be protected from voltage signals that are greater than the channel input range. At low levels of signal input, the range can be in an auto-range mode to avoid such problems, but often it is required to have a constant thermal noise floor of the background setup. In that case, the channel range should be adjusted corresponding to the maximum current or voltage produced in the circuit. The input cables should be immediately disconnected in the event of an unexpected spike in voltage levels which requires a careful monitoring of the instruments during measurement. Same is true for the TIA.

The protocols are similar to the one followed during the noise measurements in organic transistors. *(Source: thesis, "Noise spectroscopy of Polymer Field Effect Transistors by Rishav Harsh"*).

2.3 Noise setup optimizations

External sources can significantly perturb the experimental noise setup. These disturbances primarily originate from electrical coupling with the signal path. This electrical noise can be induced, in wires, cables, and connections, due to electromagnetic interference or vibration effects. Therefore, controlling these unwanted signals and keeping it within acceptable limits is crucial to any data acquisition system. For designing a low noise measurement setup, at first, main noise source should be identified, and after that, the setup should be optimized in a way to minimize the noise resulting from outside of the device under test.

2.3.1 Noise sources

Electrical-noise sources are in abundance in most of the laboratories or the industrial settings. These noise sources may include AC power lines, heavy machinery (like motors, vacuum pumps), radio and TV stations, and a variety of electronic equipment. Radio stations generate high-frequency noise, while computers and other electronic equipment generate noise in all frequency ranges. Noise sources having a specific frequency appear as a sharp peak in power spectrum and can be identified, for example, peaks at 50/60 Hz and its harmonics are due to the power line, and peak at 2.4 GHz corresponds to Bluetooth and wi-fi operation. It is recommended to isolate and decouple the sources which generate noise over wide frequency ranges from the instrumentation setup. Noise may be coupled into electric circuits by various means, and a careful understanding of coupling methods can help eliminate them. Most commonly the noise couples into a circuit on a conductor. A wire running through a noisy

environment may pick up noise and then conduct it to another circuit. A major example of this conductively coupled noise is noise conducted into a circuit on the power supply leads.

Radiated electric and magnetic fields:

They are another potential source of noise coupling. In the presence of moving charge, all circuit elements including conductors, radiate electromagnetic waves. In addition to this unintentional radiation, there is the problem of intentional sources such radio broadcast station, radar transmitters and wireless communication waves in form wi-fi and Bluetooth signals.

The grounding conflict:

Preventing electrical shocks and electrical fires is the highest priority for ground circuits, but these redundancies (of ground connections) built into many electrical grounding systems create a conflict with data acquisition systems called as ground loops. A ground loop can be understood as multiple paths for ground currents. Several internal, common busses in a data control instrument are arranged to regulate current flows and terminate all paths at one common point. Usually, this one common point connects through low impedances to the safety ground connection on the instruments AC power cord. This connection prevents the internal system from floating at an AC potential between earth ground and the input AC supply potential. Measuring instruments that contain an earth ground as described above usually generate a ground loop. A ground loop can become a serious problem even when the ground voltage on the measured point equals the ground voltage entering the instrument through the line cord. A voltage that develops between the two grounds can be either an AC or a DC voltage of any value and frequency, and as the voltage and frequency increase, the ground loop becomes more troublesome and dominates the input waveforms in noise measurements.

Triboelectric effect:

A charge can be produced on the dielectric material within a cable if the dielectric doesn’t maintain contact with the cable conductors. This is called the triboelectric effect. It is usually caused by mechanical bending of the cable or if the cable is simply hanging without rigid support. The charge acts as a noise voltage within the cable.

Conductor motion:

If a wire is moved through a magnetic field, a voltage is induced between the ends of the wire. Due to power wiring and other circuits with high current, in the laboratories and industries, stray magnetic fields exist in most environment If a wire with a low-level signal is then allowed to move through this field, a noise voltage is induced in the wire. The problem can be especially troublesome in a vibrational environment.

2.3.2 Minimization of noise

Once the major noise source is identified, a set-up has been designed taking proper precautions which are ideal for noise measurements. The first and foremost thing for minimizing the environmental interference (electromagnetic interference) is to have a shielded metal enclosure or a faraday cage. The faraday cage in this setup has been made from 2mm thick aluminum sheet having a cubic shape of side length 20 inches. Shielding becomes vital when the circuit connections are open having unshielded metal wires and connections. In addition to this faraday cage, the HOIP solar cell DUT is kept inside a small vacuum chamber (filled with nitrogen), which is also metallic with glass opening for illumination. As can be seen in the next section, this vacuum chamber (itself a faraday cage) is kept inside the main faraday cage along with the low noise tungsten white light source, dc batteries (for powering the light source) and device connections. This is done to attain the maximum noise reduction from the external electromagnetic interference.

In order to give bias to the device or to supply power to the light source, DC power source should be preferred over AC power supply based voltage sources as it completely eliminates power lines interferences. The ground loop problem is avoided by having a single grounding contact at the signal analyzer (DSA). Connections from DUT and preamplifier are grounded with DSA channel input (with BNC coaxial cables) while the faraday cage is separately ground to instrument's ground connection port by a thick copper wire. The outer shield of BNC cables (from the DUT) is not shorted with the metal shield to avoid ground loops. Further, the instrument ground has been physically isolated from the rest of the instruments by having a separate ground line to the earth. Connections from the device to the BNC female connectors are fitted into the vacuum chamber, and the copper wires are soldered to the central pin for taking the contact from the DUT. The other free end of the copper wire is connected to the electrode of the device through silver paste (conducting). The silver paste used here is a dispersion of micron sized (0.5 microns or less) fine silver particles in amyl acetate. To avoid

noise induced in the circuit due to vibration, the entire setup has been kept on vibration-proof table. Eliminating sharp bends and cable motion further reduces noise (if any) due to triboelectric and conductor motion. It is advisable to have cable length as less as possible to avoid extra noise sources, coaxial cables of length one meter is used for all the connections.

2.4 Experimental setup for noise spectroscopy of HOIP solar cells

Low noise tungsten filament driven by low-noise dc power supply was used for the experiments. The photon noise level of this light source and the floor noise of the analyzer and the digital storage oscilloscope (DSO) were negligible in comparison to the device under test (DUT) noise under illumination. Control studies with low-noise commercial photodiodes were also carried out. The initialization procedure involved monitoring and recording the background noise which includes noise from all the experimental components and the device dark current (under short circuit conditions). This procedure ensures that the primary source of the fluctuations arises from the intrinsic device processes. The experimental set up for noise measurements is shown in figure 2.4.

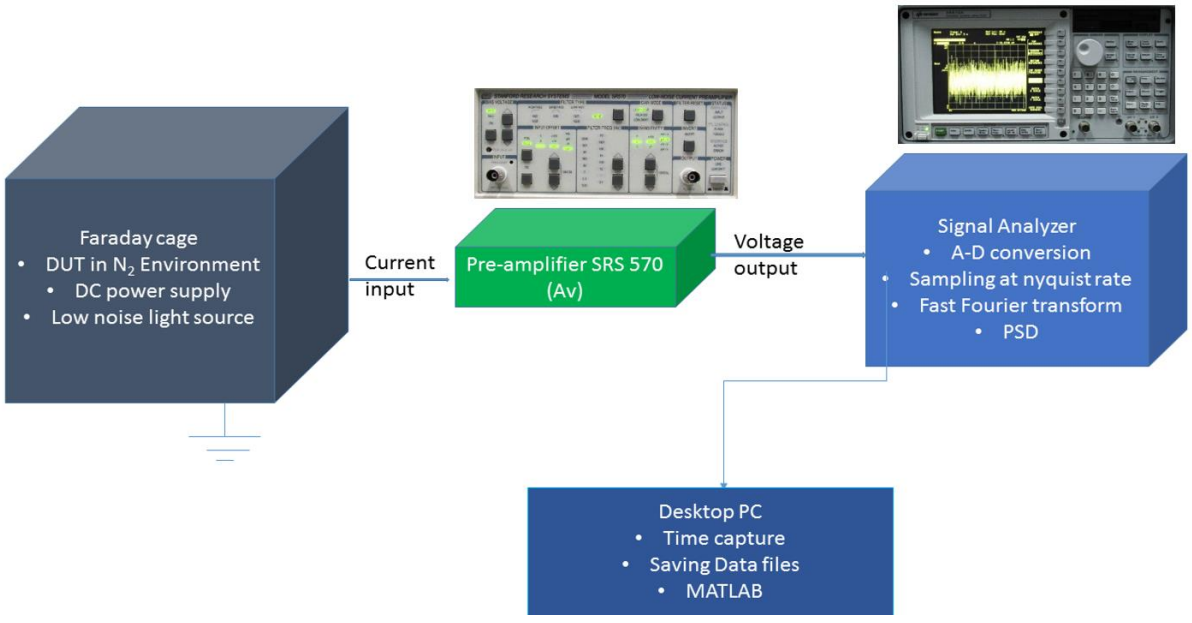

Figure 2.4: *Experimental setup for noise spectroscopy of hybrid perovskite solar cells*

Typical noise levels from these sources were in the order of ~ (<-80 $dBV_{rms}/\sqrt{Hz}$) or 10^{-14} V^2 /Hz) as compared to larger magnitude from the DUT. Trans-impedance pre-amplifier (SRS570)

and dynamic signal analyzer (DSA) (Keysight 35670A) were primarily used for data recording. The suitable gain was adjusted through the pre-amplifier and a resolution of 1600 lines from the analyzer is used to record in the time series for the 40s in a 500-millisecond window. Data is processed to get the frequency domain response for the bandwidth of 3.2 KHz. Fast Fourier transform (FFT) of time series data provided the power spectrum density (PSD) noise spectrum with respect to the frequency. Additional care was taken to obtain a clean noise spectrum using low-noise BNC cables free of interference from 50 Hz and other harmonic peaks from the surroundings. To achieve this accuracy, the experimental set-up was designed with proper shielding and grounding. The typical device under measurement was always kept inside a specially designed vacuum chamber under positive nitrogen pressure nitrogen in order to keep device ambient conditions, constant during the experiment. As discussed in the previous section, light source system and a chamber containing the device in nitrogen the environment was kept inside a faraday cage (electromagnetic shielding). Devices were kept under short circuit condition in dark. Devices were then photo-excited with exposing light of different intensities from low to high. DC value of photocurrent is typically linear with respect to intensity (Figure 3) and corresponds to estimated value from J_{sc} under AM 1.5 conditions. While light exposure of different intensities, corresponding J_{sc} values were recorded using Keithley 2400 source meter.

Photocurrent scanning and local noise measurement:

Devices are then examined using a photocurrent (PCS) arrangement, where an area of (4X4) mm was mapped by local illumination using a 630 nm laser, with intensity 1 mW/cm^2 and spot size of ~ 10 µm. The information obtained by PCS is then used to measure noise locally from regions less than 100 µm. For this purpose, the objective and the laser source, which is used for the PCS is arranged inside the noise measurement setup described above. By keeping track of the coordinates of regions of high and low PC response, the laser is focused at a particular spot to measure noise locally. (Details of local noise are given in chapter 5).

Chapter 3

Noise measurements in ionic systems

Noise measurements have been performed in literature in pure ionic solutions like KCl[129] and $CuSO_4$.[130,131] The nature of noise is mostly white, however, in some special cases, such as the presence of some impurities in the sample, *1/f* noise can be observed. Unlike the pure ionic solutions, systems with electrode-electrolyte interfaces, blend of solid-liquid electrolyte or systems with involvement both the ionic and electronic currents nature of noise could take interesting forms. In such mixed systems, at lower frequencies, noise other than white noise can dominate. In this chapter, noise measurement is carried out in an ionic system with emphasis in the picking up of the noise signature arising due to ionic contributions.

3.1 Noise in salt solutions

Noise is measured at typical concentrations in different ionic solutions. These solutions are

(i) KCl and $LiClO_4$
(ii) PSS and Nafion
(iii) $AgNO_3$ and NaCl
(iv) PbI_2 and $CH_3NH_3PbI_3$

3.1.1 KCl and $LiClO_4$

The noise is experimentally measured in the salt solution of KCl. The solution is prepared by adding a particular weight of KCl salt and a measured amount deionized (DI) water was used as a solvent in order to prepare a sample of known concentration.

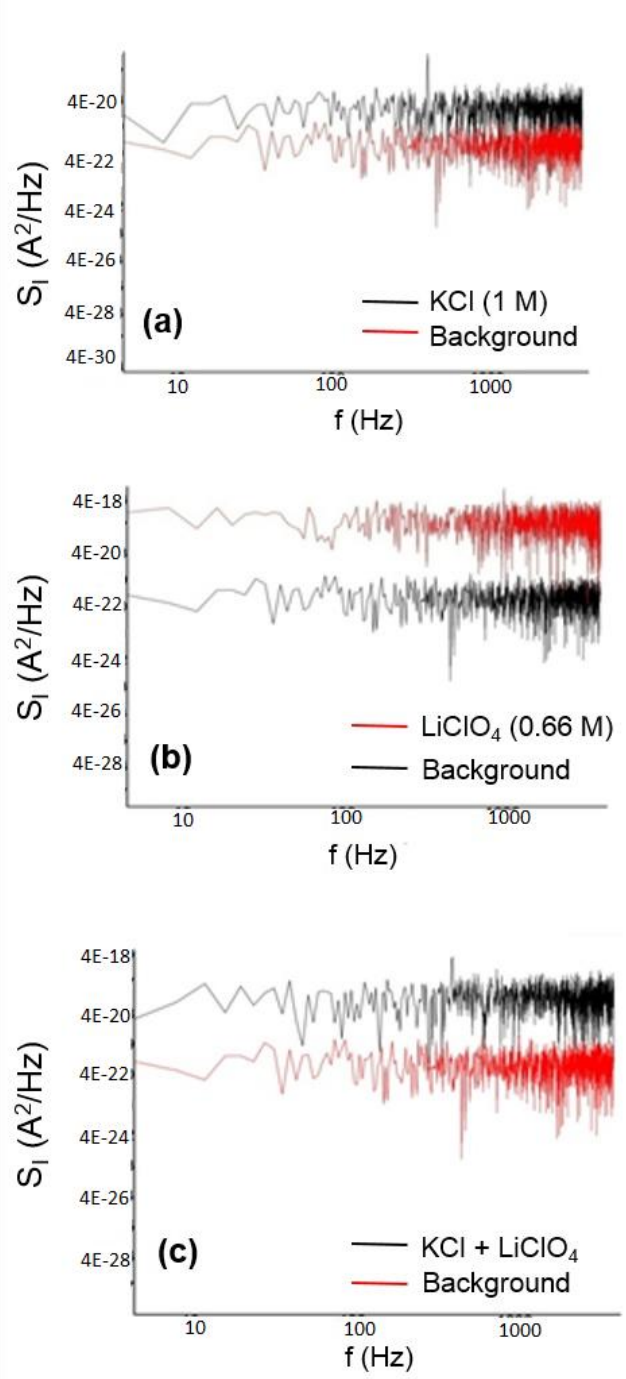

Figure 3.1 *Noise spectrum for KCl and $LiClO_4$ solutions. Noise spectrum from (a) 1M KCl solution (b) 0.66 M $LiClO_4$ (c) Mixture of KCl and $LiClO_4$.*

These measurements are recorded using a digital signal oscilloscope (Keysights MSO-X). A gain of 5 x 10^5 V/A is applied from the trans-impedance amplifier. Power spectral density (PSD) depicts current noise spectrum (S_I (A^2/Hz) in arbitrary units. In order to get the actual noise amplitudes, these arbitrary values should be divided by the square of the gain used from the pre-amplifier. For instance, in all three cases in figure 3.1, background noise (noise from

the instruments and experimental set) is of the order of 10^{-10} in PSD (Y-axis), which corresponds to the actual current noise amplitude of the order 4 x 10^{-22}. To ensure the contribution of noise from the fluctuations in ionic current only a very small amount of bias (< 100 mV) is applied during these experiments. In the case of figure 3, applied dc bias is 90 mV.

It can be seen that noise signatures are obtained from the ionic solution of KCl (figure 3.1), $LiClO_4$ (figure 3.2). The magnitude noise in case of $LiClO_4$ is significantly greater than that of KCl. Noise is also obtained from the solution of 1 molar concentration of KCl by adding some amount of 0.66 molar concentration of the $LiClO_4$ solution. The amplitude of noise, in this case, is more than that of KCl but less than the amplitude of noise in $LiClO_4$. It is to be noted that the nature of noise obtained is white. The values obtained in the case of the ionic solution of KCl and $LiClO_4$ are in agreement with the literature as white noise is observed in these systems. It has been shown earlier in the literature that noise observed in ionic systems like KCl and $CuSO_4$ is white in nature however in the case of impurities in the sample 1/f noise can be observed.[129-131]

3.1.2 Noise measurements in PSS and Nafion

Polystyrene sulfonates (PSS) and Nafion ($C_7HF_{13}O_5S.\ C_2F_4$) are the conductive polymers. Noise is measured in their ionic solution form. As can be seen from the figure 3.2, a substantial magnitude of noise above the background noise (no bias) under 60 mV bias is obtained.

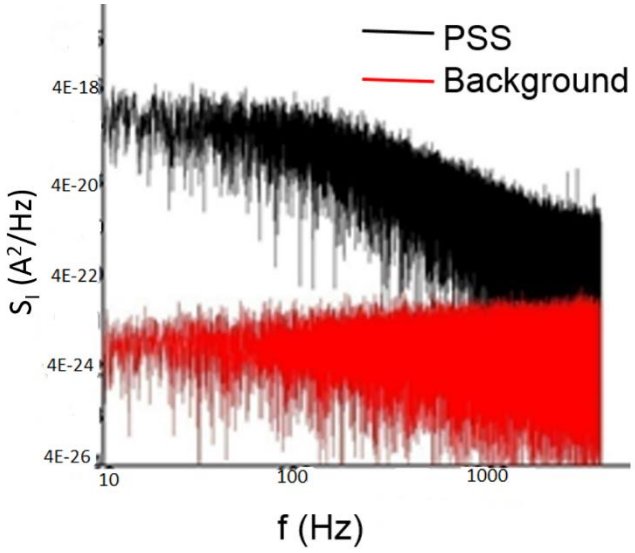

Figure 3.2: *Noise spectrum for PSS solution*

In addition to the white noise, the spectrum obtained in the case of PSS (figure 3.2) indicates the presence of generation- recombination noise. Several reports claim the occurrence of G-R noise in electrochemical systems.[132-134] For instance in a paper by Oldfield et. al, it is stated that the *"G-R noise results when a system undergoes a small fluctuation from equilibrium, then the inherent fluctuation in the number of ionic particles present caused by the generation recombination of the ions gives rise to a fluctuating current."*

Figure 3.3 represents the noise spectrum of a typical Nafion solution. The obtained noise only slightly high in amplitude is observed and again its white noise.

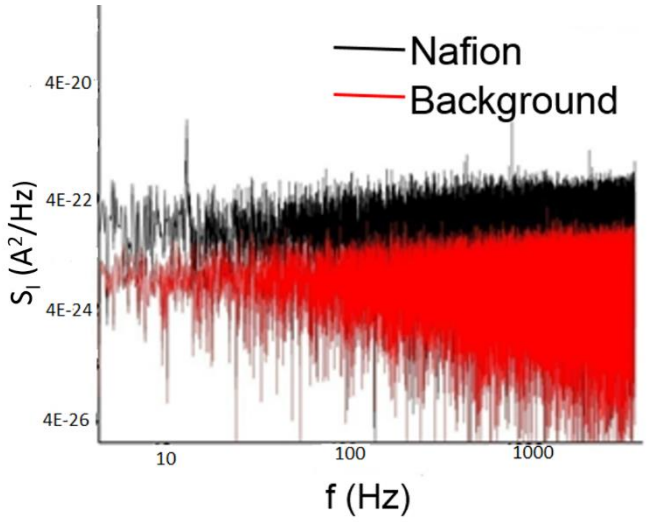

Figure 3.3: *Noise spectrum for a typical Nafion solution*

3.1.3 Noise measurements in $AgNO_3$ and NaCl solution

A precipitation reaction between an aqueous solution of silver nitrate ($AgNO_3$) and an aqueous solution of sodium chloride (NaCl) is closely studied. When the $AgNO_3$ solution is added to NaCl solution, a white precipitate of silver chloride (AgCl) is formed as shown in the equation below:

$$AgNO_3\,(aq) + NaCl\,(aq) \rightarrow AgCl\,(s) + NaNO_3\,(aq)$$

This reaction is monitored at different time intervals. As soon as the $AgNO_3$ was added to NaCl (t=0 mins.), from figure 3.4(a), some *1/f* noise features at the lower frequencies (< 1kHz). The noise measured from the same sample at t = 5 min, again shows some *1/f* noise feature.

However, the noise amplitude at 1Hz is slightly less than that at t = 0 min (figure 3.3 (b)). Finally, noise measured at t = 15 min shows no signature of *1/f* noise.

The possible explanation for such observation is that, during then initial stages of the reaction, when the $AgNO_3$ is added to NaCl the equilibrium of the system is shifted from the lowest energy state. The system is unstable at this stage as the precipitation is in the process. However, once the reaction is complete, and all the AgCl is settled down, the reaction is again in equilibrium, and now the observed noise is again white (frequency independent) in nature.

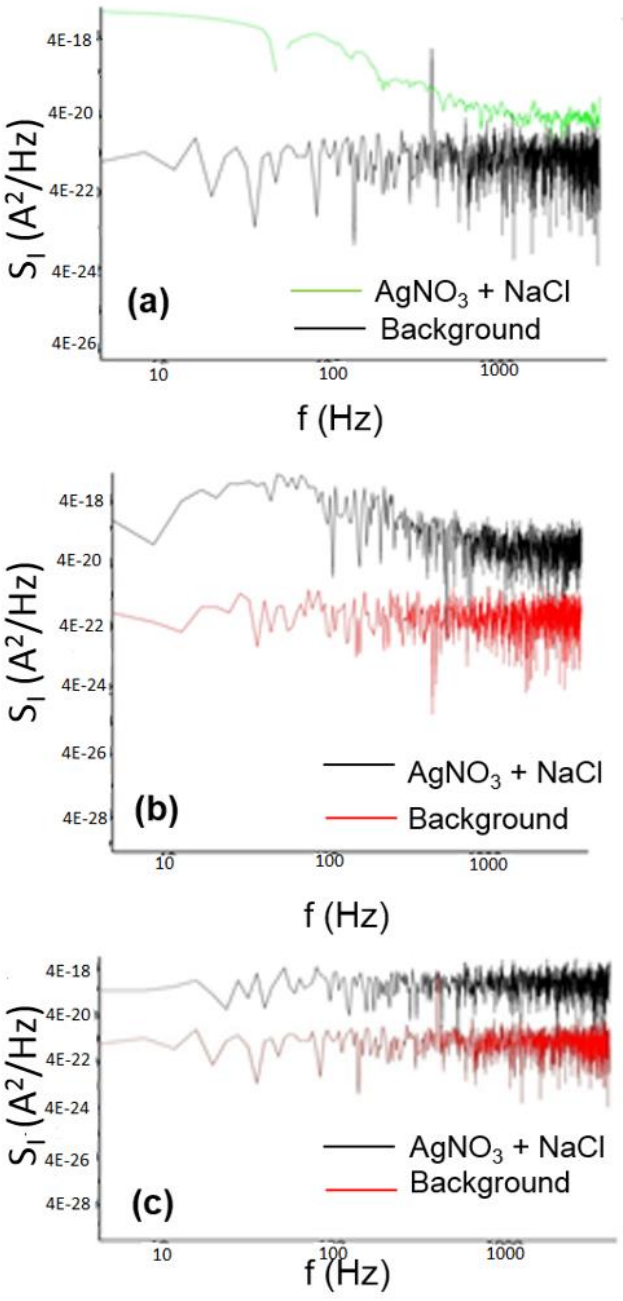

Figure 3.4: *Noise spectrum for $AgNo_3$ and NaCl solution (a) t = 0 min (b) t = 5 min (c) t = 15 min.*

3.1.4 Noise measurements in PbI_2 and $CH_3NH_3PbI_3$

Noise is measured from a solution prepared by adding lead iodide (PbI_2) to dimethylformamide (DMF). The obtained spectrum is depicted in figure 3.5. Similarly, noise is measured from a perovskite ($CH_3NH_3PbI_3$) solution in DMF (figure 3.6).

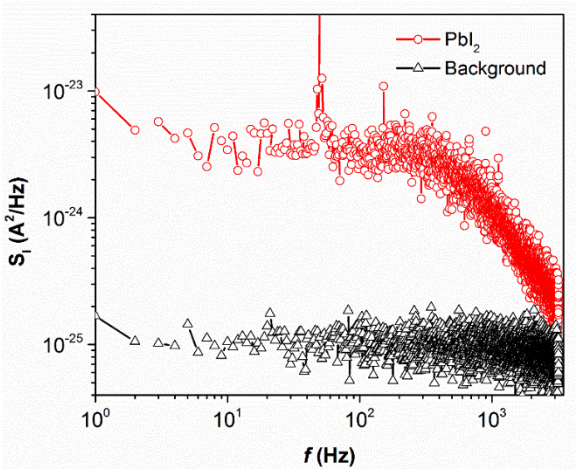

Figure 3.5: *Noise spectrum of PbI_2 solution (solvent DMF)*

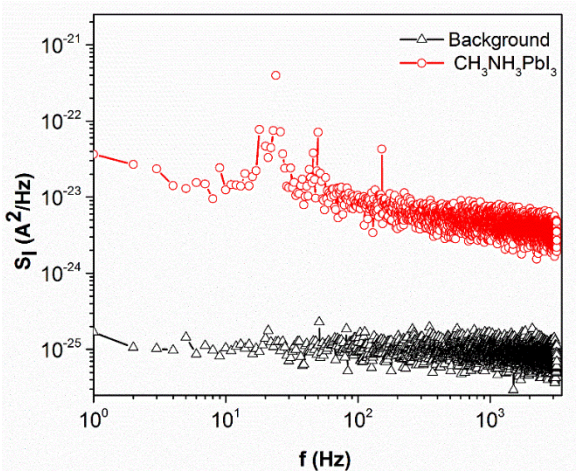

Figure 3.6: *Noise spectrum of Perovskite solution (solvent DMF)*

The spectrum reveals that it is possible to pick signatures of noise which are above the background noise just by the application of a small bias (in this case 50 mV). The observed Lorentzian in the noise spectrum can be argued to be an indication of generation and recombination noise, similar to what has been observed in the case of PSS earlier. The time series plot of PbI_2 is shown in appendix E, and it rules out the possibility of any random

telegraph noise (RTS noise). Noise amplitudes are significantly lower than that are observed in the case of perovskite solar cells.

3.2 Noise measurements in DSSCs

This section describes the noise spectroscopy of a dye-sensitized solar cell. The noise is measured for a spectral bandwidth of 51.2 kHz. A gain of 5 x 10^5 V/A is applied from the TIA. Since, the aim of the experiment is to check the signature of noise originating due to ionic transport, a very small bias of 10 mV is applied. The device is always kept under dark. From the figure 3.7, a significant amount of noise amplitude higher than the experimental setup background is seen from the device at 0 mV. However, at ten mV noise further, increases in amplitude with distinct *1/f* noise below 1 kHz (*1/f* fit is shown in the Appendix E).

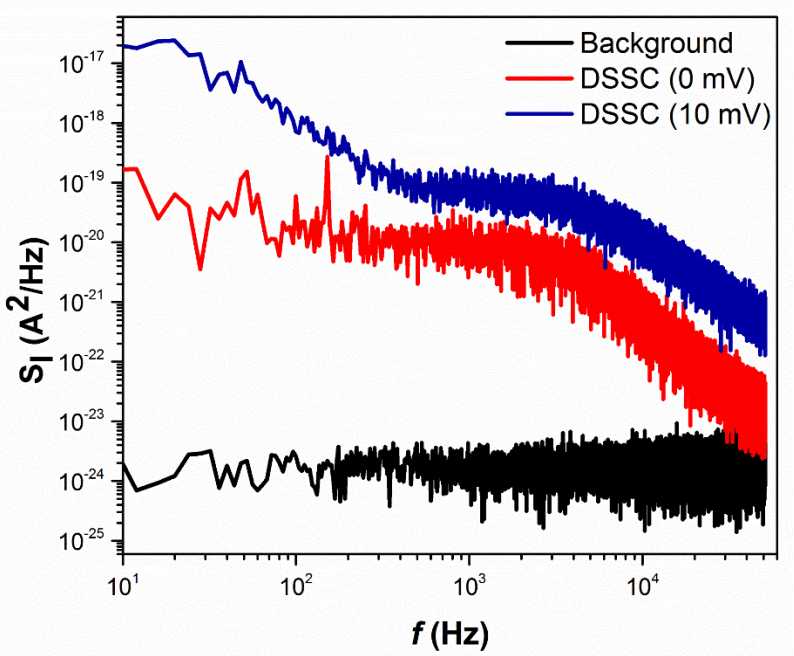

Figure 3.7: *Noise spectrum of a DSSC (η ~ 1.05 %)*

V_{oc} (Volts)	J_{sc} (mA/cm^2)	FF	η %
0.7	2.45	64.2	1.05

Table 3.1: *Table representing the parameters from a typical DDSC device used for noise measurements*

The noise is measured from the same device at a stage when it is substantially degraded (η ~ 0.06 %) (figure 3.8). In this case noise spectrum is different from the what was observed previously at the stage η ~ 1.05 %. A log-normal feature is observed with a peak centered around 2.5 kHz (log normal fit is shown in the Appendix E). This corresponds to the g-r noise. Recombination of carriers and their trapping at defects and impurities sites is the possible reason for such observed noise.[135]

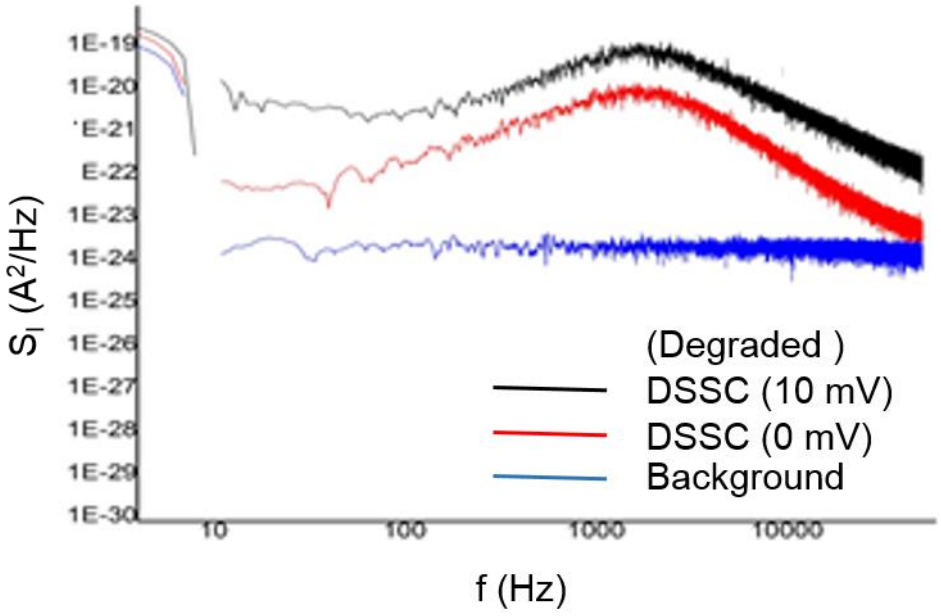

Figure 3.8: *Noise spectrum at degraded stage of the device (η ~ 0.06 %)*

From figure 3.9, spread in FWHM of the histogram can be seen, suggesting that fluctuations in current have increased with degradation.

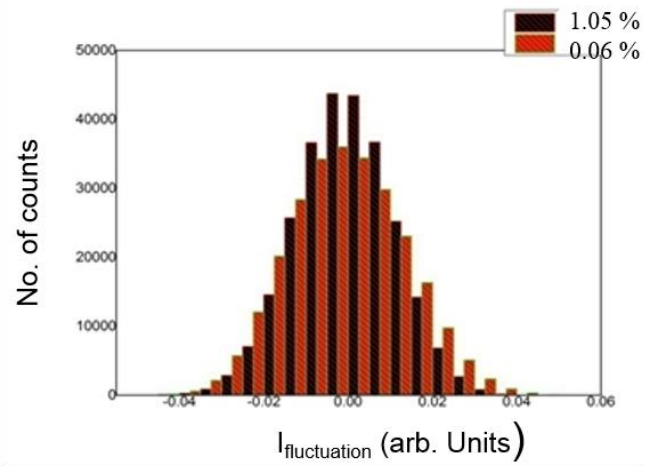

Figure 3.9: *Histogram showing the distribution from the DSSC device at two different degradation stages.*

3.3 Bias and history dependent studies in HOIP solar cells

In this section, noise is measured from perovskite solar cells of structure device type 1 i.e. FTO / TiO_2 / perovskite / spiro-OMeTAD. Hysteresis, which is readily observed in the case of perovskite solar cells is argued to originate due to various sources.[80,136-138] Among many proposed theories, ion migrations in HOIP have been hypothesized as a cause of hysteresis.[139] Here noise is measured from the devices by changing the device history. The aim of these experiments is to observe any variation in the noise spectra with a change in the prior bias history.

3.3.1 Bias dependent noise in dark and light in HOIP solar cells

Before the history dependent studies, perovskite solar cells are studied under small bias (10 mV). A consistent *1/f* noise is observed on bias application both in the dark and in the light. However, with illumination (1mW/cm^2) along with the bias, an increase in the noise magnitude is observed. Also, there is a cross-over in frequency. *1/f* is prevailing over the higher frequency range. This measurement is taken over a broad frequency range of 51.2 kHz. Significant *1/f* noise in the dark may have a contribution from the ionic transport, as only a small bias of 10 mV is leading to a clear *1/f* noise. This is further explored in the next section.

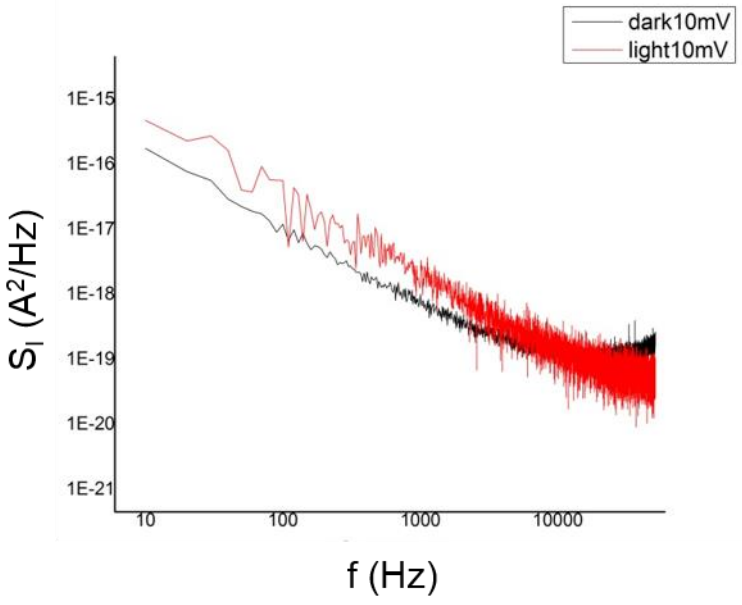

Figure 3.10: *Noise spectrum of a typical perovskite solar cells under the influence of a small bias of 10 mV in dark and light*

3.3.2 History-dependent studies

In order to see any evidence of ion migration in perovskite solar cells through the noise. The experiments are performed with the following steps:

(i) A bias (positive or negative) is applied to the device for a given time interval (30 s to 120 s) in the dark.

(ii) Immediately after the applied bias is discontinued light (1 mW/cm^2) is turned on.

(iii) Noise is measured from the device under the influence of light (no bias) but with the biased history.

Following the above procedure, DC characterization is also performed to see the changes in the device performance with the bias application. Figure 3.11 shows the current vs. time, *I(t)*, the plot for a device which is exposed to a bias of 0.6 V for 60 s. The plot reveals that there is a gradual increase in the value of current with time. This slow increase in the current could originate from the ionic transport within the device.

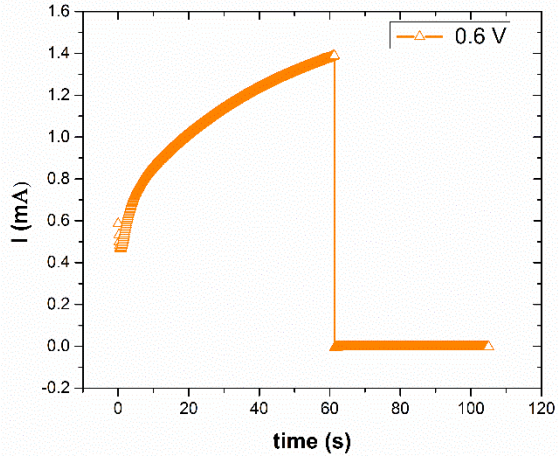

Figure 3.11: *I(t), Bias of 0.6 V was applied for 60 s prior to illumination*

Similarly, in figure 3.12, a negative bias (-1.2 V) is applied for the 60s. Current moves in the opposite direction (downwards) with gradually increasing in magnitude. However, the moment bias is off (and the lights are turned own) current approaches a positive value and becomes constant. Again such slow transport over a time span of seconds provides a good indication of ionic activity in the intrinsic transport of the devices.

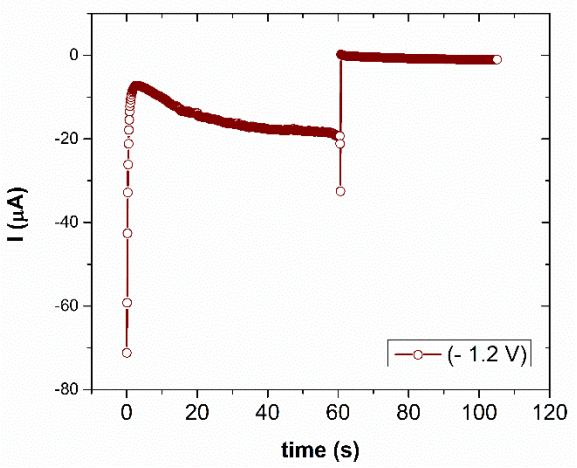

Figure 3.12: *I(t),* *Bias of (-1.2) V was applied for 60 s prior to illumination*

Noise spectrum for positive bias history is shown in figure 3.13. Since the measurement is taken from the same device and at its particular stage of device performance (PCE); ideally, noise spectrum should be identical. However, with the application of bias prior to the noise measurements seems to affect the noise spectrum.

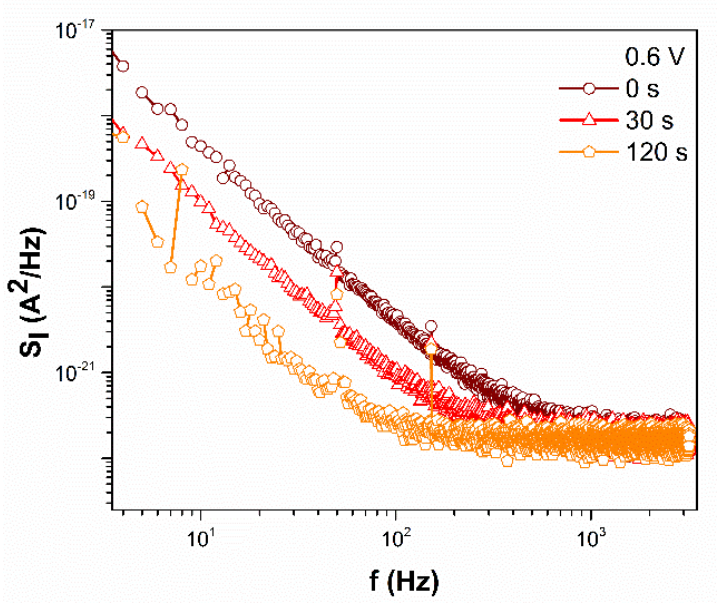

Figure 3.13: *Noise spectrum on changing the device history. The positive bias of 0.6 V is applied (under for different time intervals (0s, the 30s, 120s), before the measurement of light which results in distinct noise spectrum.*

This effect is seen even in the case of negative bias application, as depending upon the different time of bias history, different noise spectrums are observed (figure 3.14).

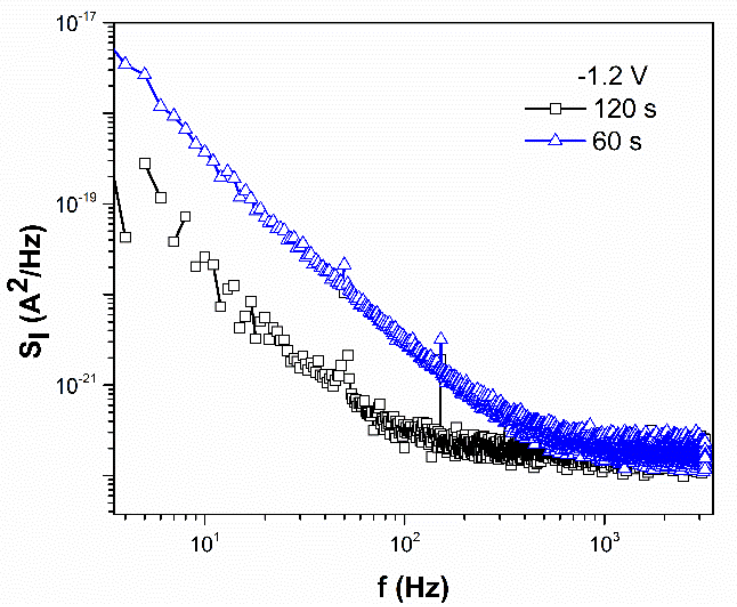

Figure 3.14: *Noise spectrum on changing the device history. A negative bias (-1.2 V) is applied (under for different time intervals (, the 60s, 120s), before the measurement of light which results in distinct noise spectrum.*

Even though bias history seems to have an effect on the noise spectrum, direct correlation or any concrete trend in the noise profile is not clearly established. Nevertheless, noise measurements appear to give significant information about the charge transport as demonstrated by the distinct noise spectrum for different bias history and from the DC characteristic.

3.4 Summary

In this chapter, noise measurement is attempted on the ionic systems with a major focus on the picking up the noise signals from the pure ionic transport. As evident from the noise spectroscopy of different ionic solutions such as KCl, LiClO4, Nafion, and perovskite, white noise dominates in these systems. In case of PSS and PbI_2 additional Lorentzian features are observed. The origin of Lorentzian is argued to be originated from the generation and recombination of the ions. However, in the case of some active reactions like in the case of $AgNO_3$ and NaCl, *1/f* noise can dominate for some part, depending upon the state of the reaction. Ionic systems behave differently in the presence of other constituents like in the case

of a functional device. In DSSC both the *1/f* and g-r noises are observed with distinct noise characteristics for working and the degraded states.

Another highlight of the noise measurements in ionic solution is that the noise amplitudes of PbI_2 and perovskite solutions are found to be significantly lower than the noise in HOIP devices. Bias depended on a study on the perovskite solar cells showed that consistent *1/f* noise over a large frequency range could be obtained in the dark with a small bias (10 mV). Finally, history dependent studies suggest the role of ionic movement in the carrier transport in the device and they seem to influence the device with effects like hysteresis. If a direct correlation between the history of bias application and corresponding noise spectrum is established, then noise can be very helpful in following up with the trajectory of the ionic movement within the device.

Chapter 4

Noise measurements in different structures of hybrid organic-inorganic perovskite solar cells

In a complex system like hybrid perovskite solar cells, a characteristic response corresponding to each physical process can have a signature in the noise characteristics. Intrinsic microscopic processes such as effects from a discrete set of traps can get reflected at the macroscopic level in the form of fluctuations. Deviations from a constant magnitude (time independent), steady state response upon continuous photoexcitation are reflected in the photocurrent fluctuations. A multidimensional stochastic variable can be formed mainly due to the charge carrier trapped at different energy states. In perovskite solar cells, contributions from trap states in the bulk active layer, interface states and ionic effects are expected, the relative proportion of each source is dictated by the device history and conditions. The time-dependent fluctuations in photocurrent $I_{ph}(t)$, give significant insight into the charge carrier transport dynamic and can be analyzed in terms of power spectrum density (PSD) in the frequency domain. $I_{ph}(t)$ snapshots taken at various stages of the device provides the trajectory of the degradation process. In this chapter, noise studies are carried out from three different type of hybrid perovskite solar cells.

4.1 Significance of intensity-dependent noise spectroscopy

Photoexcitation is one of the cleanest ways of introducing excess charge carriers in the device due to the significant photocurrent of magnitude several orders higher than the dark background current. The excess carrier generation, transport, and extraction constitute a random process. The recombination lifetime limited transport mechanism in clean systems is inherently a

statistical process and is signified by a characteristic noise form. It's PSD can be expressed in the Lorentzian form[113]: $S_I(f) = \frac{S_0}{[1 + (2\pi f\tau)^2]}$, where S_0 is the frequency independent part of $S_I(f)$ and τ is the recombination lifetime. This observation can yield relevant trap parameters, such as the capture cross-sections, energy positions, and trap densities. However, in realistic systems this response is significantly altered due to variety of other sources of noise. Thermal fluctuations (white or Johnson noise), are always present and are signified by their frequency independent profile[140]. Presence of multitude of defects of various types especially in aged or degraded or amorphous samples eventually results in an apparent featureless *1/f* profile. The ionic motion contributes to the fluctuation within the film can contribute to the fluctuation in a distinct way. However, the *1/f* noise model is an effective diagnostic tool for quality and reliability test of semiconductor devices[141], and importantly, it can be correlated to the degradation of the solar cell devices[142]. Current fluctuations[143] ($\Delta\sigma = \Delta(qn\mu)$) can broadly be classified in terms of the fluctuations in charge carrier density (ΔN model) or mobility fluctuations ($\Delta\mu$ model)[112,127]. Bulk related *1/f* noise has been attributed to the carrier number fluctuations due to the random trapping and de-trapping events. Numerical methods have been reported which allows one to determine the parameters of the Lorentzian noise spectrum of single trap models as a function of position, energy and bias conditions. The presence of traps in solar cells with appropriate energetic distribution and concentration contribute to the variation in the current in a discretized manner[144]. Fluctuations associated with a realistic trap mediated transport model can be simulated using kinetic Monte Carlo procedure and upon comparison with the PSD in the measurements, the trap density, kinetics and energetics can be estimated. Through detailed modeling using kinetic Monte-Carlo, it is earlier shown in BHJ systems that the $1/f^{\alpha}$ behavior may be understood within a wide uncorrelated Gaussian disorder model with a threshold mobility edge[117].

As evidenced in most analysis, the light intensity serves as a useful parameter to evaluate the transport process of the photo-generated carriers. The measurements in these studies are carried out for different devices (efficiency) at various stages of performance. They are carried across a large number of cells to arrive at a conclusive trend. J_{sc} typically increases with intensity in all the devices, and this trend is shown in Figure 4.1. In all the devices, fluctuations proportional to the light intensity *(P)* is observed with an *S(f)* exhibiting a P^{β} behavior.

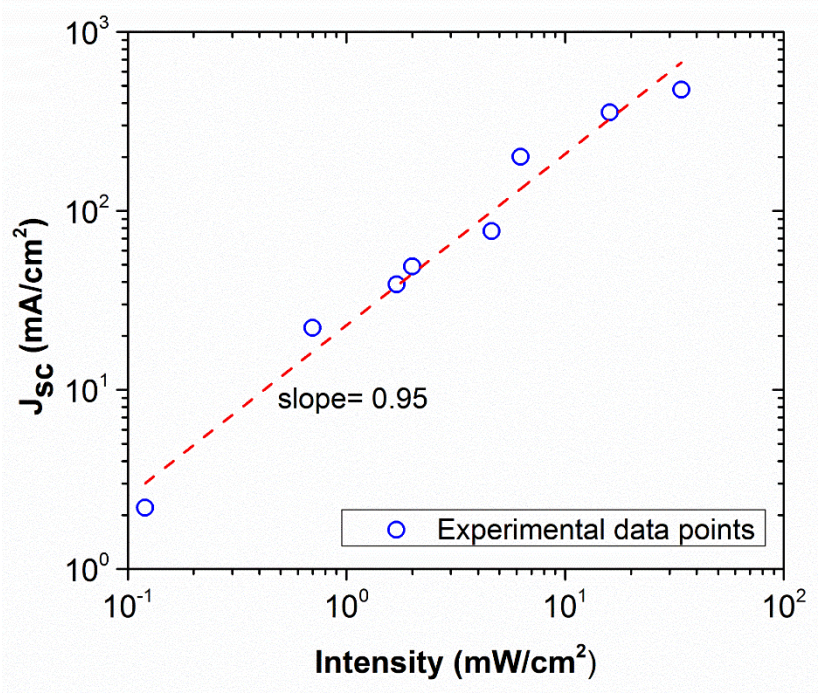

Figure 4.1: *Representative image from a typical device, showing a linear dependence of J_{sc} on Intensity.*

4.2 Time series analysis

Time series data gives the primary information about the fluctuation trend from any device. The characteristic fluctuations for different structures of HOIP solar cells may vary from each other. During noise measurements, the data is first recorded in the time series, and then it is processed using FFT to get noise PSD. Although major noise analysis is done by the obtained PSD however, time series data itself can be very informative. Distinct fluctuations from a particular device can be from the measurements in dark and under illumination. The amplitude of dark fluctuations acts as a background and is almost same for every case, but as soon as the device is illuminated, sharp photocurrent fluctuations larger than the dark fluctuations are clearly observed.

Figure 4.2 shows the time series data from different devices under dark and similar illumination conditions. This figure shows the typical pattern of photocurrent fluctuations in the three structures of hybrid perovskite solar cells studied. A qualitative trend of the noise levels magnitude associated with different geometry is apparent, with the presence of significant noise in regular TiO_2 (Device 1) based structures and relatively low-noise in the inverted structure. The variation in the fluctuations for the different devices can be appreciated qualitatively by the variance/ standard deviation analysis as shown in table 4.1.

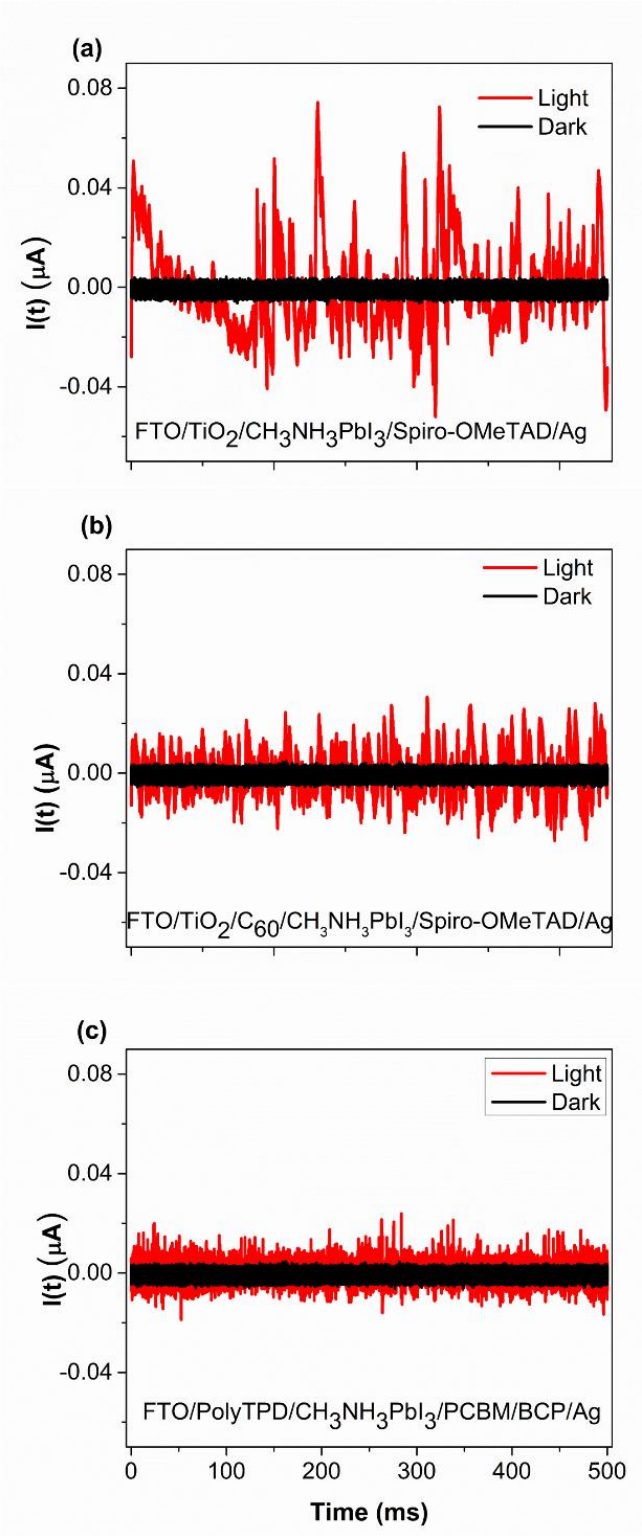

Figure 4.2: *Typical Current I(t) time series recordings from representative samples of the three device structure under similar dark and light conditions and represents the initial device state for noise studies. (a)FTO / TiO_2 / $CH_3NH_3PbI_3$ / Spiro-OMeTAD / Ag (b) FTO / C_{60} / $CH_3NH_3PbI_3$ / Spiro-OMeTAD / Ag (c) FTO / Poly-TPD / $CH_3NH_3PbI_3$ / PCBM / BCP / Ag. The time duration for the capture of one data frame is 0.5 s, and 80 frames were recorded for each dataset.*

Devices	Standard deviation
Device 1	1.8×10^{-8}
Device 2	8.4×10^{-9}
Device 3	2.8×10^{-9}

Table 4.1*: Standard deviation from the three devices (averaged over 327680 data points in each case)*

The low level of fluctuations as observed in the time series plot of the inverted structure device suggests that they are relatively more stable against the exposed light (figure 4.2 (c)), in contrast, device 1 (figure 4.2 (a)) is highly sensitive towards the illumination. Considering significantly large amplitudes of noise than the other structures, they can be expected to degrade faster over prolonged illumination. Thus, relative stability can be compared with noise.

4.3 Noise measurements in FTO / TiO_2 / $CH_3NH_3PbI_3$ / Spiro-OMeTAD/ Ag (conventional structure, Device type 1)

The noise studies from one of the most standard structures of HOIP solar cells is carried out in in this section. Multiple devices were experimented and results from one typical device representing the conventional structure of FTO / TiO_2 / $CH_3NH_3PbI_3$ / Spiro-OMeTAD / Ag is presented here. This device is named device 1 for simplicity and further reference in the thesis.

Experimental Protocols:

Following experimental procedures are followed for the noise measurement in all the cases including experimental results in the next sections.

- Measured frequency range: 2 Hz to 3.2 kHz
- Gain from the trans impedance preamplifier: 5×10^4 V/A
- Time duration for capture of one data frame: 500 ms
- Number of data –frames per dataset: 80
- Total time of recording of one complete data set: 40 s
- Resolution lines in the DSA: 1600

Results and discussion

Figure 4.3 to 4.6 summarizes the device 1 characteristics. Typical *J(V)* characteristics prior to the noise measurements are shown in Figure 4.3, and the inset shows the details of each layer in the structure of the device.

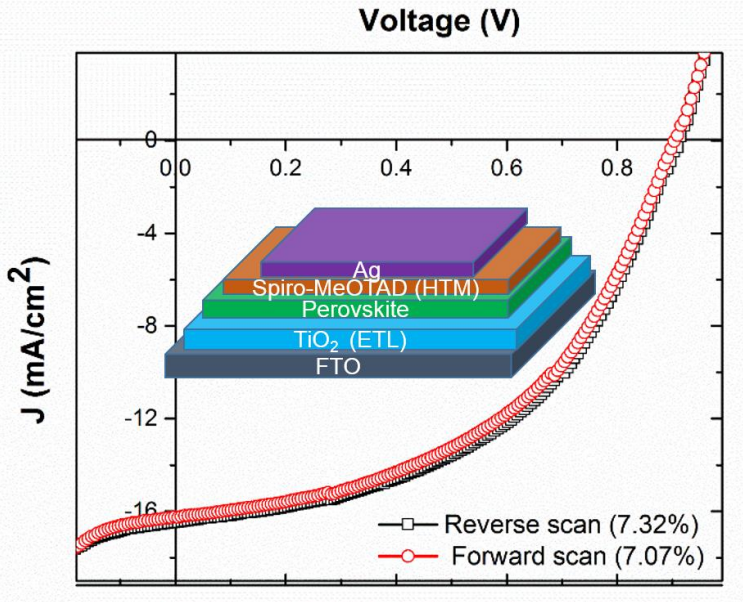

Figure 4.3: *(Device 1) J(V) characteristics in forward and reverse scan (inset shows the details of the device structure.*

Effect of illumination on *I(t)* fluctuations is indicated in the normalized amplitude histogram distribution (Figure 4.4), which exhibits a Gaussian form with the Full-width half maxima (FWHM) increasing with intensity.

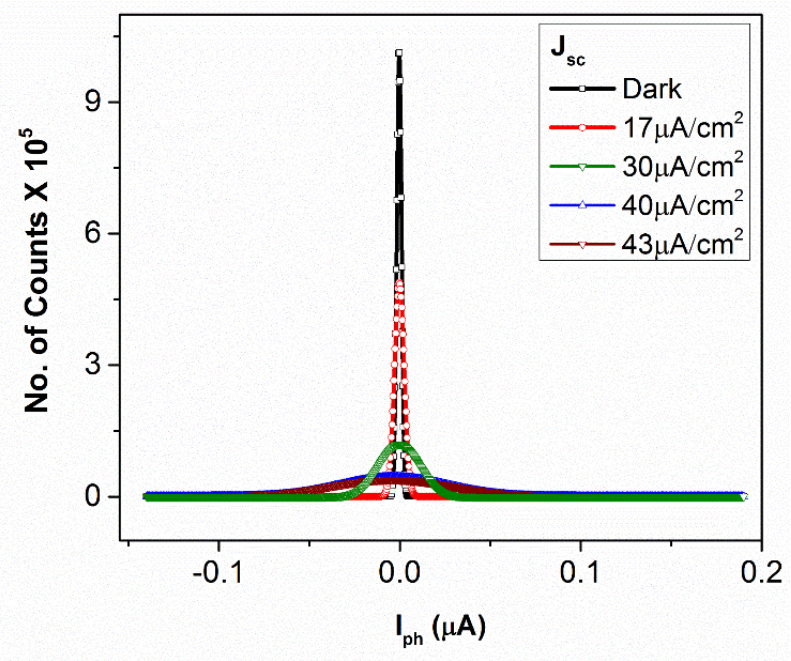

Figure 4.4: *Distribution function of current amplitude fluctuation histogram under dark and different intensities (J_{sc} values) of white light.*

The spread in the FWHM with increasing J_{sc} indicates the increase in photocurrent fluctuations. In the case of dark I_{ph} is centered close to zero, but with increasing intensities, it gets widened (increase in fluctuations).

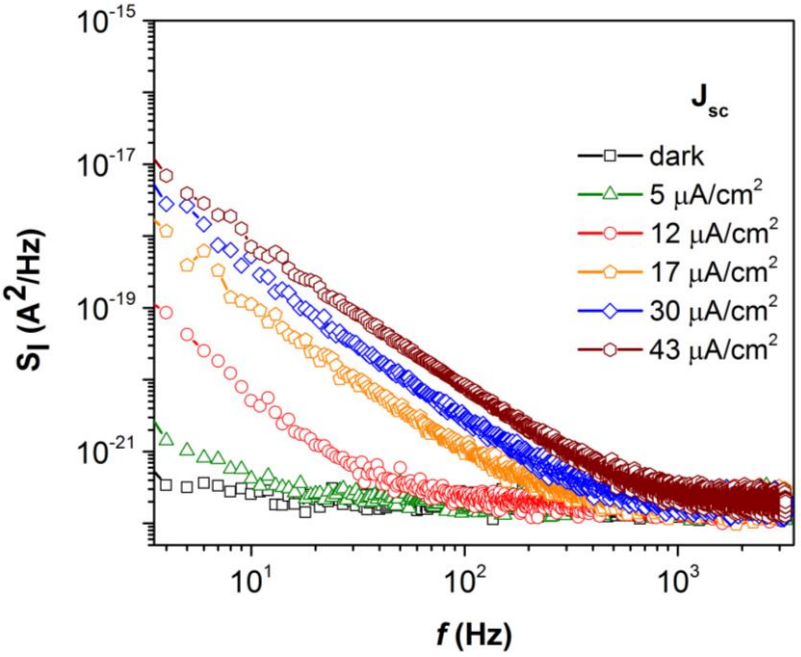

Figure 4.5: *power spectrum density (PSD) $S_I(f)$ at different intensity/J_{sc}.*

Figure 4.5 depicts the noise spectrum from the device 1. A consistent *1/f* noise is observed at all J_{sc} (intensity) values. The noise is analyzed using the simple Hooge's relationship:

$$S_I(f) = A\frac{I^2}{f^\alpha} \qquad (4.1)$$

where 'A' is a constant, corresponding to a noise magnitude and can be obtained directly from the noise spectrum plot using power spectral density (PSD) amplitude at a given frequency. α values can be obtained by fitting the noise spectrum (obtained from the experimental data) by using equation 4.1.

An increase in the magnitude of PSD can be seen with increasing J_{sc} with α ~1.9 in $1/f^\alpha$. The high value of α suggests that the main source of noise appears to be due to carrier number fluctuation. As light intensity increases, the noise magnitude gradually tends to get saturated beyond a certain intensity *(J_{sc})*, and indicative of filling up of the trap states[118]. A crossover in frequency (cut-off frequency for *1/f*) can also be observed. With increasing intensities, *1/f* feature spreads over higher frequencies.

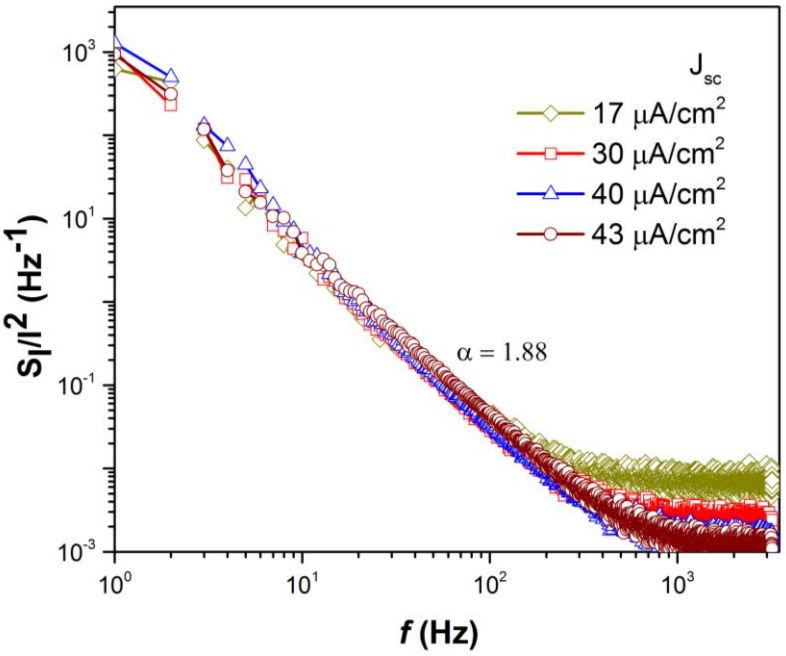

Figure 4.6: *Normalized power spectrum density ($(S(f)/I^2)$, to highlight the low-f universal behavior, the inset shows the observed linear dependence of J_{sc} on Intensity.*

Another useful way to analyze the noise spectrum is by using modified Hooge's equation to get the normalized noise:

$$S(f) \propto \frac{S_I(f)}{I^{\beta}} \propto \frac{1}{N\, f^{\alpha}} \tag{4.2}$$

where 'N' is the number of charge carriers. The generally accepted value of β is 2. However its value can be calculated from the experimental data by plotting J_{sc} against the noise PSD. The slope of the linear fit gives the tentative value of β (an example of calculation of β is discussed in the next section). The β values for the currently studied structure ranged between 2-2.5. The normalized noise which is the scaled PSD exhibits a universal behavior (figure 4.6), with all the different intensity response profiles collapsing to a single profile in the low-frequency range. Normalized noise spectrum is important in the case of the degradation studies. The values of α and β provide insights about the intrinsic mechanisms in the device. B gives the information about the mixing of the noise from the various sources and to differentiate between the surface (β ≈ 1)and the bulk effects ((β ≈ 1.5 -2).[126,145] A value can be related to the distribution of the trap states and to point out the dominating source of fluctuations (carrier number or the mobility fluctuations). The α ≈ 1 suggests that the trap states are uniformly distributed.

Similar analytical model is applied in the study of other two structures as well. The normalized power spectral density (NPSD) depicted throughout the thesis is calculated by using the following equation:

Calculation of normalized PSD:

$S(f) = S_I(f)/ (J^{\beta} \times 10^{-22})$. 10^{-22} is a used normalizing constant in each case.

4.4 Noise measurements in FTO / TiO_2 / C_{60} /$CH_3NH_3PbI_3$ / Spiro-OMeTAD/ Ag

(conventional structure, Device type 2)

Results from another device with conventional structure but with a different combination of electron transfer layer (ETL) is presented here. In device 2, an additional layer of C_{60} is present along with TiO_2 as ETL. The noise characteristics of device 2 are represented in figures 4.7 to 4.10.

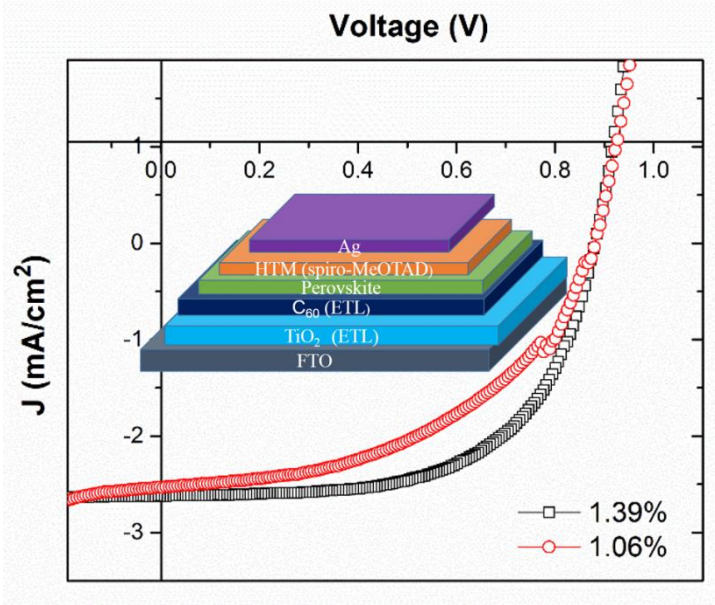

Figure 4.7: *(Device 2) J(V) characteristics in forward and reverse scan (inset shows the details of the device structure.*

J(V) characteristics in forward and reverse case is depicted in figure 4.7 with details of the device structure in the inset. Light-induced noise contribution is observed here as well. $I_{ph}(t)$ reveals the spread in FWHM maxima (Figure 4.8) of the noise amplitude with increasing light intensity. It is to be noted that the device PCE, in this case, is significantly lower than what was observed in freshly prepared samples.

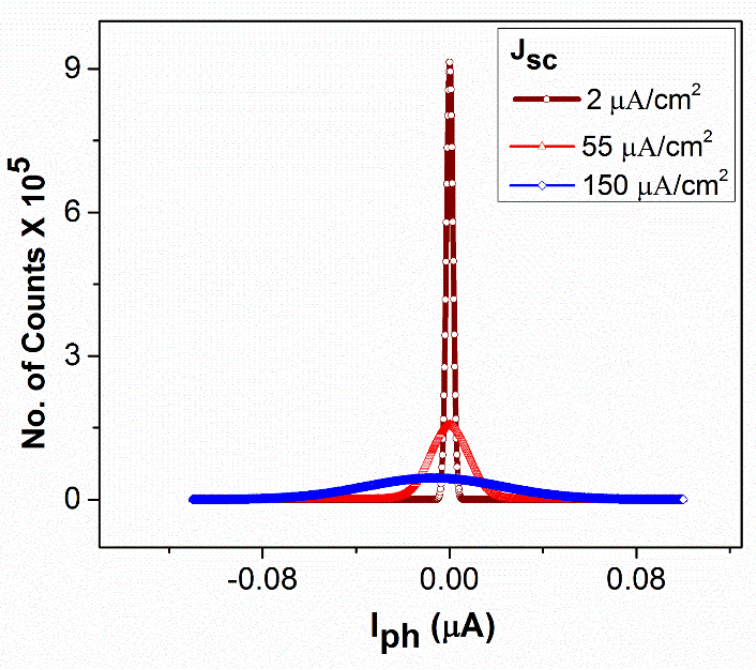

Figure 4.8: *Distribution function for device 2 in the dark and two different intensities.*

Noise spectrum with regions of two different α values in $1/f^{\alpha}$:

PSD observed in the case of device 2 is different from that of the device 1 discussed in section 4.3. A cross-over in *1/f* cut-off frequency is observed with increasing J_{sc}. However, unlike device 1, the *1/f* noise spectrum is not consistent in this case.

Noise spectrum (Figure 4.9), for this structure, reveal $1/f^{\alpha}$ behavior with different α in two distinct regions. α is higher (~2) in the low-frequency regime (<100 Hz) and is close to 1 in the high-frequency regime (> 1 KHz). This feature is indicative of at least two dominant processes with different time constants contributing to the noise[140]. Noise observed at lower frequencies with high α values can be related to both the interface states and grain boundaries and noise at higher frequencies exhibiting α~1 is largely representative of trap-limited bulk transport processes[146].

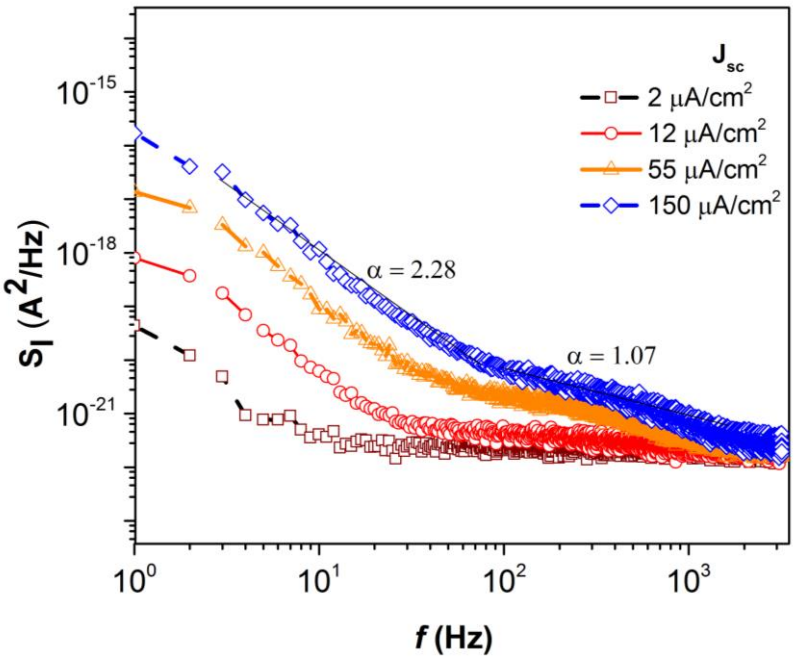

Figure 4.9: *power spectrum density (PSD) $S_I(f)$ at different intensity/J_{sc} for FTO / TiO_2 / C_{60} / $CH_3NH_3PbI_3$ / Spiro-OMeTAD / Ag*

Normalized noise $(S(f))/I^{\beta}$ in Figure 4.10 again indicates a unified behavior at low frequency. It is to be noted that the value of β ~1.6 in these devices, and the $S(f)$ is scaled by $((J_{sc})^{1.6})$.

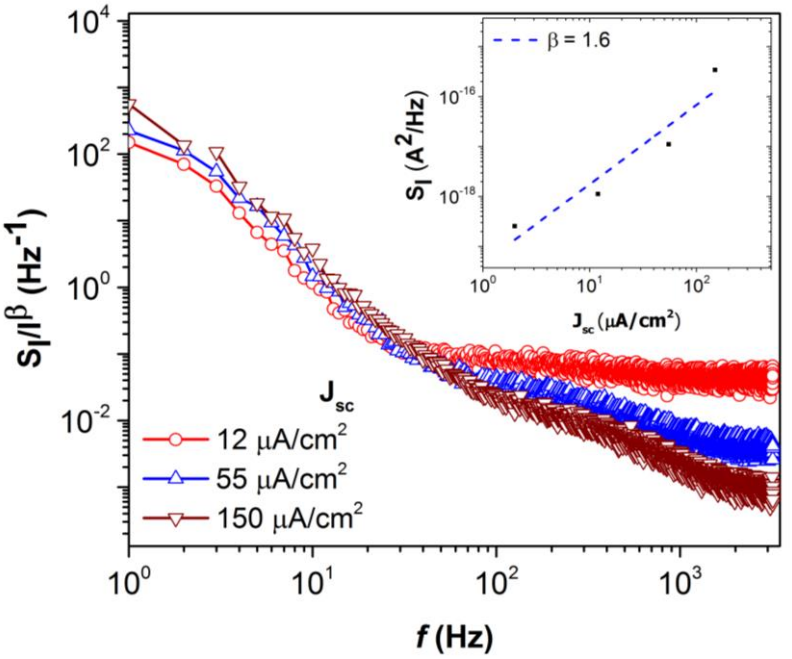

Figure 4.10: *Normalized power spectrum density ($(S(f)/I^{\beta})$, to highlight the low-f universal behavior. The inset depicts the noise power as a function of intensity to estimate β (~ 1.6 at 1 Hz).*

4.5 Noise measurements in FTO / Poly-TPD / $CH_3NH_3PbI_3$ / PCBM / BCP / Ag

(inverted structure, Device type 3)

Devices with the inverted structured as already discussed in section 4.2 are found to be relatively more stable and exhibited high PCE values. This allows the monitoring of the device and closely study the degradation trend. In this section, results from a typical device, which had over 15 % efficiency to start with are studied. Measurements from this device were also taken at its different stages of degradation and are discussed in the next section (section 4.6).

Figure 4.11 shows the JV characteristics with detailed structure of the inverted structure device. The experimental results from a representative device (device 3) are presented here.

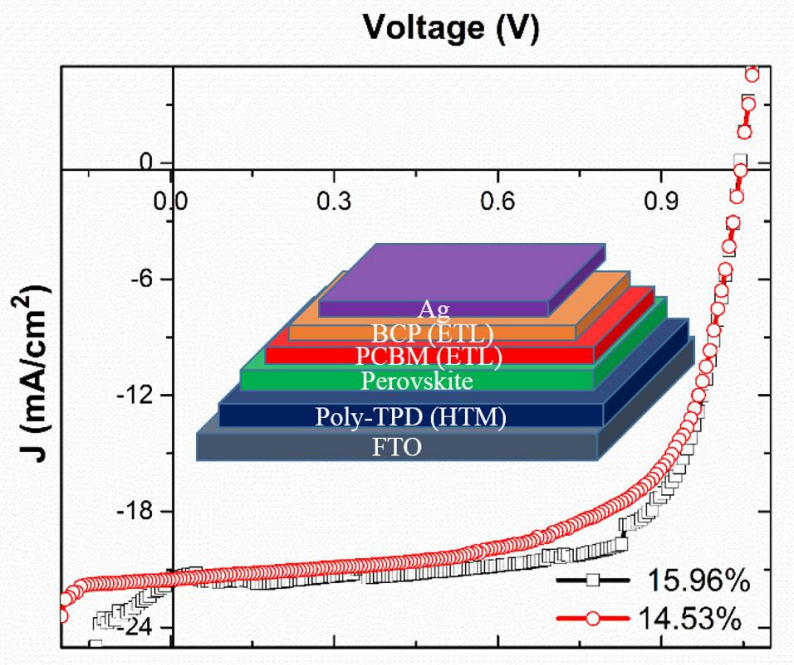

Figure 4.11: *(device 3) J(V) in forward and reverse scan – initial state of the device (b) PSD at different intensities/J_{sc} values, PCE of ~15%.*

The normalized distribution of current amplitude histogram is depicted in figure 5.12. The trend of the spread of FWHM with increasing intensity is consistent even in this third structure. However, the magnitude of $|I_{ph}|$ is relatively lesser than the other two structures (device 1and 2).

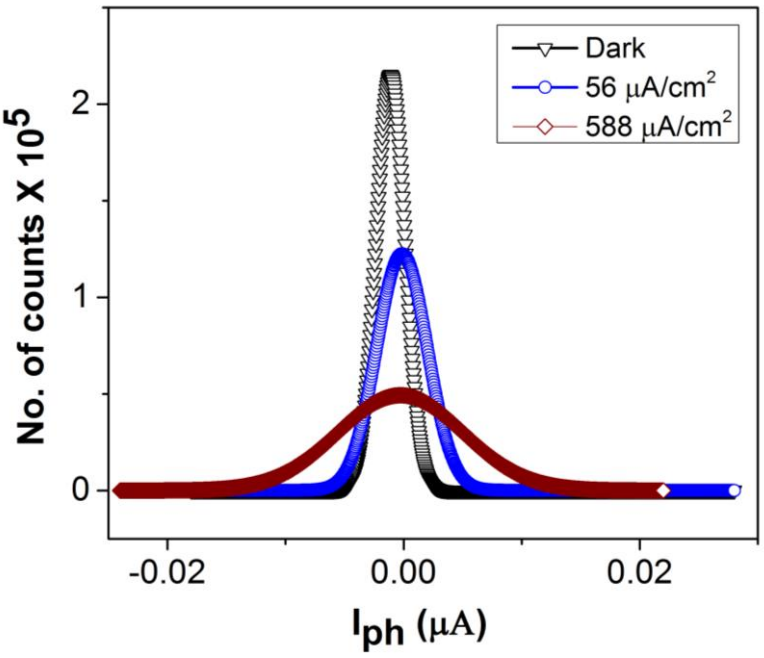

Figure 4.12: *Distribution function of current amplitude fluctuation histogram at different intensities for device 3.*

Observed generation-recombination (g-r) noise:

Figure 5.13 shows the noise spectrum for an inverted perovskite solar cell (device 3). The highlight of the noise results from this device structure is that unlike the case of device 1 and device 2 in addition to the *1/f* noise features, generation-recombination noise is also observed. The relatively low noise associated with the device enables observation of g-r noise at low-medium intensities (J_{sc} values 5μA/cm^2 and 56 μA/cm^2). At higher intensity (J_{sc}> 170 μA/cm^2), the *1/f* noise covers the range with α~1. A basic qualitative scenario for this trend of crossover of PSD profile as a function of intensity inefficient devices can be interpreted in terms of localized traps and the associated charge trapping and de-trapping kinetics.

In a high-performance device, when the degradation level is low, and the stability is high, noise signatures other than the *1/f* can be picked up. This is possible because trap/ defect density during the high PCE stage is low. *1/f* (with α~1) indicates the trap states are uniformly distributed, and the noise contribution is from the bulk. During low bulk trap density, noise from localized trap may dominate and get reflected in noise spectrum. So the observed g-r noise at intermediate intensities can be explained by a single trap model. Further, analysis of g-r noise can give information about the recombination lifetimes, capture cross-section and energetic profile of different carrier transport processes.

$$S_I(f) = \frac{S_0}{[1 + (2\pi f\tau)^2]} \tag{4.3}$$

where S_0 is the frequency independent part of $S_I(f)$ and τ is the recombination lifetime.

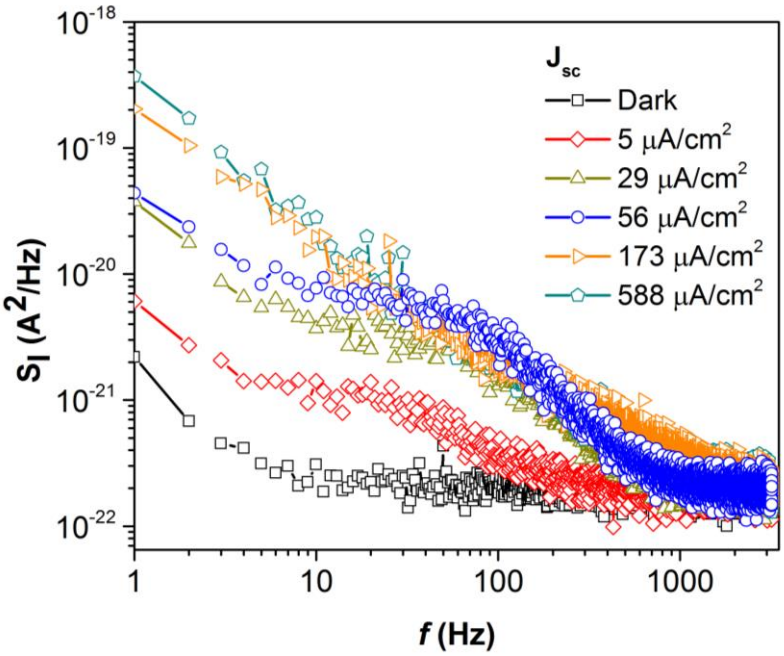

Figure 4.13: *PSD at different intensities/J_{sc} values, PCE of ~15% for FTO / Poly-TPD / $CH_3NH_3PbI_3$ / PCBM / BCP / Ag (inverted structure).*

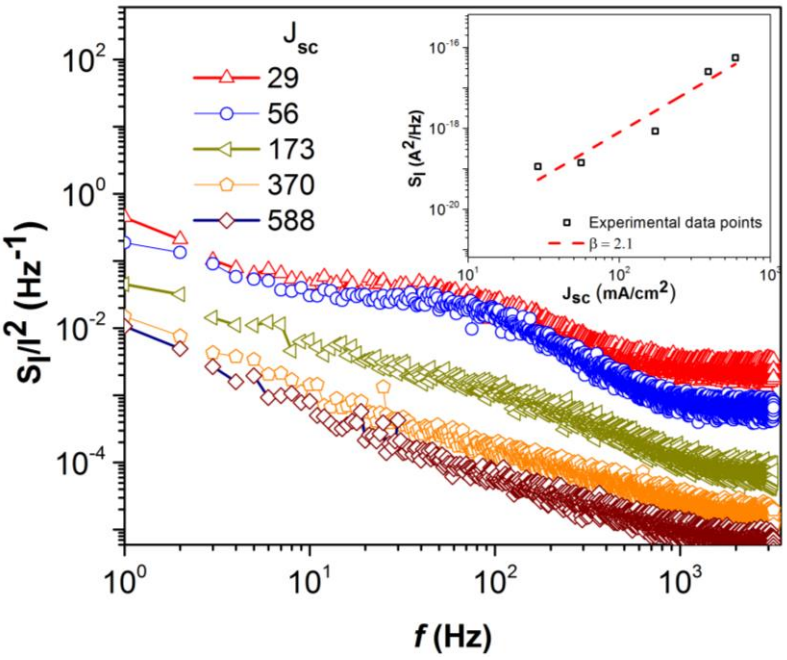

Figure 4.14: *Normalized power spectrum density ($(S(f)/I^{\beta})$, to highlight the low-f universal behavior. The inset depicts the noise power as a function of intensity to estimate β (~ 2 at 1 Hz).*

The NPSD for the device 3 is shown in the figure 4.14. Evaluation of β is depicted in the inset. The device 3 is further investigated for degradation.

4.6 Degradation studies

In figure 4.15, noise spectrum can be seen in the final stage of device degradation when the efficiency z < 0.1%). For this measurement, the device was exposed to slightly higher intensity (50 mW/cm^2) in order to check the point of noise magnitude saturation. A crossover in noise frequency response is observed with increasing intensities. However, the *1/f* behavior is now uniform with α~1.

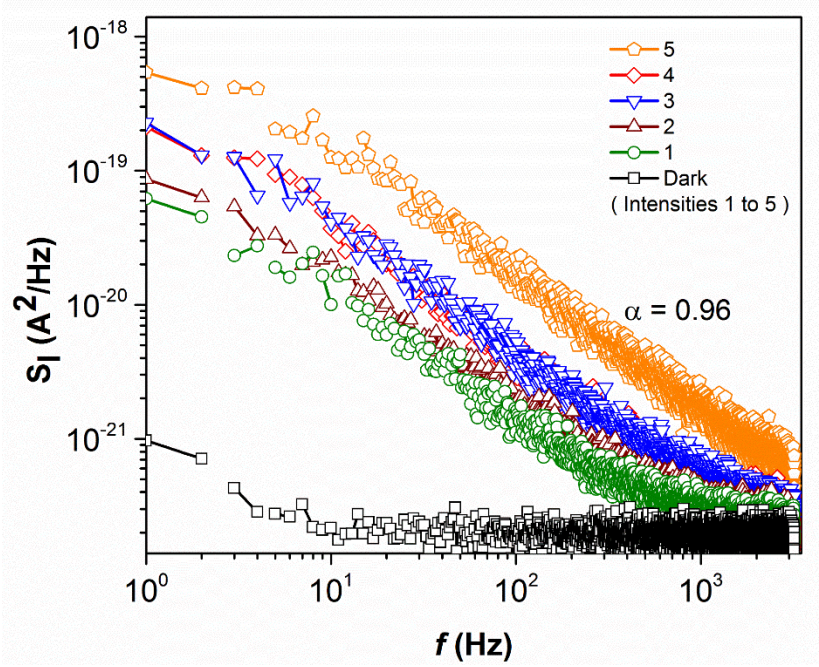

Figure 4.15: *PSD measured from the device, cell degraded down to PCE of <0.1%. 1 to 5 represents intensities (0.45 mW/cm^2, 9.8 mW/cm^2, 18.6 mW/cm^2, 23 mW/cm^2, and 52.4 mW/cm^2).*

This is an important result. There is a change in the noise spectrum from figure 4.13 (η ~15 %) and figure 4.15 (η ~ 0.1 %). In this degraded stage, multiple sources like trap states, mobile defects, interface deterioration contribute to the overall noise. Noise is a valuable tool for the evaluation of defect states[115] in solar cells.

The PSD fits the Hooge's model and the *1/f* exponent α = 1. The observation indicates:

- There is an increase in the density of trap states with degradation, and unlike the initial stages of the device, now traps are not localized but uniformly distributed over the device.

- Mobility fluctuations are also a factor besides the carrier number fluctuations which is contributing to the noise source in HOIP solar cells.

The noise was also measured from the same device (device 3) during the efficiency stages of 7.8%, 4.5%, and 0.0.5% of the device. JV characteristics for different device performance stages (PCE) is shown in the figure 4.16, and corresponding normalized noise spectrum is depicted in the next figure.

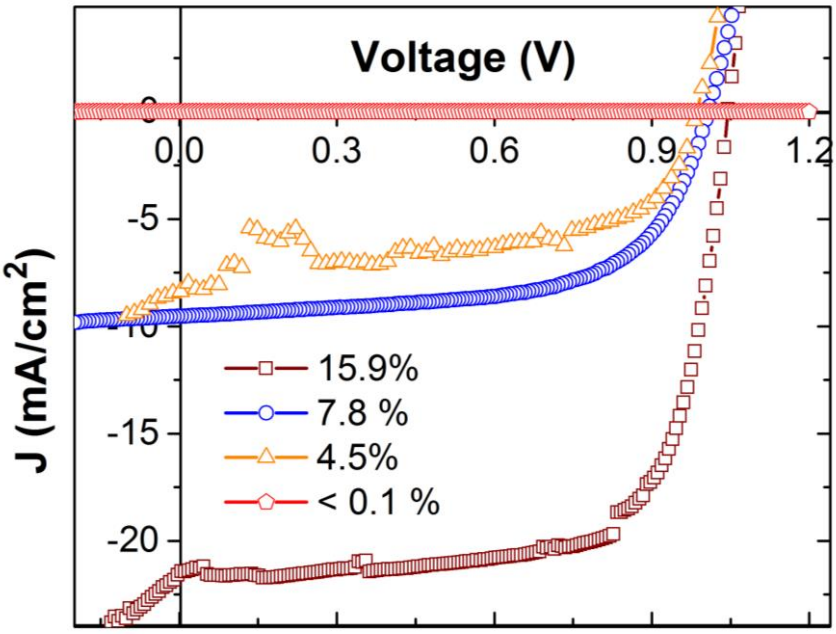

Figure 4.16: *J(V) characteristics at different degradation stages of device 3.*

Figure 4.17 represents the normalized power spectrum density from the device 3 at its different stages of degradation. Noise measurements taken at similar intensities at four different stages of degradation are normalized with their respective J_{sc} values, under 1 Sun illumination. Normalized noise $(S_I(f)/J^2_{sc})$ i.e. $S(f)$ is found to increase in magnitude with degradation. Normalized noise magnitude in the degraded stage (where efficiency < 0.1%) is three orders of magnitude higher than the stage when the device was ~15% efficient. With degradation, the current density decreases and $S(f)$ power spectrum density increases in magnitude over a wider f range, exhibiting an observable change in noise spectral profile.

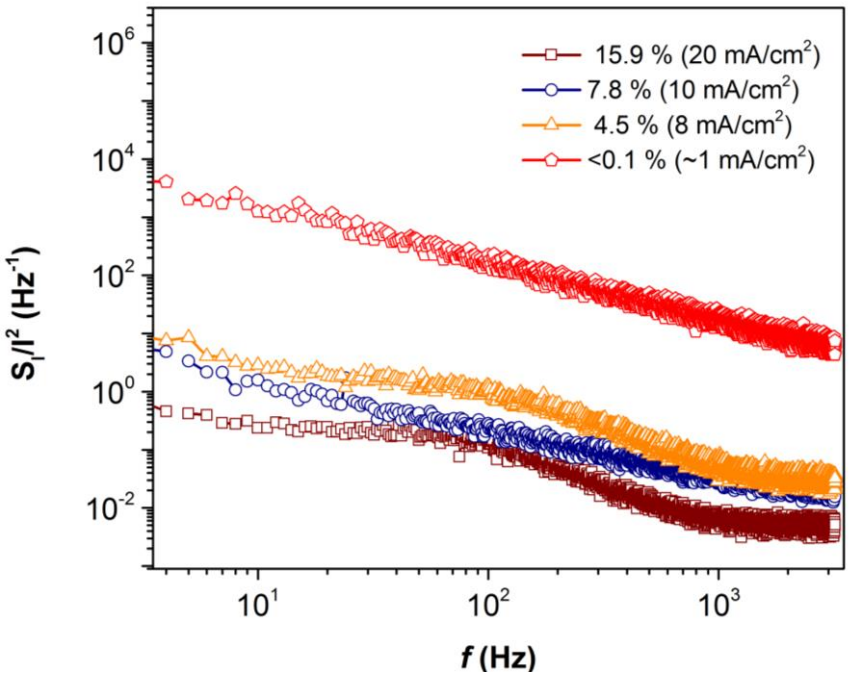

Figure 4.17: *Degradation studies: normalized noise power spectrum density (NPSD), of device 3 with efficiency at 15.9%, 7.8%, 4.5% and <0.1% levels which corresponded to the measurements taken at 0 hr., 8 hrs., 16 hrs. and 32 hrs.*

It may be instructive to compare these changes in these HOIP cells with the noise studies of Stabeler-Wronski defects which arise in a-Si based cells.[147] According to Stabeler-Wronski effect (SWE) metastable changes in the properties of hydrogenated amorphous silicon (a-Si) can be induced due to the light exposure. Light exposure leads to the increase in the defect density of hydrogenated a-Si, which results in an increase in the recombination current and thus suppresses the PCE.

A graph is plotted between the NPSD and the efficiency to observe the nature of noise amplitude increase with degradation (figure 4.18). This plot is limited to four data points. However, the analysis of the noise amplitude with degradation profile can be further improved by statistical analysis of more data points provided stable for a longer duration so as to facilitate the capturing of multiple experimental data sets. The available results indicate the noise amplitude (at 1Hz) is significantly higher for the lower efficiency state and it increases in nearly power law manner with degradation.

In figure 4.19, J(V) characteristics in dark conditions for different stages are shown. This plot reveals that there is no significant change in the dark current profile in the measured HOIP solar cells with degradation. The device continues to show ideal diode behavior.

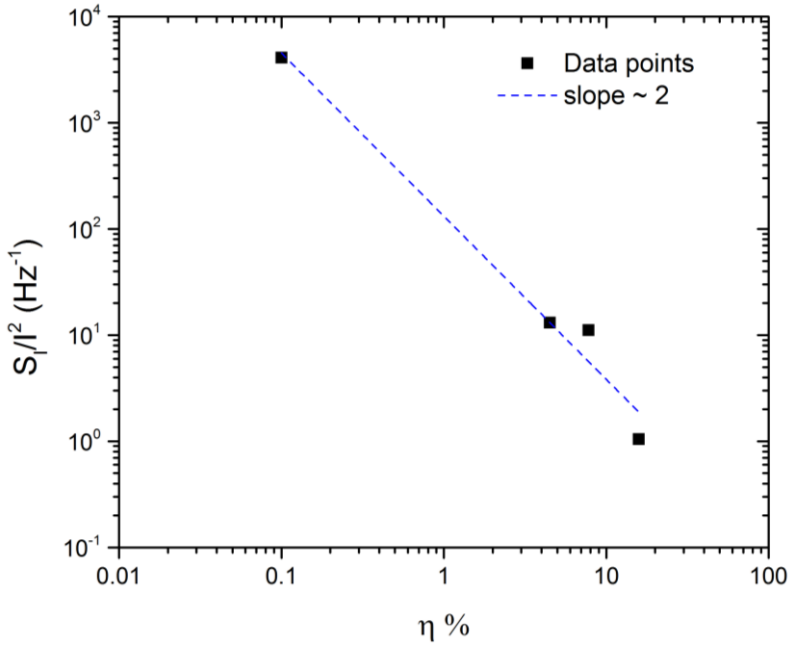

Figure 4.18: *Plot between NPSD and PCE depicting an increase in noise amplitude with degradation.*

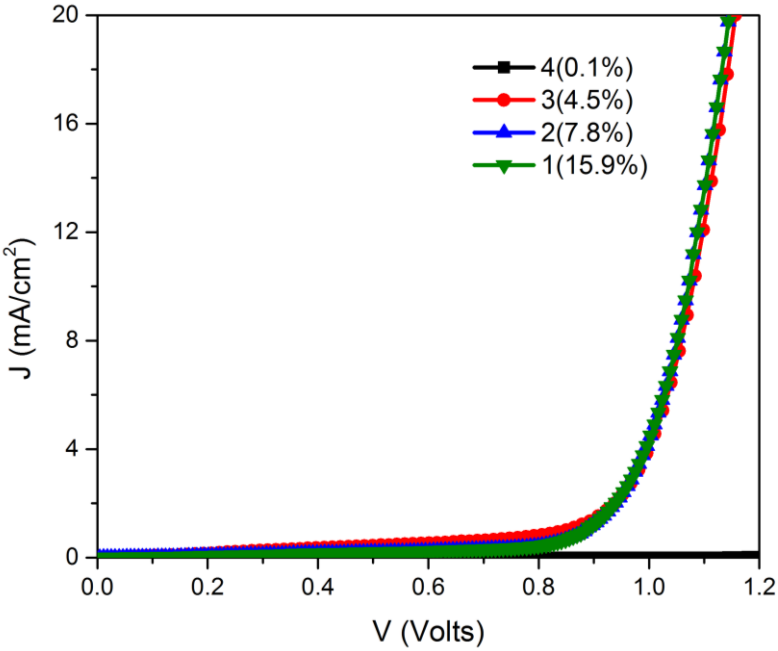

Figure 4.19: *J(V) characteristics in dark condition for different degradation stages.*

It is hypothesized that different structures of perovskite solar cells, depending upon the constituents and the fabrication may give unique associated noise signatures during their high performance/ stable stages. However, after degradation, all types of HOIP solar cells should give consistent *1/f* noise with cross-over in frequency (*1/f* noise over wider frequency

bandwidths). This argument can further be supported by observing the noise evolution trend in device 2 (figure 4.20).

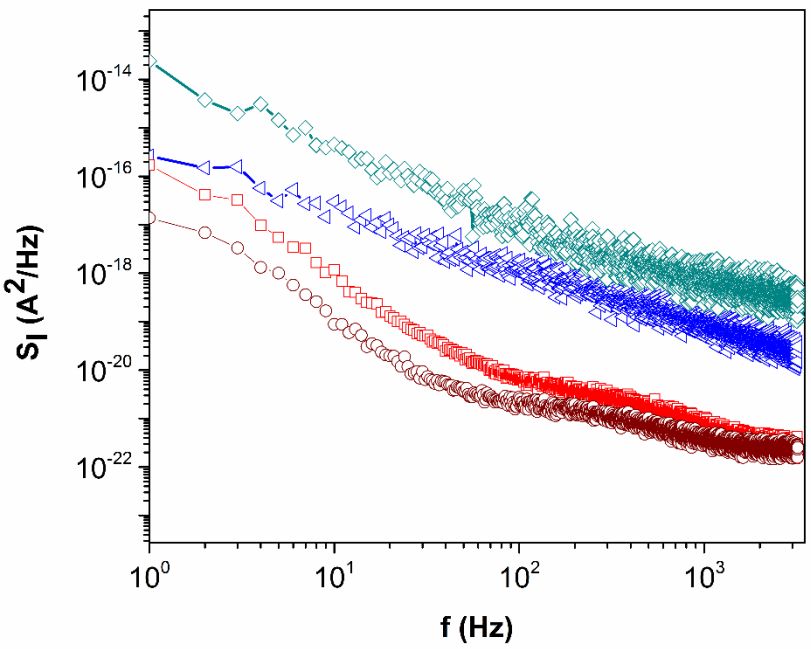

Figure 4.20: *Evolution of noise with degradation as seen in device 2 (conventional structure,* FTO */ TiO_2 / C_{60} / $CH_3NH_3PbI_3$ / Spiro-OMeTAD / Ag).*

The PSD at the degraded stage for both the conventional and the inverted structure gives the consistent *1/f*. This reproducibility of noise pattern can be assumed to be universal and should be applicable for all perovskite solar cells. The evolution of the noise behavior with degradation of the device is informative and can be utilized to predict the trajectory or the useful lifespan of the device.

The summary of the experimental results and analysis, obtained after three different device structures of hybrid organic-inorganic methylammonium lead trihalide perovskite solar cells is given in table 4.1.

Parameters	Device 1	Device 2	Device 3
	FTO / TiO_2 / $CH_3NH_3PbI_3$ / Spiro-OMeTAD / Ag	FTO / C_{60} / $CH_3NH_3PbI_3$ / Spiro-OMeTAD / Ag	FTO /Poly-TPD / $CH_3NH_3PbI_3$ / PCBM / BCP / Ag
V_{oc} (V)	0.91	0.88	1.04
J_{sc} (mA/cm^2)	16.51	2.61	21.85
Fill Factor	48.78	60.67	69.9
Efficiency (η %)	7.32	1.39	15.96
S_I (A^2/Hz) (at 1 Hz) P = 3 mW/cm^2	4.5×10^{-16}	1.1×10^{-17}	1.5×10^{-19}
S_I (A^2/Hz) (η < 0.1 %) (at 1 Hz) P = 3 mW/cm^2	4.4×10^{-15}	1.9×10^{-15}	1.2×10^{-18}
α in $1/f^{\alpha}$	α~ 1.9	α~ 2 for lower f (<100Hz) and α~1 for higher f. At very low η (<0.1%),1/f is uniform with α~ (1to 1.4)	α ~ 1. In addition to 1/f, G-R noise is observed. at η < 0.1%, uniform 1/f behaviour with α~1

Table 4.2: *Summary of the studies on the different devices*

4.7 Outdoor noise measurement

The noise measurement experiments are also performed in real outdoor conditions under the direct Sunlight. For this purpose, the experimental set comprising of portable parts such as DSA, pre-amplifier and a laptop along with standard low noise connecting cables and wires are taken on the rooftop. The device is stored in a vacuum chamber under positive nitrogen pressure in order to avoid the instability of the device during the experiment. Light is exposed to the sample through a glass window present in the vacuum chamber. Experimental results from a typical solar cell of device 1 type (FTO /TiO_2 /Perovskite / Spiro-OMeTAD /Ag) are presented here.

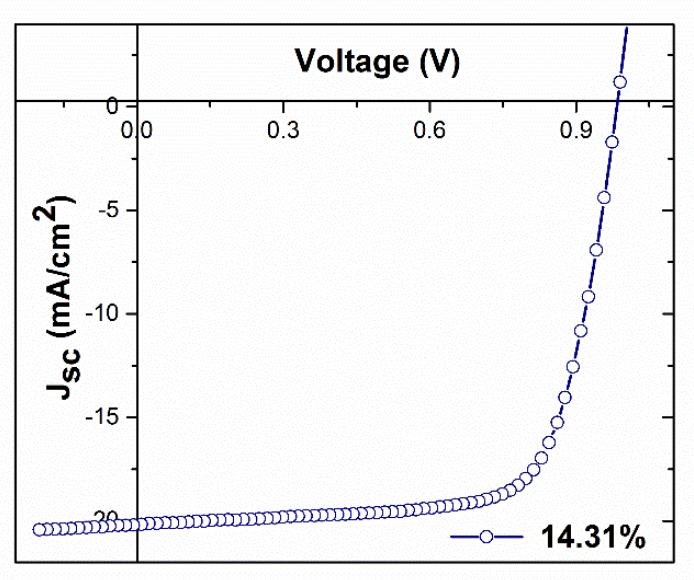

Figure 4.21: *J(V) characteristics of a typical device used for outdoor measurements*

Figure 4.21 shows the J(V) characteristics with PCE of ~ 14 % and figure 4.22 depicts the corresponding noise spectrum. Characteristic noise responses from cells under direct sunlight (outdoor conditions) are similar to the results obtained in these devices under laboratory conditions.

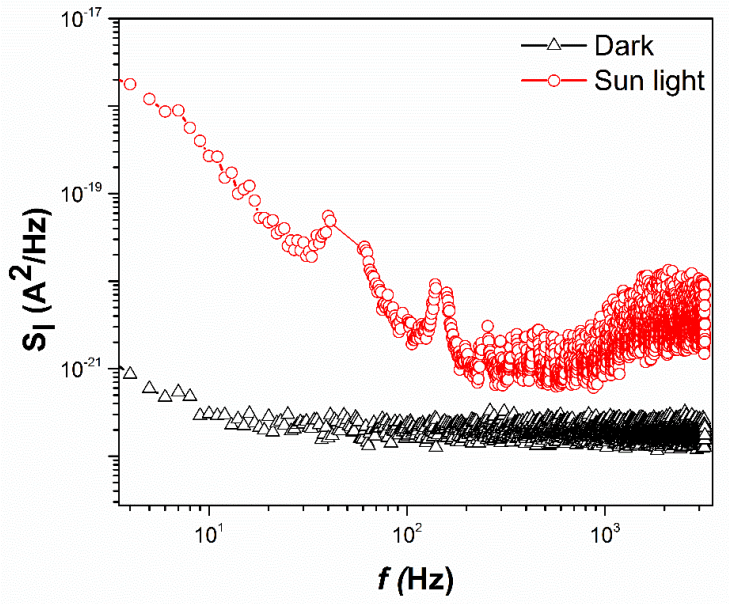

Figure 4.22: *Noise spectrum obtained from the outdoor experiments under dark and direct Sunlight conditions. Distinct 1/f noise is observed in light (which matches with the laboratory experiments)*

4.8 Thermal admittance spectroscopy

In addition to noise spectroscopy, complimentary studies using thermal admittance spectroscopy (TAS) are discussed in this section. TAS is useful in quantitative analysis of the density of trap states. These measurements are carried out on similar inverted structure devices which are used for noise measurements. The experiment is carried out by Dr. Zhipping Wang and Dr. Pabitra K. Nayak in Prof. Henry Snaith's laboratory, University of Oxford (U.K.).

Introduction to thermal admittance spectroscopy (TAS)

Thermal admittance spectroscopy (TAS) is a technique that uses electrical characterization to measure the capacitance and conductance as a function of frequency and temperature. Contrary to the deep level transient spectroscopy (DLTS), which is a nonequilibrium measurement technique, TAS is a steady state measurement. DLTS is used for high doped semiconductors, whereas TAS can be used for low doped or high resistivity materials.

The basic idea behind the TAS is to measure the capacitance or conductance over a range of temperature and frequencies. At a given high signal frequency if the emission rate is slower than the test frequency, a deep trap is unable to respond and contribute to the capacitance and conductance. However, with increase in the temperature the emission rate of a defect increases and trap can contribute to the measurement.

The deep level signal appears as a step in the capacitance, or a peak in the conductance at a threshold in frequency or temperature. Inflection point temperature of each plot of capacitance versus temperature at a fixed frequency is used along with the frequency, as one point in an Arrhenius plot. The energy associated with the defects can be obtained from plotting pairs of frequency and temperature points in an Arrhenius plot of emission rate (frequency of measurement) versus 1/kT.

A typical experimental set up for TAS measurement consists of a specially designed chamber to hold the sample, a cooling unit, temperature controller system and LCR meter so as to measure the capacitance (Appendix E). The admittance consists of two parts conductance and susceptance.

Admittance is given by $Y(f) = G(f) + iS(f)$

Susceptance is related to the capacitance: $S(f) = 2\pi f C(f)$.

Mott-Schottky plots:

Measured capacitance at 10kHz vs. Bias voltage at 294 K.

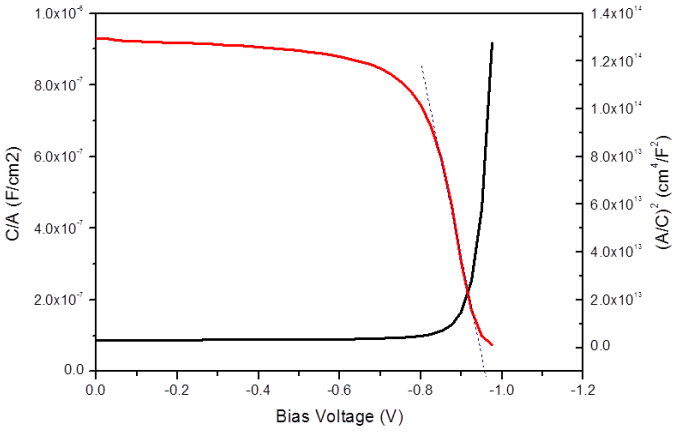

***Figure 4.23**: Mott-Schottky plot for perovskite solar cells. The blue line is an extrapolation to determine the built-in voltage.*

To determine the trap density of states (tDOS) by thermal admittance spectroscopy (TAS), we followed the procedures reported in Refs. [148]and [149]. First to determine the depletion width and built-in voltage, Mott-Schottky plots were measured: the capacitance (C) at a frequency (f) of 10 kHz were measured as a function of bias voltage (V_{bias}) at a temperature (T) of 294 K. A typical Mott-Schottky plot of one of the devices reported here is shown in Figure 4.23 in red, where A is the area of the measured cell (0.0919 cm^2 in our case).

From extrapolating the $(A/C)^2$ graph as shown in figure 4.23 to A/C = 0 follows the built-in voltage. The slope of the extrapolation can be used to determine the doping density N_d (e.g. due to traps) and the depletion width W at V_{bias} = 0 V:

$$N_d = -\frac{2}{q\varepsilon}\left(\frac{d(C/A)^{-2}}{dV}\right)^{-1}, \tag{4.4}$$

$$w = \sqrt{\frac{2\varepsilon(V_{bi}-V_{bias})}{qN_d}}, \tag{4.5}$$

where ε is the dielectric constant and ε_r for this perovskite is 30.[149]

	V_{bi} (V)	N_d (cm^{-3})	W (cm)
Fresh	0.95	$5.6x10^{15}$	$7.5x10^{-5}$
Aged	0.87	$8.6x10^{16}$	$1.8x10^{-5}$

Table 4.3: *Calculated parameters from Mott-Schottky plot.*

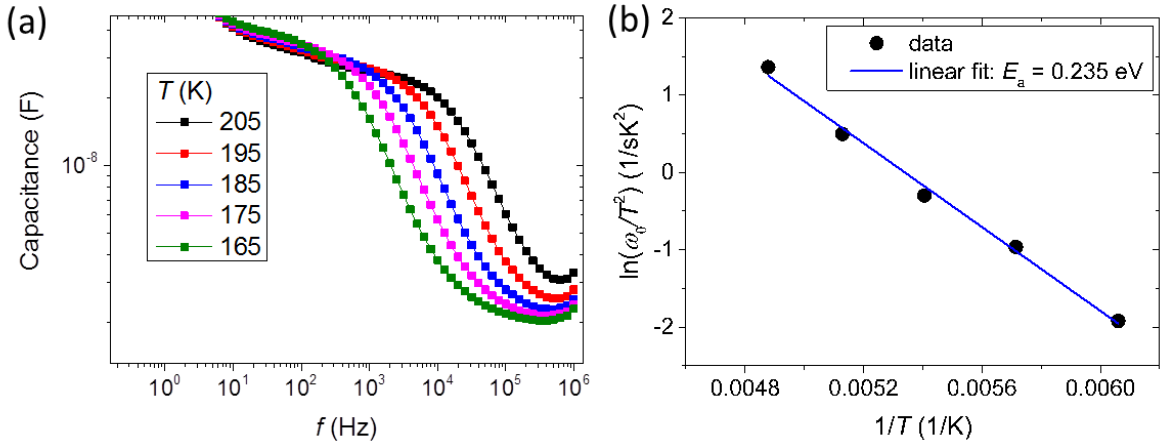

Figure 4.24: *a) Typical temperature dependence of the frequency-dependent capacitance of a perovskite solar cell. b) Arrhenius plot of the characteristic transition frequencies extracted from a) to extract the defect activation energy of a perovskite solar cell.*

After characterization of the Mott-Schottky plots, the temperature dependence of the frequency dependent capacitance is measured. An example is shown in figure 4.24 (a). Steps are observed in these spectra that shift to lower frequency for lower temperature. The transition frequency can be related to the rate of carrier emission and capture from traps in the bandgap. We assume that the occupancy of these states is in thermal equilibrium and hence is determined by the Fermi-Dirac distribution. Therefore, the trap energy E_a and the characteristic transition frequency ω_0 can be expressed as:

$$\omega_0 = 2DT^2 exp\left(-\frac{E_a}{kT}\right), \qquad (4.6)$$

where D is a constant related to the effective density of states in the conduction band, the thermal velocity, and the carrier capture cross-section.[28,150,151]

From figure 4.24 (a) we extracted a dC/df plot which can be used to determine the characteristic transition frequency that relates to the temperature-dependent shift of the steps observed in the high-frequency regions in figure 4.24 (a). This characteristic transition frequency is plotted in

Figure 4.24 (b) as a function of temperature. From Figure 4.24 (b), the activation energy of the trap states is determined by fitting with Eq. 4.6.

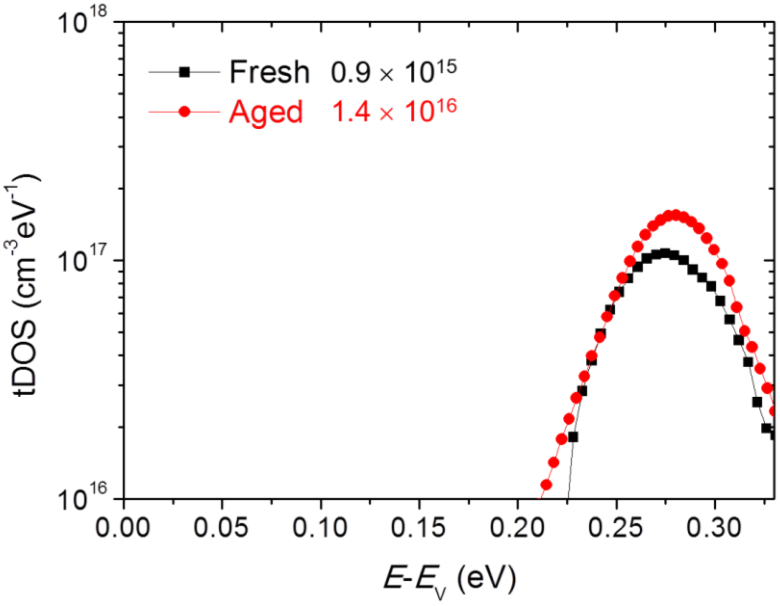

***Figure 4.25**: tDOS for perovskite solar cells before and after aging.*

Now the frequency dependent capacitance can be used to determine the energetic profile of the tDOS by using:

$$N_t = \frac{V_{bi}}{qW}\frac{dC}{d\omega}\frac{\omega}{kT}. \qquad (4.7)$$

The horizontal axis can be converted from frequency to energy by Eq. 4.6. The resultant graph shows the tDOS as a function of energy related to the valence band of the perovskite. These graphs have been extracted from multiple devices and are shown in figure 4.25. Integration of the tDOS along the horizontal axis gives the trap density in the perovskite.

These studies further highlight the results from the noise studies, i.e. there is an increase in the trap density with degradation HOIP solar cells.

4.9 Summary

The general characteristics of specific noise pattern associated with a structure of the perovskite solar cells were reproducible across a set of 48 solar cells. A qualitative trend of the noise levels magnitude associated with different geometry is apparent, with the presence of significant noise in conventional (Device type1) structures and relatively low-noise in the inverted structure

device. In all the devices, fluctuations proportional to the light intensity *(P*) is observed with an *S(f)* exhibiting a P^{β} behavior.

The salient features which emerge are the following: (i) Noise magnitude relative to the signal directly correlates with the performance parameters, with the noise levels increasing with degradation. (ii) All the devices exhibit $1/f^{\alpha}$ behavior in the range < 1 kHz (iii) The exponent α and *f* range over which *1/f* response is observed appears to depend on the transport processes and the associated disorder in the system (iv) the noise mechanism of devices under operation with high *J* (at high light intensity) is different from that at low *J*.

This intensity dependent noise response appears to be dependent on the device structure and is different from the different geometry. For instance, device 2 indicates significant $1/f^{\alpha}$ component at large *J* as compared to PSD obtained for device 3 in the same f-range. It is expected that as the device engineering advances are made of these materials in terms of ionic impurities and defects, optimum trap energetics and densities and improvement in barrier layers are made, the fluctuations decrease and exhibit stationary white noise behavior. Noise spectrum tends to change with degradation, and importantly rate of degradation can be monitored, and future stability can be predicted.

The utility of noise measurements in evaluating the defect states is HOIP solar cells is also highlighted. The findings are complimented by the TAS measurements, and different noise signatures (including the appearance of g-r noise) can be picked in accordance with the device structure and the stability of the device.

Chapter 5

Photocurrent scanning and local noise measurements

Probing of the degradation and stability in solar cells in general is done by using transient measurements by evaluating mobility and recombination in the device at its different stages of degradation. Significant information about the trap density and mechanism of charge extraction can be obtained by using the transient measurements and its drift-diffusion simulations analysis.[152] Moreover, various frequency dependent approaches such as intensity modulated photocurrent, and photovoltage spectroscopy has been utilized to study charge transport mechanisms.[153] An averaged parameter from the entire area of the sample is used for the analysis using these techniques. However, information about the local recombination centers and local stability from a specific section of a device cannot be obtained with these traditional techniques. During degradation, loss mechanisms and recombination can get significantly altered in different regions of the device depending on the device geometry and degradation sources.

In this chapter, a unique and original approach to study the inhomogeneity in the HOIP solar cells is demonstrated. In the subsequent sections, results obtained from the study of different perovskite solar cells with the inverted structure using photocurrent scanning are presented. Information from the scanning is then exploited to measure noise locally within a device at different regions.

5.1 Introduction to photocurrent scanning

The basic principle behind the photocurrent scanning is that a small region within a device (< 10 μm) is illuminated at a time and the photocurrent response from these small regions is recorded by gradually scanning the entire device area. This provides the photocurrent response profile from different sections within a device and information obtained can be used to

segregate areas with high or low photocurrent performances. Thus, unlike obtaining stability status from the entire solar cell device, degraded patches within the device can be spotted, and elaborate insights about the device stability are obtained.

The experimental setup used for the photocurrent scanning (PCS) is designed and developed in the Molecular Electronics Lab by Dr. Suman Banerjee and co-workers. The details about the scanning can be found in the manuscript *"Photocurrent imaging of large area solar cells and modules at micron resolution."* The setup comprises of three major components: (i) an optical source (ii) sample stage controller (iii) and a measurement unit. The schematic diagram for the PCE is depicted in figure 5.1.

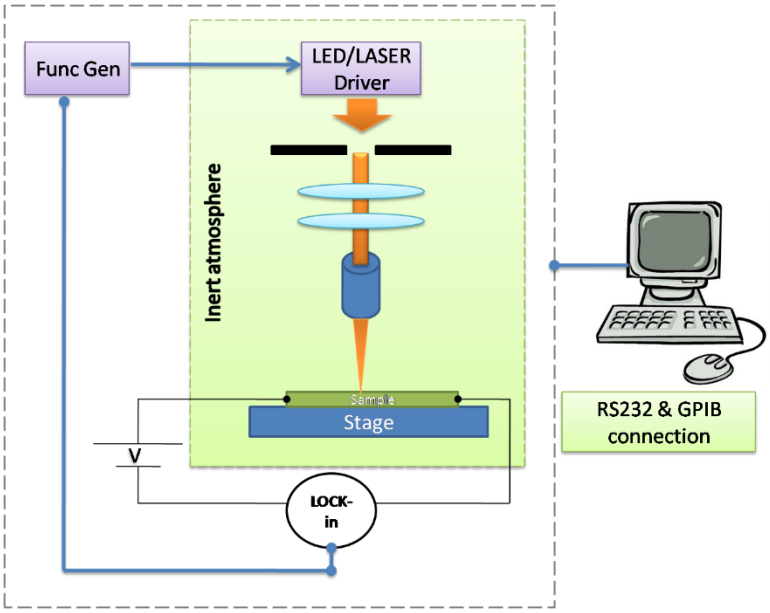

Figure 5.1: *Schematic representation of Photocurrent scanning setup (courtesy Dr. Suman Banerjee)*

A 632 nm LASER controlled by a function generator is used as a light source in the setup. The required current to drive the LASER is beyond the capacity of the function generator. Hence, a separate LASER driving circuit is designed for driving the LASER. The input of the driver circuit and a lock-in reference is fed directly by the function generator, so as to modulate laser intensity. The objective lens (20X and 50X) are used to get a focused LASER spot-size, at the plane of the sample. The measurement of spot size used during the scanning of HOIP solar cells with the 20X objective is described in the "Appendix C." A sub ten-micron spot size is easily obtained.

"Thorlab XYZ motion controller" with 5 µm resolution is used to control the movement of the sample. Along with the PCS, transmitted image of the perovskite solar cell under test is obtained by using a Si photodetector (T-PD) by placing it below the focused light. Lock-in amplifier *(Stanford Research SR830 lock-in)* is used to measure the sample photocurrent data and T-PD data.

The DUT is placed on a sample holder, whose motion is controlled by the Thorlab XYZ motion controller. The sample holders specific to the HOIP solar cells are made in the lab using a 3D printer. The entire setup is housed inside a "mini-glove box," so that the device can be kept in an inert or nitrogen environment. This is done to avoid the variation in the device stability during the measurement. Processing of the data is done by using different software tools. The data acquisition and plotting is done by using *"Labview"*[154], and image analysis is performed through a customized image analysis software developed using "*Mathematica from Wolfram Research"*.[155]

5.2 Mapping photocurrent response in HOIP solar cells

Experimental results from the photocurrent scanning of perovskite solar cells are presented in this section. Multiple devices with structure FTO/ Poly-TPD/ $CH_3NH_3PbI_3$ / PCBM / BCP / Au, are studied using the protocol described in section 5.1. Figure 5.2 shows the external quantum efficiency from a typical cell used in the measurement during its high-performance stage. Its value is found to be 93.3 % at the center, the details of calculations can be found in Appendix D.

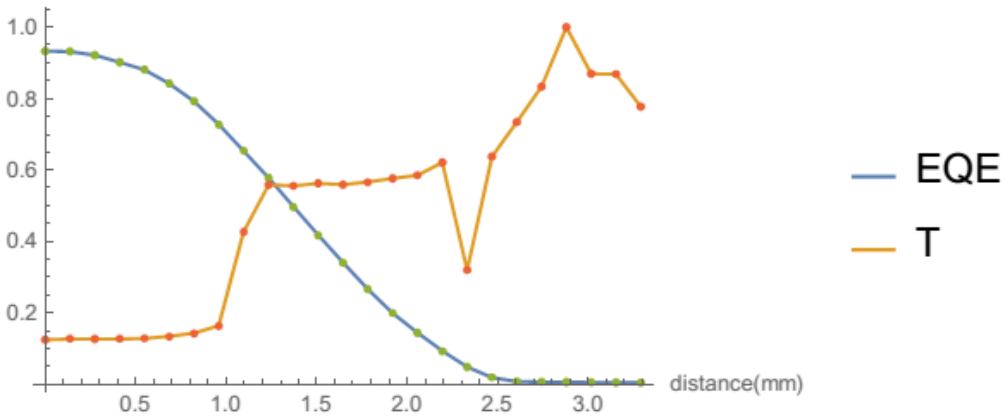

Figure 5.2: *External quantum efficiency as a function of distance. (T is the transmittance plot)*

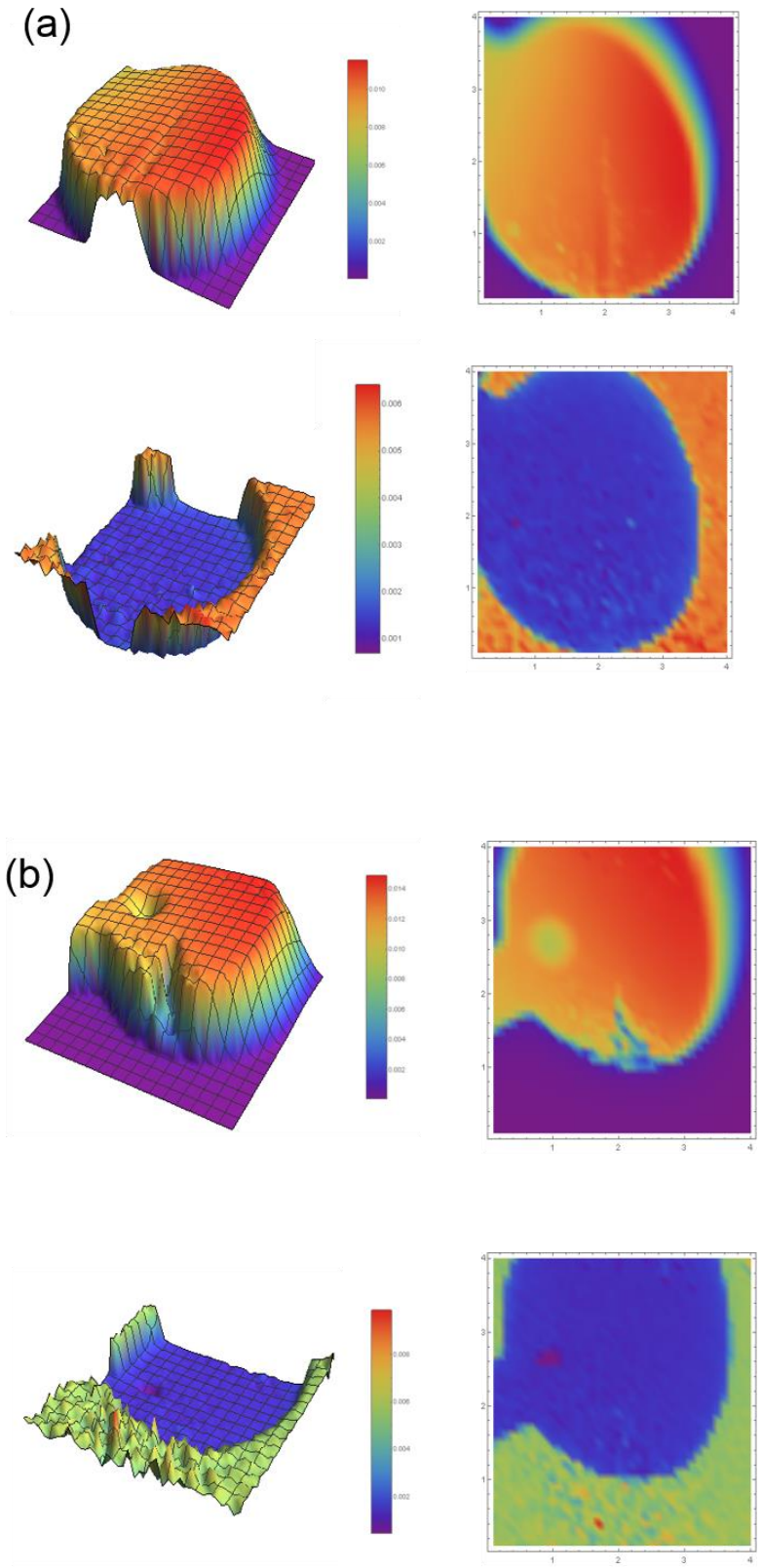

Figure 5.3: *Photocurrent scanning and transmittance images in 2D and 3D (a) from a device with less inhomogeneity (b) mechanical defect on the contact, gets reflected in PCS and transmitted images.*

Figure 5.3 depicts the typical PCS profile from two different devices. The first row of figure 5.3 (a) shows the PCS in followed by second row, representing transmittance data from the device in 3D and 2D respectively. The Photocurrent response obtained for this device is uniform i.e. most of the sub-sections within the device are having a similar performance against the illumination, and on the whole, irregularities in the sample are less. However, exact PCS response from different regions can be analyzed using the color contrast. Similarly, PCS and transmittance images in 3D and 2D are depicted in figure 5.3 (b). In this case, mechanical defect in the top electrode can be observed clearly in the PCS and transmitted images. Moreover, the onset of degradation from one of the edges can also be observed.

Transmittance images are especially useful in a way that it gives the exact idea about the area of the device under the scan. It leads to the better analysis of the PCS data. Another important feature that can be observed from these images are that there is a gradient in photocurrent response towards the edges. There is a gradual decrease in the photocurrent as we move towards the periphery of the device. This can be further seen from the figure 5.4.

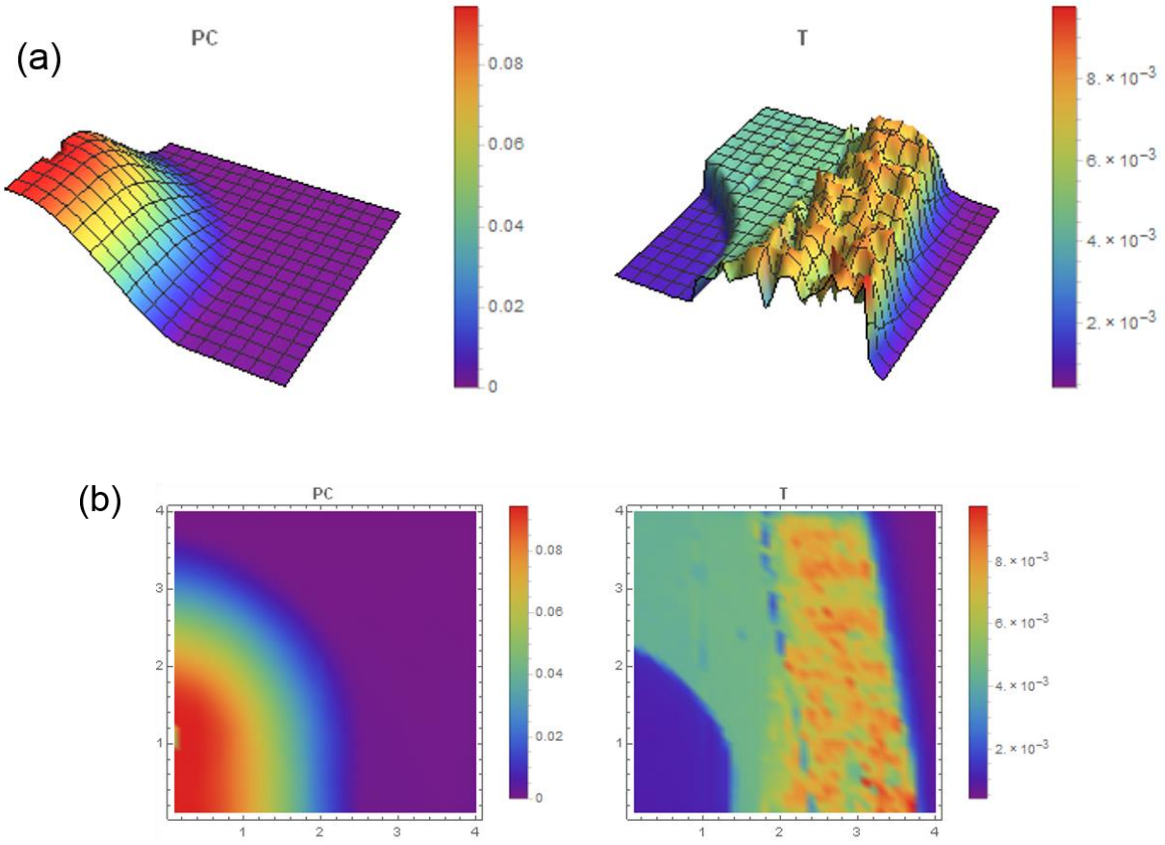

Figure 5.4: *PCS performed at the edge of a device PCS and transmittance images (a) in 3D and (b) 2D. Degradation is initiating due to the ingress of moisture and oxygen from the periphery.*

The scanning is performed at the edge of the device instead of scanning the entire device area. However scanning area is kept as previously ($4\times 4\ mm$), so the actual area under scan now also covers area outside the device, this enables clear photocurrent response specifically from the edges in the scanning images. The probable explanation for the observed gradient at the periphery is due to the ingress of the oxygen and moistures through the periphery and indicates the offset of degradation.

Scanning of different devices at different degradation levels

With a motivation to study the pattern of degradation profile in different perovskite solar cells PCS is performed in multiple devices and various stages of degradation. When the device is still stable (low degradation state) the photocurrent profile is similar to that in figure 5.3 (a). However, with degradation device may show different scanning response depending upon the level of degradation.

In figure 5.5 the scanning results from the seven different devices, fabricated on the same substrate are depicted. This set of scanning measurements is performed at the stage when all the devices are substantially degraded. However, it can be seen that the level and pattern of degradation in each device is different from each other. Column 1 and 2 in figure 5.5 represents PC response in 3D and 2D respectively. Column 4 represents the transmittance response whereas additional phase scanning measurement is also carried out along with PC and transmittance scanning. This is depicted in column 3. The combination of PC, transmittance and phase scanning provide a very detailed information about the state of the device and significantly add to the quality of stability and degradation analyses of perovskite solar cells.

The seven rows in figure 5.5 represent seven different devices from D1 to D7. Device D5 and D7 are relatively better performing than the rest. On the other hand, Device D1, D2, and D4 are degraded with some patches of device areas still showing some photocurrent response. Device D3 is severely degraded device D7 is completely degraded as no or negligible value of photocurrent is recorded. Even though the PCS images change drastically with degradation, however, there is no change in transmittance images, confirming that the entire device area was scanned and the low photocurrent response is due to the degradation of the device. So the utility of photocurrent scanning can be appreciated from these measurements as they reveal finer details about the solar cell device.

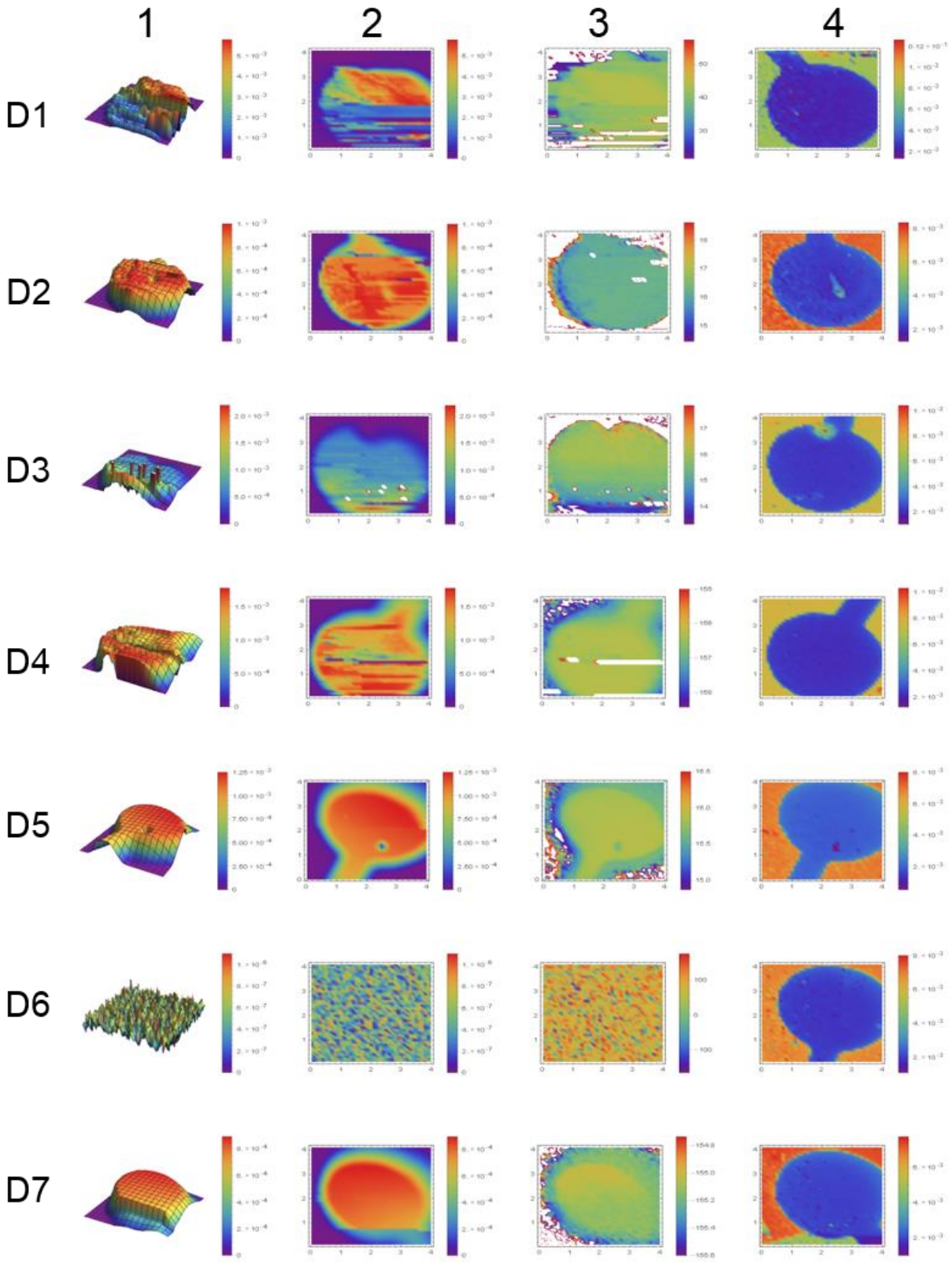

Figure 5.5: *Scanning images from seven different devices. In addition to PCS and transmittance images (column 2 and 4 respectively) phase scanning images are also depicted in column 3.*

5.3 PCS and local noise measurements

Noise measurements in previous chapters were carried out by exposing the entire area of the device, and cumulative effects resulted in the obtained noise spectrum. However, as shown in this section noise measurements can further be extended to measure noise locally from a small section of the device. PCS gives the information about the hot and cold spots (high and low performing regions), and it is possible to extract noise signals from these small regions.

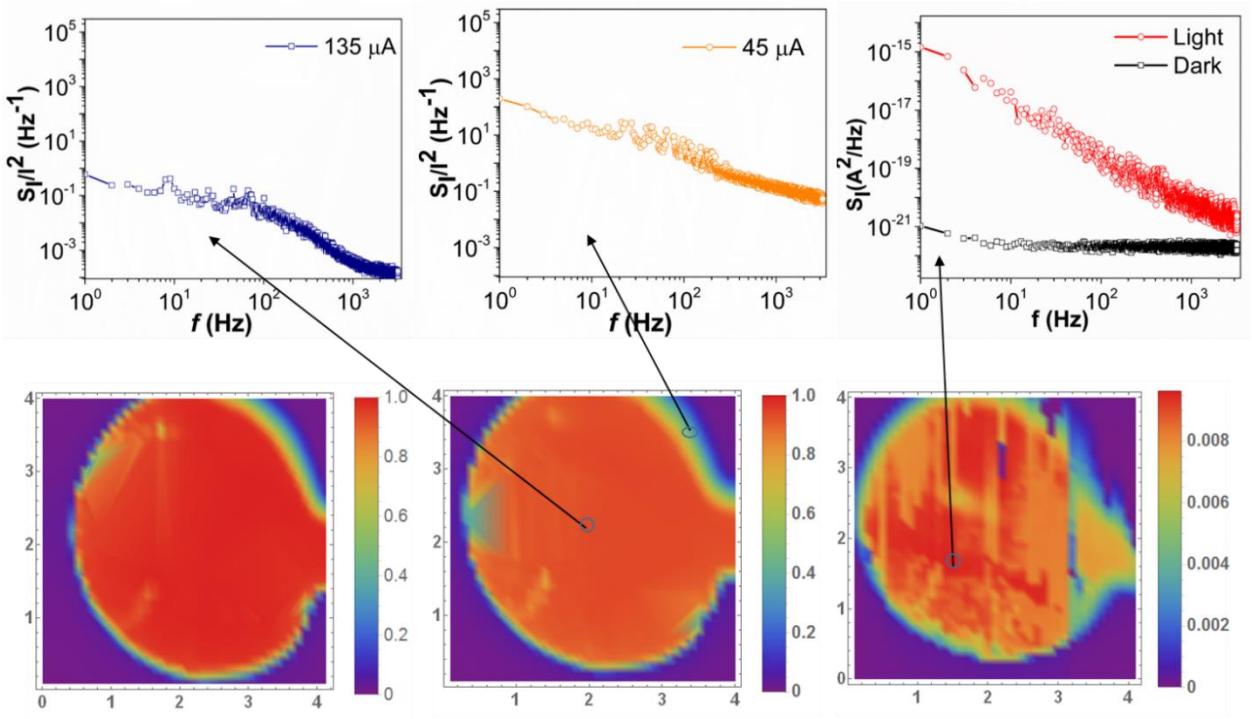

Figure 5.6: *2D photocurrent scanning for 4 mm X 4 mm area with a beam size of ≈10 µm and intensity ≈ 1 mW/cm^2.The regions of different photocurrent levels (scales) are depicted with a color contrast. Figure (a), (b) and (c) shows device degradation over a duration of two days. 1 and 2 in (b) represent periphery and bulk regions. Local Noise Measurement: Normalized power spectrum density from two different regions as indicated, region 1 and 2 correspond to the I_{ph} of 45 µA and 135 µA respectively. The inset shows local noise measurement in a degraded region along with the dark background.*

Figure 5.6 shows photocurrent scanning data from a typical inverted structure device FTO/Poly-TPD/$CH_3NH_3PbI_3$/PCBM/BCP/Au. Scanning carried out at three different stages (figure 5.6 (a to c)), depicts the progression in the degradation of the device. It should be noted that photocurrent, I_p (as indicated by the lower scale) is more than an order of magnitude lower

for figure 5.6 (c). These measurements reveal regions with inhomogeneities which is reflected in the device performance. Additional local noise measurements were carried out to study the noise response from the local regions. In this case, the light is focussed to a region with beam size ≈ 100 µm. Noise features were detectable from these spots. The signal analysis revealed *1/f* signatures from these regions. The combination of scanning and local noise measurements should be of wide utility and examine the stability of the device.

Analysis of photocurrent profiles as shown in figure 5.6 is compared with the local noise measurements. The power spectrum density reveals high noise amplitude for regions with low I_{ph}. The factors involved in the I_{ph} variation in these cells are also responsible for the noise fluctuations. A local noise measurement carried out in a degraded device exhibiting low I_{ph} from a region indicated in figure 5.6 (c) reveals large noise levels with a distinct *1/f* behavior over a significantly large range spanning over 2 Hz to 50 kHz (figure 5.7).

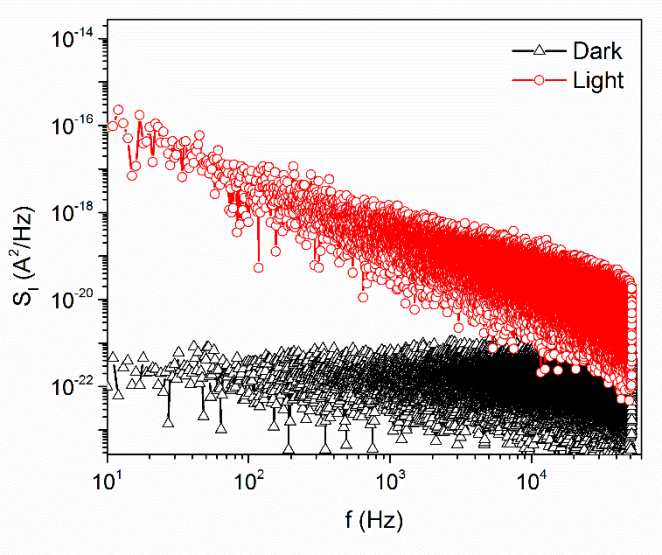

Figure 5.7: *1/f noise over a wide range of frequency (52.4 kHz) from a point within a degraded device.*

The consistent *1/f* noise observed over a wide frequency range in the case of the degraded device by local illumination is in agreement with the noise spectrum observed earlier in the case of usual noise measurement by wide illumination, covering the entire device.

5.4 Implication of photocurrent scanning and local noise measurements

The association of noise with device performance can be explored by examining noise features obtained from local regions with different degree of degradation within each solar cell. Devices decaying over a finite duration can be periodically scanned and provides a testbed for this spatial dependence of noise. These scanning measurements were carried out with local illumination with a narrow beam spot size (< 10 μm). This gives the mapping of entire device area and regions with high or low photocurrent region which can be visualized. These measurements show features of typical solution processed devices, with a low photocurrent response at the periphery. Inhomogeneity emanating from other regions can also be tracked with these spatial photocurrent maps.

The degradation of solar cells can be very well probed using the PCS as it accurately reveals the performance level of different areas in the device. This will have huge implication in large area solar cells where defective regions (regions with low I_p) can be sorted. The combination of PCS and local noise provide a valuable tool to gather insights into the transport mechanisms and monitoring of the device stability.

Apart from the above-stated applications, the PCS set up can be used to understand inhomogeneity in the device arising due to the different fabrication methods used. The mapping of the device also enables the prediction of the device efficiency and losses. It is possible to integrate different wavelength light sources with the PCS setup, resulting in the possibility of probing different optical phenomena. Considering then low-cost optics involved in the setup, instruments can be modified for real time transmittance and reflectance imaging, intensity control, and light bias usage.

The noise and PCS set up can also be used for the design of module of solar cells as the wavelength of excitation, light spot and scan area can be easily configured by the user. Further PSC set up along with non-destructive noise technique can be used to perform quick quality check of the modules in the production lines and stability can be measured against the different degradation stage, operating and atmospheric conditions.

Chapter 6

Conclusions and future directions

In this thesis, noise is extensively studied in hybrid organic-inorganic perovskite solar cells. A large number of devices with three different structures including both conventional and inverted have been thoroughly studied to come up with the conclusive trend of noise in perovskite solar cells in general. During their high-performance state, an HOIP device of a particular structure found to have a unique noise feature. This is also evident from the analysis of the time series results. The level of current fluctuations under similar illumination conditions is also different for a different structure of the device. However, with degradation all HOIP devices, irrespective of the device structure show consistent *1/f* noise over a wide range of frequency. In addition to *1/f* noise, generation–recombination noise is observed in the case of high-performance perovskite solar cells with an inverted structure. The origin of g-r noise can be explained by the single trap model, during low bulk trap density effects from localized trap may dominate.

Noise measurements in the ionic systems including DSSCs suggest that it is possible to have signatures of noise originating from the ionic sources. The nature of noise in ionic systems is mostly white (frequency independent noise). Noise from the ionic solutions of PbI_2 and perovskite solutions are found to be relatively less than that of the perovskite solar cells. Noise and DC characteristic (*I(t)*) from 'bias history dependent measurements' indicate the role of ionic movement in the intrinsic transport mechanism in perovskite solar cells.

Noise is demonstrated to be a very useful tool not only in the evaluation of defect states in HOIP solar cell devices but they can provide significant insights into the degradation processes in perovskite solar cells or any solar cells in general. Perovskite-based solar cells exhibit characteristic noise features. The magnitude of the fluctuations and the associated PSD response directly correlates to the state of the device. Devices with inverted structure were found to be more stable and exhibit lower magnitude of fluctuations. The process of degradation of inverted devices is fundamentally different and exhibits lower noise magnitude

as the device decays in comparison to regular geometry devices where noise amplitude grows in a power law manner with degradation. The dependence on the intensity and the cutoff for the *1/f* behavior is also observed to be clearly different for the inverted structure. In the case of sufficiently aged and degraded devices, the noise spectrum uniformly exhibits a characteristic *1/f* response.

Complimentary studies, which involved the qualitative analysis of trap density by thermal admittance spectroscopy corroborates the findings of the noise that density of trap states increases with the degradation. It was possible to measure noise signals in outdoor conditions. $I_{ph}(t)$ snapshot recordings upon analysis exhibited *1/f* characteristics. Measurements of this kind can evaluate the defect growth kinetics in-situ conditions and track the device trajectory.

Besides the noise studies on devices, information from local illumination photocurrent scanning imaging studies is also carried out to highlight the spatial inhomogeneity existing in typical devices. Noise studies are selectively carried out in these disparate regions which exhibit different performance levels. A gradient in the photocurrent response is observed across the device boundary, suggesting that the photocurrent gradually decreases as we approach periphery of the device, suggesting possible ingress of moisture and oxygen originates from the peripheral regions. Implementation of this method in a large type of cells at different stages of performance levels should resolve many of the issues and can highlight the dominant factor in the degradation process.

The spatial inhomogeneity in a device is highlighted by the differences in the noise spectrum. The device aging studies along with a suitable model can assess the defect density and energetics and can be utilized to gauge the feasibility of hybrid perovskite-based cells.

For future directions, it would be interesting to study the noise patterns and signature of degradation prior to drop in photocurrent value of the device. Noise is a very useful non-destructive tool to study the onset of degradation in perovskite. However, its application can be extended to study different aspects of the device. The combination of Photocurrent scanning and local noise measurements can be very handy in monitoring the stability of solar cells. It could be further used to study other solar cells structures and systems like Nanowire FETs (which potentially have application in functional quantum computing system). These studies can provide valuable information about the following- (i) determination of noise amplitude (ii) characterization of degradation mechanisms and phenomena (iii) prediction of structure stability and reliability.

References and bibliography

1 Factbook, C. The world factbook. *See also: https://www. cia. gov/library/publications/the-world-factbook* (2010).
2 Factbook, C. Central Intelligence Agency. *Benin, URL: https://www. cia. gov/library/publications/the-world-factbook/geos/bn. html* (2012).
3 Factbook, C. (2006).
4 Arto, I., Capellán-Pérez, I., Lago, R., Bueno, G. & Bermejo, R. The energy requirements of a developed world. *Energy for Sustainable Development* **33**, 1-13 (2016).
5 Shockley, W. & Queisser, H. J. Detailed balance limit of efficiency of p-n junction solar cells. *Journal of applied physics* **32**, 510-519 (1961).
6 Green, M. A., Ho-Baillie, A. & Snaith, H. J. The emergence of perovskite solar cells. *Nature Photonics* **8**, 506-514 (2014).
7 Precursors, H. H. P. S. C. (Keyou).
8 Shachar, A. Picking winners: Olympic citizenship and the global race for talent. (2011).
9 Al Qassem, A. A COMPARATIVE ANALYSIS OF SILICON AND CADMIUM TELLURIDE BASED SOLAR CELLS. (2016).
10 Roy, K. in *Materials science and physics of non-conventional energy sources* (1991).
11 Zhao, J., Wang, A., Green, M. A. & Ferrazza, F. 19.8% efficient "honeycomb" textured multicrystalline and 24.4% monocrystalline silicon solar cells. *Applied Physics Letters* **73**, 1991-1993 (1998).
12 Rath, J. Micro-/poly-crystalline silicon materials for thin film photovoltaic devices: Deposition processes and growth mechanisms. *Photovoltaic and Photoactive Materials—Properties, Technology and Applications*, 157-170 (2002).
13 Carlson, D. Multijunction amorphous silicon solar cells. *Philosophical Magazine B* **63**, 305-313 (1991).
14 Carlson, D. E. & Wronski, C. R. Amorphous silicon solar cell. *Applied Physics Letters* **28**, 671-673 (1976).
15 Chen, Y. *et al.* Improved performance of flexible amorphous silicon solar cells with silver nanowires. *Journal of Applied Physics* **112**, 124320 (2012).
16 Nubile, P., Torres, P., Hof, C. & Fischer, D. Analysis of the inner collection efficiency in hybrid silicon solar cells. *Solid-State Electronics* **41**, 1202-1206 (1997).
17 Rios-Flores, A., Arés, O., Camacho, J. M., Rejon, V. & Peña, J. Procedure to obtain higher than 14% efficient thin film CdS/CdTe solar cells activated with HCF 2 Cl gas. *Solar Energy* **86**, 780-785 (2012).
18 Aramoto, T. *et al.* 16.0% efficient thin-film CdS/CdTe solar cells. *Japanese Journal of Applied Physics* **36**, 6304 (1997).
19 Chu, T. *et al.* 13.4% efficient thin-film CdS/CdTe solar cells. *Journal of applied physics* **70**, 7608-7612 (1991).
20 Cell, I.-O. H. S. (Shenqiang).
21 Wright, M. & Uddin, A. Organic—inorganic hybrid solar cells: A comparative review. *Solar energy materials and solar cells* **107**, 87-111 (2012).
22 Somani, P. R., Somani, S. P., Umeno, M. & Sato, A. Concept and demonstration of all organic Gratzel solar cell (dye sensitized solar cell). *Applied physics letters* **89**, 083501 (2006).

23 Neugebauer, H., Brabec, C., Hummelen, J. & Sariciftci, N. Stability and photodegradation mechanisms of conjugated polymer/fullerene plastic solar cells. *Solar Energy Materials and Solar Cells* **61**, 35-42 (2000).
24 Wells, A. F. *Structural inorganic chemistry*. (Oxford University Press, 2012).
25 Weller, M. T., Weber, O. J., Henry, P. F., Di Pumpo, A. M. & Hansen, T. C. Complete structure and cation orientation in the perovskite photovoltaic methylammonium lead iodide between 100 and 352 K. *Chemical Communications* **51**, 4180-4183 (2015).
26 Stoumpos, C. C., Malliakas, C. D. & Kanatzidis, M. G. Semiconducting tin and lead iodide perovskites with organic cations: phase transitions, high mobilities, and near-infrared photoluminescent properties. *Inorganic chemistry* **52**, 9019-9038 (2013).
27 Goldschmidt, V. M. Die gesetze der krystallochemie. *Naturwissenschaften* **14**, 477-485 (1926).
28 Poglitsch, A. & Weber, D. Dynamic disorder in methylammoniumtrihalogenoplumbates (II) observed by millimeter-wave spectroscopy. *The Journal of chemical physics* **87**, 6373-6378 (1987).
29 Weber, D. CH3NH3PbX3, ein Pb (II)-system mit kubischer Perowskitstruktur/CH3NH3PbX3, a Pb (II)-system with cubic perovskite structure. *Zeitschrift für Naturforschung B* **33**, 1443-1445 (1978).
30 Zhou, Z. *et al.* Methylamine-Gas-Induced Defect-Healing Behavior of CH3NH3PbI3 Thin Films for Perovskite Solar Cells. *Angewandte Chemie International Edition* **54**, 9705-9709 (2015).
31 Nie, W. *et al.* High-efficiency solution-processed perovskite solar cells with millimeter-scale grains. *Science* **347**, 522-525 (2015).
32 Zhou, Y. *et al.* Room-temperature crystallization of hybrid-perovskite thin films via solvent–solvent extraction for high-performance solar cells. *Journal of Materials Chemistry A* **3**, 8178-8184 (2015).
33 O'regan, B. & Grfitzeli, M. A low-cost, high-efficiency solar cell based on dye-sensitized. *nature* **353**, 737-740 (1991).
34 Hardin, B. E., Snaith, H. J. & McGehee, M. D. The renaissance of dye-sensitized solar cells. *Nature Photonics* **6**, 162-169 (2012).
35 Snaith, H. J. & Schmidt-Mende, L. Advances in liquid-electrolyte and solid-state dye-sensitized solar cells. *Advanced Materials* **19**, 3187-3200 (2007).
36 Snaith, H. J., Stavrinadis, A., Docampo, P. & Watt, A. A. Lead-sulphide quantum-dot sensitization of tin oxide based hybrid solar cells. *Solar Energy* **85**, 1283-1290 (2011).
37 Kamat, P. V. Quantum dot solar cells. The next big thing in photovoltaics. *The journal of physical chemistry letters* **4**, 908-918 (2013).
38 Kojima, A., Teshima, K., Shirai, Y. & Miyasaka, T. Organometal halide perovskites as visible-light sensitizers for photovoltaic cells. *Journal of the American Chemical Society* **131**, 6050-6051 (2009).
39 Im, J.-H., Lee, C.-R., Lee, J.-W., Park, S.-W. & Park, N.-G. 6.5% efficient perovskite quantum-dot-sensitized solar cell. *Nanoscale* **3**, 4088-4093 (2011).
40 Lee, M. M., Teuscher, J., Miyasaka, T., Murakami, T. N. & Snaith, H. J. Efficient hybrid solar cells based on meso-superstructured organometal halide perovskites. *Science* **338**, 643-647 (2012).
41 Kim, H.-S. *et al.* Lead iodide perovskite sensitized all-solid-state submicron thin film mesoscopic solar cell with efficiency exceeding 9%. *Scientific reports* **2**, 591 (2012).
42 Snaith, H. J. Perovskites: the emergence of a new era for low-cost, high-efficiency solar cells. *The Journal of Physical Chemistry Letters* **4**, 3623-3630 (2013).
43 Snaith, H. J. Estimating the maximum attainable efficiency in dye-sensitized solar cells. *Advanced Functional Materials* **20**, 13-19 (2010).

44 Kubo, W. *et al.* Quasi-solid-state dye-sensitized TiO2 solar cells: effective charge transport in mesoporous space filled with gel electrolytes containing iodide and iodine. *The Journal of Physical Chemistry B* **105**, 12809-12815 (2001).
45 Bach, U. *et al.* Solid-state dye-sensitized mesoporous TiO2 solar cells with high photon-to-electron conversion efficiencies. *Nature* **395**, 583-585 (1998).
46 Itzhaik, Y., Niitsoo, O., Page, M. & Hodes, G. Sb2S3-sensitized nanoporous TiO2 solar cells. *The Journal of Physical Chemistry C* **113**, 4254-4256 (2009).
47 Lévy-Clément, C., Tena-Zaera, R., Ryan, M. A., Katty, A. & Hodes, G. CdSe-Sensitized p-CuSCN/Nanowire n-ZnO Heterojunctions. *Advanced Materials* **17**, 1512-1515 (2005).
48 Kim, H.-S., Im, S. H. & Park, N.-G. Organolead halide perovskite: new horizons in solar cell research. *The Journal of Physical Chemistry C* **118**, 5615-5625 (2014).
49 Xing, G. *et al.* Low-temperature solution-processed wavelength-tunable perovskites for lasing. *Nature materials* **13**, 476-480 (2014).
50 Singh, S. P. & Nagarjuna, P. Organometal halide perovskites as useful materials in sensitized solar cells. *Dalton Transactions* **43**, 5247-5251 (2014).
51 Gao, P., Grätzel, M. & Nazeeruddin, M. K. Organohalide lead perovskites for photovoltaic applications. *Energy & Environmental Science* **7**, 2448-2463 (2014).
52 Berhe, T. A. *et al.* Organometal halide perovskite solar cells: degradation and stability. *Energy & Environmental Science* **9**, 323-356 (2016).
53 Jeng, J. Y. *et al.* CH3NH3PbI3 Perovskite/Fullerene Planar-Heterojunction Hybrid Solar Cells. *Advanced Materials* **25**, 3727-3732 (2013).
54 Malinkiewicz, O. *et al.* Metal-Oxide-Free Methylammonium Lead Iodide Perovskite-Based Solar Cells: the Influence of Organic Charge Transport Layers. *Advanced Energy Materials* **4** (2014).
55 Bisquert, J. Chemical diffusion coefficient of electrons in nanostructured semiconductor electrodes and dye-sensitized solar cells. *The Journal of Physical Chemistry B* **108**, 2323-2332 (2004).
56 Snaith, H. J. & Grätzel, M. Electron and Hole Transport through Mesoporous TiO2 Infiltrated with Spiro-MeOTAD. *Advanced Materials* **19**, 3643-3647 (2007).
57 Zhu, K., Neale, N. R., Halverson, A. F., Kim, J. Y. & Frank, A. J. Effects of annealing temperature on the charge-collection and light-harvesting properties of TiO2 nanotube-based dye-sensitized solar cells. *The Journal of Physical Chemistry C* **114**, 13433-13441 (2010).
58 Yang, W. S. *et al.* High-performance photovoltaic perovskite layers fabricated through intramolecular exchange. *Science* **348**, 1234-1237 (2015).
59 Brenner, T. M., Egger, D. A., Kronik, L., Hodes, G. & Cahen, D. Hybrid organic—inorganic perovskites: low-cost semiconductors with intriguing charge-transport properties. *Nature Reviews Materials* **1**, 15007 (2016).
60 Jenny, D., Loferski, J. & Rappaport, P. Photovoltaic effect in GaAs p− n junctions and solar energy conversion. *Physical Review* **101**, 1208 (1956).
61 De Wolf, S. *et al.* Organometallic halide perovskites: sharp optical absorption edge and its relation to photovoltaic performance. *The Journal of Physical Chemistry Letters* **5**, 1035-1039 (2014).
62 Kirchartz, T. & Nelson, J. in *Multiscale Modelling of Organic and Hybrid Photovoltaics* 279-324 (Springer, 2013).
63 Mosconi, E., Ronca, E. & De Angelis, F. First-principles investigation of the TiO2/organohalide perovskites interface: The role of interfacial chlorine. *The journal of physical chemistry letters* **5**, 2619-2625 (2014).
64 Menéndez-Proupin, E., Palacios, P., Wahnón, P. & Conesa, J. Self-consistent relativistic band structure of the CH 3 NH 3 PbI 3 perovskite. *Physical Review B* **90**, 045207 (2014).

65 Sadhanala, A. *et al.* Preparation of single-phase films of CH3NH3Pb (I1–x Br x) 3 with sharp optical band edges. *The journal of physical chemistry letters* **5**, 2501-2505 (2014).
66 Sze, S. M. & Ng, K. K. *Physics of semiconductor devices*. (John wiley & sons, 2006).
67 Oga, H., Saeki, A., Ogomi, Y., Hayase, S. & Seki, S. Improved understanding of the electronic and energetic landscapes of perovskite solar cells: high local charge carrier mobility, reduced recombination, and extremely shallow traps. *Journal of the American Chemical Society* **136**, 13818-13825 (2014).
68 Wehrenfennig, C., Eperon, G. E., Johnston, M. B., Snaith, H. J. & Herz, L. M. High charge carrier mobilities and lifetimes in organolead trihalide perovskites. *Advanced materials* **26**, 1584-1589 (2014).
69 Stranks, S. D. *et al.* Electron-hole diffusion lengths exceeding 1 micrometer in an organometal trihalide perovskite absorber. *Science* **342**, 341-344 (2013).
70 Shi, D. *et al.* Low trap-state density and long carrier diffusion in organolead trihalide perovskite single crystals. *Science* **347**, 519-522 (2015).
71 Zhang, M. *et al.* Composition-dependent photoluminescence intensity and prolonged recombination lifetime of perovskite CH 3 NH 3 PbBr 3− x Cl x films. *Chemical Communications* **50**, 11727-11730 (2014).
72 Brittman, S., Adhyaksa, G. W. P. & Garnett, E. C. The expanding world of hybrid perovskites: materials properties and emerging applications. *MRS communications* **5**, 7-26 (2015).
73 Shin, S. S. *et al.* Colloidally prepared La-doped BaSnO3 electrodes for efficient, photostable perovskite solar cells. *Science* **356**, 167-171 (2017).
74 Egger, D. A., Edri, E., Cahen, D. & Hodes, G. (ACS Publications, 2015).
75 Xiao, Z. *et al.* Giant switchable photovoltaic effect in organometal trihalide perovskite devices. *Nature materials* **14**, 193-198 (2015).
76 Yuan, Y. *et al.* Photovoltaic switching mechanism in lateral structure hybrid perovskite solar cells. *Advanced Energy Materials* **5** (2015).
77 Leijtens, T. *et al.* Overcoming ultraviolet light instability of sensitized TiO2 with meso-superstructured organometal tri-halide perovskite solar cells. *Nature communications* **4** (2013).
78 Misra, R. K. *et al.* Temperature-and component-dependent degradation of perovskite photovoltaic materials under concentrated sunlight. *The journal of physical chemistry letters* **6**, 326-330 (2015).
79 Eperon, G. E., Burlakov, V. M., Docampo, P., Goriely, A. & Snaith, H. J. Morphological Control for High Performance, Solution-Processed Planar Heterojunction Perovskite Solar Cells. *Advanced Functional Materials* **24**, 151-157 (2014).
80 Tress, W. *et al.* Understanding the rate-dependent J–V hysteresis, slow time component, and aging in CH 3 NH 3 PbI 3 perovskite solar cells: the role of a compensated electric field. *Energy & Environmental Science* **8**, 995-1004 (2015).
81 Carrillo, J. *et al.* Ionic reactivity at contacts and aging of methylammonium lead triiodide perovskite solar cells. *Advanced Energy Materials* **6** (2016).
82 Domanski, K. *et al.* Not All That Glitters is Gold: Metal Migration-Induced Degradation in Perovskite Solar Cells. *ACS nano* (2016).
83 Supasai, T., Rujisamphan, N., Ullrich, K., Chemseddine, A. & Dittrich, T. Formation of a passivating CH3NH3PbI3/PbI2 interface during moderate heating of CH3NH3PbI3 layers. *Applied Physics Letters* **103**, 183906 (2013).
84 Heo, J. H. *et al.* Efficient inorganic-organic hybrid heterojunction solar cells containing perovskite compound and polymeric hole conductors. *Nature photonics* **7**, 486-491 (2013).
85 Yu, H. *et al.* The Role of Chlorine in the Formation Process of "CH3NH3PbI3-xClx" Perovskite. *Advanced Functional Materials* **24**, 7102-7108 (2014).

86 Dualeh, A. *et al.* Effect of annealing temperature on film morphology of organic–inorganic hybrid pervoskite solid-state solar cells. *Advanced Functional Materials* **24**, 3250-3258 (2014).
87 Seemann, A., Egelhaaf, H.-J., Brabec, C. J. & Hauch, J. A. Influence of oxygen on semi-transparent organic solar cells with gas permeable electrodes. *Organic Electronics* **10**, 1424-1428 (2009).
88 Reese, M. O. *et al.* Photoinduced degradation of polymer and polymer–fullerene active layers: experiment and theory. *Advanced Functional Materials* **20**, 3476-3483 (2010).
89 Manceau, M. *et al.* Effects of long-term UV–visible light irradiation in the absence of oxygen on P3HT and P3HT: PCBM blend. *Solar Energy Materials and Solar Cells* **94**, 1572-1577 (2010).
90 Krebs, F. C. & Norrman, K. Analysis of the failure mechanism for a stable organic photovoltaic during 10 000 h of testing. *Progress in Photovoltaics: Research and Applications* **15**, 697-712 (2007).
91 Carter, E., Carley, A. F. & Murphy, D. M. Evidence for O2-radical stabilization at surface oxygen vacancies on polycrystalline TiO2. *The Journal of Physical Chemistry C* **111**, 10630-10638 (2007).
92 Al-Dmour, H. & Taylor, D. Revisiting the origin of open circuit voltage in nanocrystalline-TiO 2/polymer heterojunction solar cells. *Applied Physics Letters* **94**, 148 (2009).
93 Iwamoto, M., Yoda, Y., Egashira, M. & Seiyama, T. Study of metal oxide catalysts by temperature programmed desorption. 1. Chemisorption of oxygen on nickel oxide. *The Journal of Physical Chemistry* **80**, 1989-1994 (1976).
94 Pathak, S. K. *et al.* Performance and stability enhancement of dye-sensitized and Perovskite solar cells by Al doping of TiO2. *Advanced Functional Materials* **24**, 6046-6055 (2014).
95 Pathak, S. K. *et al.* Towards Long-Term Photostability of Solid-State Dye Sensitized Solar Cells. *Advanced Energy Materials* **4** (2014).
96 Schwanitz, K., Weiler, U., Hunger, R., Mayer, T. & Jaegermann, W. Synchrotron-induced photoelectron spectroscopy of the dye-sensitized nanocrystalline TiO2/electrolyte interface: band gap states and their interaction with dye and solvent molecules. *The Journal of Physical Chemistry C* **111**, 849-854 (2007).
97 Schwanitz, K., Mankel, E., Hunger, R., Mayer, T. & Jaegermann, W. Photoelectron Spectroscopy at the Solid–Liquid Interface of Dye–Sensitized Solar Cells: Unique Experiments with the Solid–Liquid Interface Analysis System SoLiAS at BESSY. *CHIMIA International Journal for Chemistry* **61**, 796-800 (2007).
98 Nakamura, I. *et al.* Role of oxygen vacancy in the plasma-treated TiO 2 photocatalyst with visible light activity for NO removal. *Journal of Molecular Catalysis A: Chemical* **161**, 205-212 (2000).
99 Habisreutinger, S. N. *et al.* Carbon nanotube/polymer composites as a highly stable hole collection layer in perovskite solar cells. *Nano letters* **14**, 5561-5568 (2014).
100 Smith, I. C., Hoke, E. T., Solis-Ibarra, D., McGehee, M. D. & Karunadasa, H. I. A layered hybrid perovskite solar-cell absorber with enhanced moisture stability. *Angewandte Chemie* **126**, 11414-11417 (2014).
101 You, J. *et al.* Moisture assisted perovskite film growth for high performance solar cells. *Applied Physics Letters* **105**, 183902 (2014).
102 Niu, G. *et al.* Study on the stability of CH 3 NH 3 PbI 3 films and the effect of post-modification by aluminum oxide in all-solid-state hybrid solar cells. *Journal of Materials Chemistry A* **2**, 705-710 (2014).
103 Dualeh, A., Gao, P., Seok, S. I., Nazeeruddin, M. K. & Grätzel, M. Thermal behavior of methylammonium lead-trihalide perovskite photovoltaic light harvesters. *Chemistry of Materials* **26**, 6160-6164 (2014).

104 Aharon, S., Dymshits, A., Rotem, A. & Etgar, L. Temperature dependence of hole conductor free formamidinium lead iodide perovskite based solar cells. *Journal of Materials Chemistry A* **3**, 9171-9178 (2015).
105 Unger, E. *et al.* Hysteresis and transient behavior in current–voltage measurements of hybrid-perovskite absorber solar cells. *Energy & Environmental Science* **7**, 3690-3698 (2014).
106 Ito, S., Tanaka, S., Manabe, K. & Nishino, H. Effects of surface blocking layer of Sb2S3 on nanocrystalline TiO2 for CH3NH3PbI3 perovskite solar cells. *The Journal of Physical Chemistry C* **118**, 16995-17000 (2014).
107 Dutta, P. & Horn, P. Low-frequency fluctuations in solids: 1 f noise. *Reviews of Modern physics* **53**, 497 (1981).
108 Hooge, F. Discussion of recent experiments on 1/ƒ noise. *Physica* **60**, 130-144 (1972).
109 Hooge, F., Kleinpenning, T. & Vandamme, L. Experimental studies on 1/f noise. *Reports on progress in Physics* **44**, 479 (1981).
110 Vandamme, L., Li, X. & Rigaud, D. 1/f noise in MOS devices, mobility or number fluctuations? *IEEE Transactions on Electron Devices* **41**, 1936-1945 (1994).
111 Vandamme, L. K. & Hooge, F. What do we certainly know about noise in MOSTs? *IEEE transactions on electron devices* **55**, 3070-3085 (2008).
112 Balandin, A., Wang, K., Svizhenko, A. & Bandyopadhyay, S. The fundamental 1/f noise and the Hooge parameter in semiconductor quantum wires. *IEEE Transactions on Electron Devices* **46**, 1240-1244 (1999).
113 Balandin, A. A. Low-frequency 1/f noise in graphene devices. *Nature nanotechnology* **8**, 549-555 (2013).
114 Harsh, R. & Narayan, K. Noise spectroscopy of polymer transistors. *Journal of Applied Physics* **118**, 205502 (2015).
115 Landi, G., Barone, C., Mauro, C., Neitzert, H. & Pagano, S. A noise model for the evaluation of defect states in solar cells. *Scientific Reports* **6** (2016).
116 Katsu, H., Kawasugi, Y., Yamada, R. & Tada, H. in *Noise and Fluctuations (ICNF), 2011 21st International Conference on.* 77-79 (IEEE).
117 Bag, M., Vidhyadhiraja, N. & Narayan, K. Fluctuations in photocurrent of bulk heterojunction polymer solar cells—A valuable tool to understand microscopic and degradation processes. *Applied Physics Letters* **101**, 043903 (2012).
118 Barone, C. *et al.* Unravelling the low-temperature metastable state in perovskite solar cells by noise spectroscopy. *Scientific Reports* **6** (2016).
119 Lee, B. *et al.* Evaluating the Optoelectronic Quality of Hybrid Perovskites by Conductive Atomic Force Microscopy with Noise Spectroscopy. *ACS Applied Materials & Interfaces* **8**, 30985-30991 (2016).
120 Hassibi, A., Navid, R., Dutton, R. W. & Lee, T. H. Comprehensive study of noise processes in electrode electrolyte interfaces. *Journal of applied physics* **96**, 1074-1082 (2004).
121 Hooge, F. 1/f noise sources. *IEEE Transactions on Electron Devices* **41**, 1926-1935 (1994).
122 Raychaudhuri, A. Measurement of 1/f noise and its application in materials science. *Current opinion in solid state and materials science* **6**, 67-85 (2002).
123 Shockley, W. & Read Jr, W. Statistics of the recombinations of holes and electrons. *Physical review* **87**, 835 (1952).
124 Van Der Ziel, A. Noise in solid-state devices and lasers. *Proceedings of the IEEE* **58**, 1178-1206 (1970).
125 Sah, C.-T. The equivalent circuit model in solid-state electronics—Part I: The single energy level defect centers. *Proceedings of the IEEE* **55**, 654-671 (1967).
126 Van der Ziel, A. Unified presentation of 1/f noise in electron devices: fundamental 1/f noise sources. *Proceedings of the IEEE* **76**, 233-258 (1988).
127 Amberiadis, K., Grimes, R. W. & Kump, M. R. GR noise spectra of semiconductors and insulators with various trap distributions. *Solid-state electronics* **33**, 975-977 (1990).

128 Niu, G., Guo, X. & Wang, L. Review of recent progress in chemical stability of perovskite solar cells. *Journal of Materials Chemistry A* **3**, 8970-8980 (2015).
129 van den Berg, R., de Vos, A. & de Goede, J. Electrical resistivity fluctuations in aqueous KCl solutions. *Physics Letters A* **84**, 433-434 (1981).
130 de Vos, A., van den Berg, R. & de Goede, J. Resistivity fluctuations in aqueous CuSO4 solutions. *Physics Letters A* **102**, 320-322 (1984).
131 Musha, T. & Sugita, K. 1/f Conductance fluctuations in aqueous ionic solution. *Journal of the Physical Society of Japan* **51**, 3820-3825 (1982).
132 Fleischmann, M. & Oldfield, J. Generation-recombination noise in weak electrolytes. *Journal of Electroanalytical Chemistry and Interfacial Electrochemistry* **27**, 207-218 (1970).
133 Molski, A. & Dutkiewicz, E. Conductivity of water-in-oil microemulsions: Fluctuations from the charge generation-recombination equilibrium. *Colloid & Polymer Science* **271**, 1177-1182 (1993).
134 Barker, G. Noise connected with electrode processes. *Journal of Electroanalytical Chemistry and Interfacial Electrochemistry* **21**, 127-136 (1969).
135 Jayaweera, P., Pitigala, P., Seneviratne, M., Perera, A. & Tennakone, K. 1/f noise in dye-sensitized solar cells and NIR photon detectors. *Infrared physics & technology* **50**, 270-273 (2007).
136 Snaith, H. J. *et al.* Anomalous hysteresis in perovskite solar cells. *The journal of physical chemistry letters* **5**, 1511-1515 (2014).
137 Zhang, Y. *et al.* Charge selective contacts, mobile ions and anomalous hysteresis in organic–inorganic perovskite solar cells. *Materials Horizons* **2**, 315-322 (2015).
138 Zhao, Y. *et al.* Quantification of light-enhanced ionic transport in lead iodide perovskite thin films and its solar cell applications. (2016).
139 Calado, P. *et al.* Evidence for ion migration in hybrid perovskite solar cells with minimal hysteresis. *arXiv preprint arXiv:1606.00818* (2016).
140 Milotti, E. 1/f noise: a pedagogical review. *arXiv preprint physics/0204033* (2002).
141 Vandamme, L. Noise as a diagnostic tool for quality and reliability of electronic devices. *IEEE Transactions on Electron Devices* **41**, 2176-2187 (1994).
142 Chobola, Z. & Ibrahim, A. Noise and scanning by local illumination as reliability estimation for silicon solar cells. *Fluctuation and noise letters* **1**, L21-L26 (2001).
143 Hooge, F. & Vandamme, L. Lattice scattering causes 1/f noise. *Physics Letters A* **66**, 315-316 (1978).
144 Bertuccio, G., De Geronimo, G., Longoni, A. & Pullia, A. Low frequency gate current noise in high electron mobility transistors: experimental analysis. *IEEE electron device letters* **16**, 103-105 (1995).
145 Vandamme, L. K. Bulk and surface 1/f noise. *IEEE Transactions on Electron Devices* **36**, 987-992 (1989).
146 Škarvada, P. *et al.* 101420U-101420U-101427.
147 Fritzsche, H. Photo-induced structural changes associated with the Staebler-Wronski effect in hydrogenated amorphous silicon. *Solid state communications* **94**, 953-955 (1995).
148 Shao, Y., Xiao, Z., Bi, C., Yuan, Y. & Huang, J. Origin and elimination of photocurrent hysteresis by fullerene passivation in CH3NH3PbI3 planar heterojunction solar cells. *Nature communications* **5** (2014).
149 Duan, H.-S. *et al.* The identification and characterization of defect states in hybrid organic–inorganic perovskite photovoltaics. *Physical Chemistry Chemical Physics* **17**, 112-116 (2015).
150 Gonzalez-Pedro, V. *et al.* General working principles of CH3NH3PbX3 perovskite solar cells. *Nano letters* **14**, 888-893 (2014).
151 Jasenek, A., Rau, U., Nadenau, V. & Schock, H. Electronic properties of CuGaSe 2-based heterojunction solar cells. Part II. Defect spectroscopy. *Journal of Applied Physics* **87**, 594-602 (2000).

152 MacKenzie, R. C., Shuttle, C. G., Chabinyc, M. L. & Nelson, J. Extracting microscopic device parameters from transient photocurrent measurements of P3HT: PCBM solar cells. *Advanced Energy Materials* **2**, 662-669 (2012).
153 Byers, J. C., Ballantyne, S., Rodionov, K., Mann, A. & Semenikhin, O. Mechanism of recombination losses in bulk heterojunction P3HT: PCBM solar cells studied using intensity modulated photocurrent spectroscopy. *ACS applied materials & interfaces* **3**, 392-401 (2011).
154 Instruments, N. Labview. *Austin, TX* (2006).
155 Mathematica, W. Wolfram Research. *Inc., Champaign, Illinois* (2009).

Appendix A

Trap model for the photocurrent fluctuations in solar cells

1/f noise component originating from the amplitude *Var [I]* can be considered as the sum of a dark (*Var [I_{dark}]*) and a photo-indued (*Var [I_{ph}]*) contribution. The emission rate $e_{n,p}$ (s^{-1}) and capture coefficient $c_{n,p}$ ($cm^3 s^{-1}$) for the electrons and holes traps, influence the *Var [I_{dark}]* under dark and forward bias condition. Under illumination, these emission rates and capture coefficients change along with the density of filled traps. This results in an increase in the trap filling due to the process of carrier photogeneration. Filling of the traps continues until a point of saturation, wherein noise point of view, all the traps have been activated. In this condition, the contribution is dominant from the *Var [I_{ph}]*, hence noise larger than the background is obtained.

Generated photocurrent can be expressed as:

$$I_{ph} = \frac{q}{\tau_{eff}} Adn$$

Where q is the charge, n is the average density of excess charge carriers; A is the area of the sample and d is the sample thickness. Considering the SRH statistics, the resulting fraction of the filled fluctuating traps can be given as:

$$n_T = \frac{N_T e_n}{e_n + c_n n}$$

Further, the fraction of the filled recombination centers is:

$$n_{SRH} = \frac{N_T e_n}{c_n n + c_p N_A}$$

Where N_A is the concentration of the base doping, In the first equation, the fluctuating term is related to n, hence under the assumption of a binomial probability distribution, *Var [I_{ph}]* can be represented as:

$$Var[I_{ph}] = \left(\frac{q}{\tau_{eff}}\right)^2 \{Var[Adn_T] + Var\,[Adn_{SRH}]\}$$

Substituting equation A2 and A3 in equation A4 we get:

$$Var\,[I_{ph}] = \left(\frac{q}{\tau_{eff}}\right)^2 Ad \left[N_T \frac{n\frac{c_n}{e_n}}{\left(1 + n\frac{c_n}{e_n}\right)^2} + \frac{N_{SRH}}{N_A}\frac{c_n}{c_p}\frac{n}{\left(1 + \frac{n}{N_A}\frac{c_n}{c_p}\right)^2} \right]$$

Where c_n/c_p is the symmetric ratio and can be represented as 'k'.

If, I_o^{light} is interpreted as the threshold current for the saturation of the noise level and I_A takes into consideration the effect of recombination centers, then by definition:

$$I_o^{light} = \frac{q}{\tau_{eff}} Ad \frac{e_n}{c_n}$$

and

$$I_A = \frac{q}{\tau_{eff}} Ad \frac{A_n}{k}$$

equation A5 can be rewritten as:

$$Var\left[I_{ph}\right] = A_1 \frac{I_{ph}}{\left(1 + \frac{I_{ph}}{I_o^{light}}\right)^2} + A_2 \frac{I_{ph}}{\left(1 + \frac{I_{ph}}{I_A}\right)^2}$$

with $A_1 = \frac{q}{\tau_{eff}} N_T \frac{C_n}{e_n}$ and $A_2 = \frac{q}{\tau_{eff}} N_{SRH} \frac{k}{N_A}$

are representing the current fluctuations amplitudes related to the trapping and recombination mechanisms respectively. It can be seen that current fluctuations are the dominant noise source in the photovoltaic system.

Appendix B

MATLAB CODE

```
%% Details of the Code
% The PSD is computed by taking the time series file and splitting into
% frames of a specific frequency range, which can be different from the
% settings at DSA.Thus this program can change the lower and
% higher frequency ranges and is also good for average. Here the nfft is
% radix-2 and not in terms of resolution lines of the signal analyzer. But
the
% PSD is plotted in resolution lines which depend on the user input
% frequency range  values.
%% Code Created:
%% Author:
%% Molecular Electronics LAB

function DSA_PSD_zeta
format long
clear all

%% Initializing all parameters from the measurement settings

fres = 1600; %input('Enter the frequency resolution: ');
fspan = 3200;%input('Enter the frequency span of time capture in DSA(in
Hz): 12800');

sf = fspan*2.56;           %sampling frequency, sf does not depend on
                           % frequency resolution of DSA
%lowf = fspan/fres;     % lower frequency in DSA
T =6;%input('Enter the total duration of time capture:10 ');
%minf=1/T;               % lowest frequency possible
fl = 0.1;%input('Enter the lower frequency of plot: ');
fu =3200;%input('Enter the upper frequency of plot: ');
t = 1/fl;              % this should be the time capture for one PSD plot
Av= input('Enter the gain at preamplifier (only exponent): ');
Av=5*10^(4);
%% Calling the saved file into MatLAB
data_file = input('Enter the file name of time series capture: ','s');
fid = fopen(data_file,'r');
data= dlmread(data_file);
X= data(:,1);               % X has all the data points of time capture
X=X./(Av);
len_X= length(X);                                %len_X

%% Initialize parameters for obtaining PSD plots

len_T = T*sf;
len_t= t*sf;               %data points required for one PSD plot

nfft = 2.56*(fu/fl);%nfft


%(p=nextpow2(len_t);nfft=2^p;nfft) this line can also be used, but the only
```

```
% when the lower frequency ranges are similar or when more no.of  points
are
% taken for a particular freq span. Like 8192 data pts for 4096 fft pts

Navg = len_T/len_t;

x = zeros(len_t,1);
PSD_total = zeros(nfft,1);
psd_x = zeros(nfft,1);
ptr=0;

for i= 1:Navg

    x = X(1+ptr:len_t+ptr,1);

    psd_x = (fft(x,nfft))./(nfft);
    psd_x = abs(psd_x);
    psd_x = (psd_x.^2);


    PSD_total=PSD_total+psd_x;
    ptr= ptr+len_t;

end

freq=0:fl:fu;           % size(freq)
                        % freq(1,1:4)

PSD_total = PSD_total/Navg;

PSD_total=PSD_total(1:((nfft/2)+1),1);

PSD_total(2:end-1,1) = PSD_total(2:end-1,1);

% Do not multiply the elements of PSD with 2, even if the elements are the
same
% and are folded with respect to zero level. The correct form is taking
% only one side (or only one-half) along with the zero level.

PSD_plt=plot(log10(freq),log10(PSD_total(1:((nfft/2.56)+1))));
xlabel('Frequency (Hz)')
title(data_file)
%saveas(PSD_plt,sprintf('.bmp'))


%% Saving the PSD plot into text file
freq=transpose(freq);
PSD_write=zeros((fu/fl)+1,2);
PSD_write(:,1)= freq(:,1);
PSD_write(:,2)= PSD_total(1:((nfft/2.56)+1),1);

dlmwrite('PSD_dsa.txt',PSD_write,'precision',16,'delimiter',',','newline','
pc')
 fclose all
```

Appendix C

Spot-size measurement for local illumination photocurrent scanning

(a)

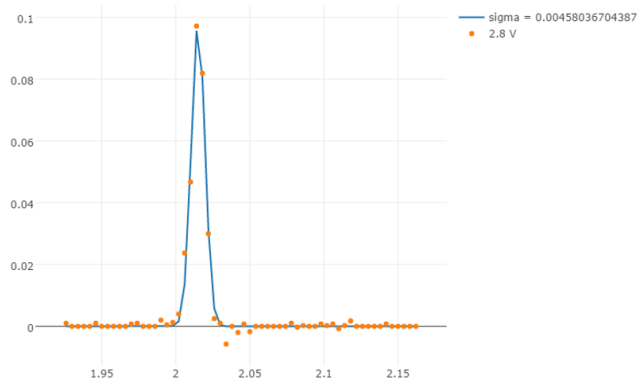

(b)

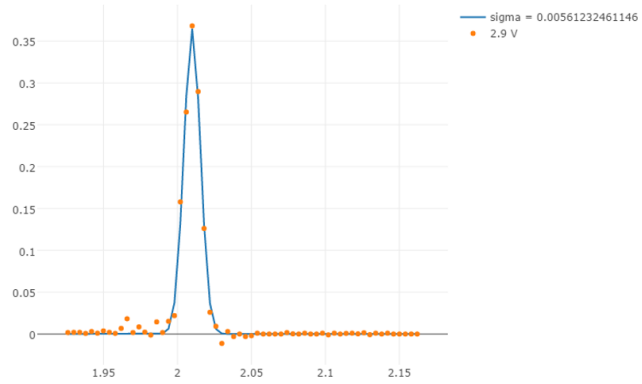

(c)

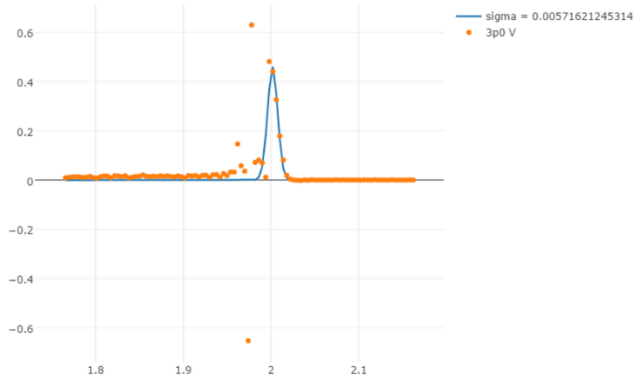

(d)

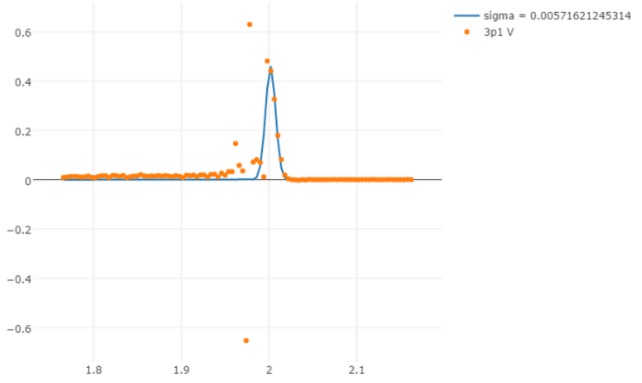

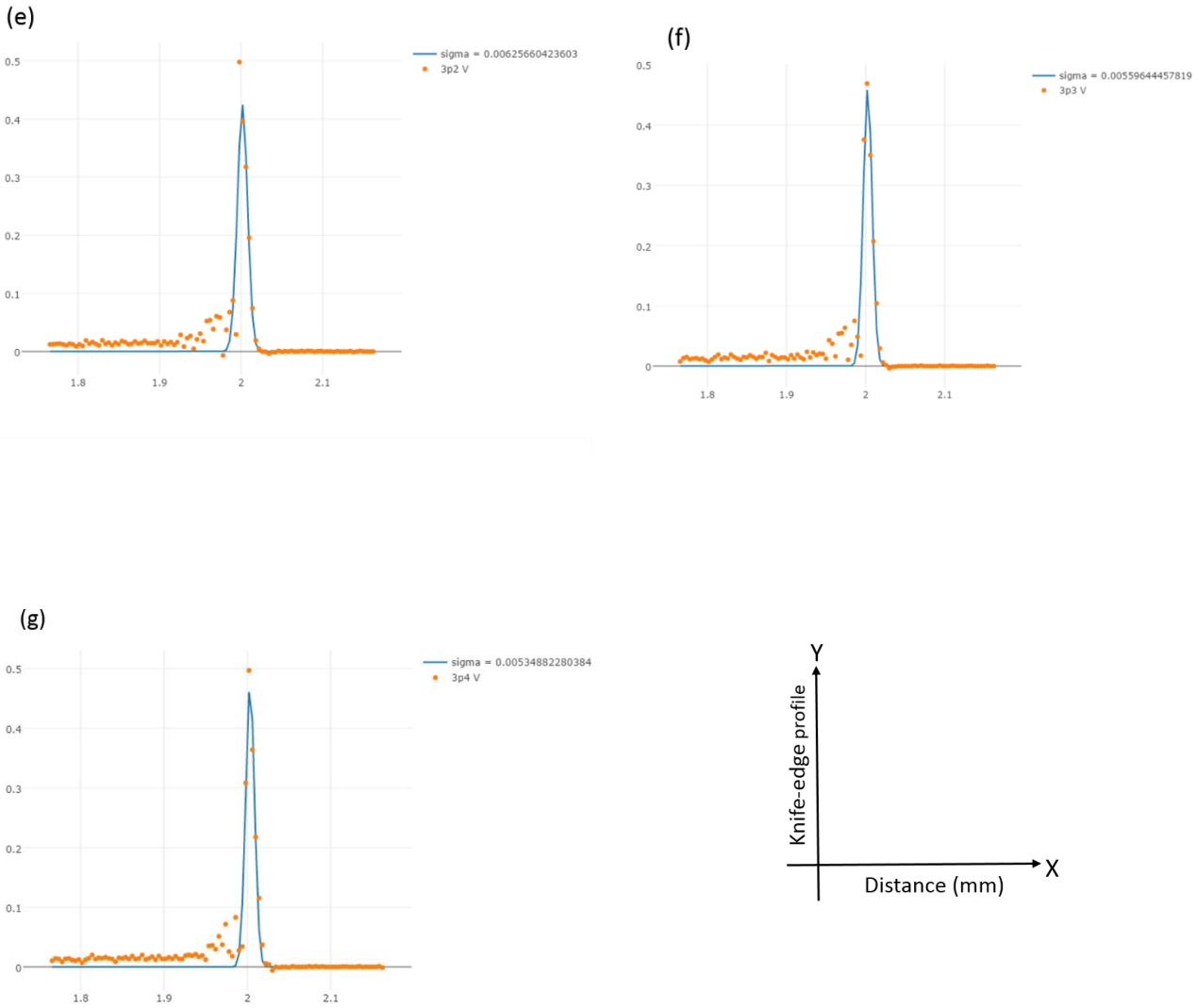

Figure A.C.1: *Spot size measurement using knife edge technique: Calculated values of spot-size (sigma) at different voltages ranging from 2.8- 3.4 V of supply to the laser (figure (a) to (g)).*

These calculations are made from the experimental data obtained using noise knife-edge technique. In this method, a sharp edge of the blade navigates perpendicular to the axes of the beam while recording photocurrent response as a function of position. Spot-size is obtained by the derivative of the profile and fitting Gaussian curve. The spot sizes found out in figure (a) to (g) are in the range of 5.5-6.25 μm, with the mean value of 5.7 μm.

Appendix D

Quantum efficiency of Perovskite cell

Spectral Response of Si

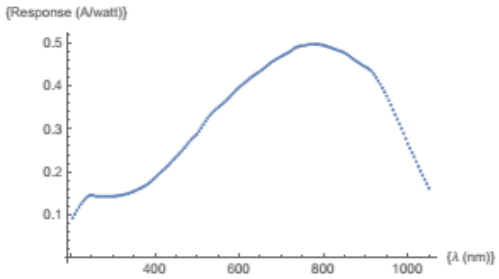

Si-SR at 620 ηη (A/Watt)

```
0.413351
```

Calculation & Plots

Directory

Formula

```
gainval = 10^3;
transdata =
 ReadData["Relay OFF  I-L of spotsize 3p0new objre_ _  .txt"];
(*photovoltage of the photodiode*)
inntensityval = 7.95 × 10^-3 / (gainval IntSi[620]);
Snumphoton = inntensityval / ((6.3 × 10^-34 * 3 × 10^8) / (620 × 10^-9));
Snumelectron = .094 * 10^-4 / (1.6 × 10^-19); (*gain = 10^-4*)
Seqe = Snumelectron / Snumphoton;
Max [Seqe]
0.931172
```

Distance vs PC data for sample

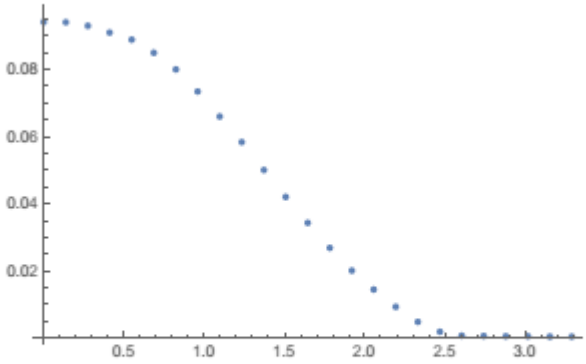

Max Quantum efficiency

```
0.933119
```

Appendix E

Miscellaneous

Page 50-figure 3.5-

The time series data of PbI_2 does not show any random telegraph noise. The power Spectral density of both G-R and RTS noise show Lorentzian feature. However, RTS noise show characteristic square like pulse in the time series.

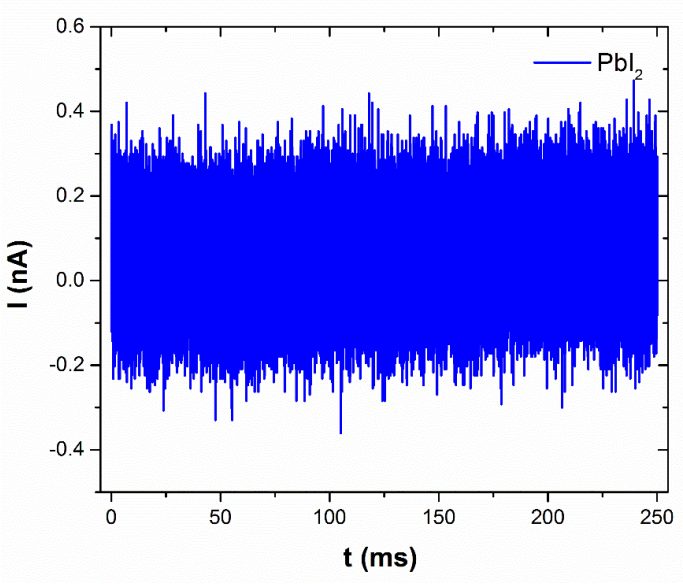

Time series plot of PbI_2

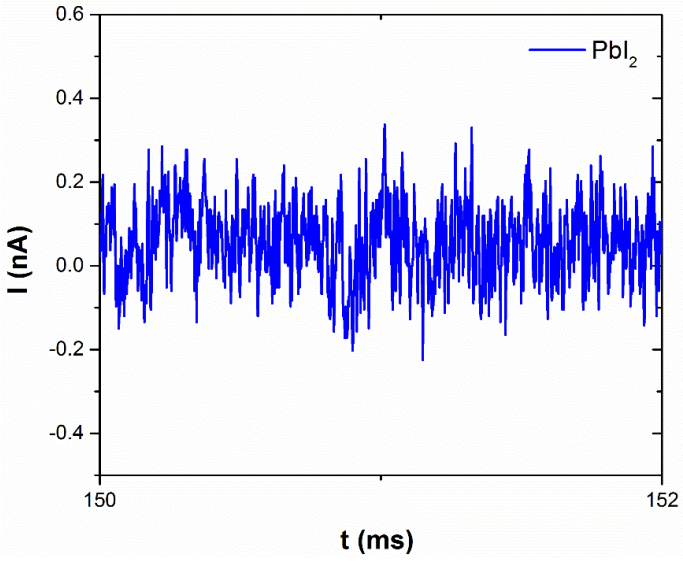

Figure showing zoomed-in time series. No RTS noise is observed.

Page 51, figure 3.7-

$1/f^{\alpha}$ fit for noise in DSSC (figure 3.7) for frequency < 1 kHz is shown below. The value of α obtained from fitting is 1.8.

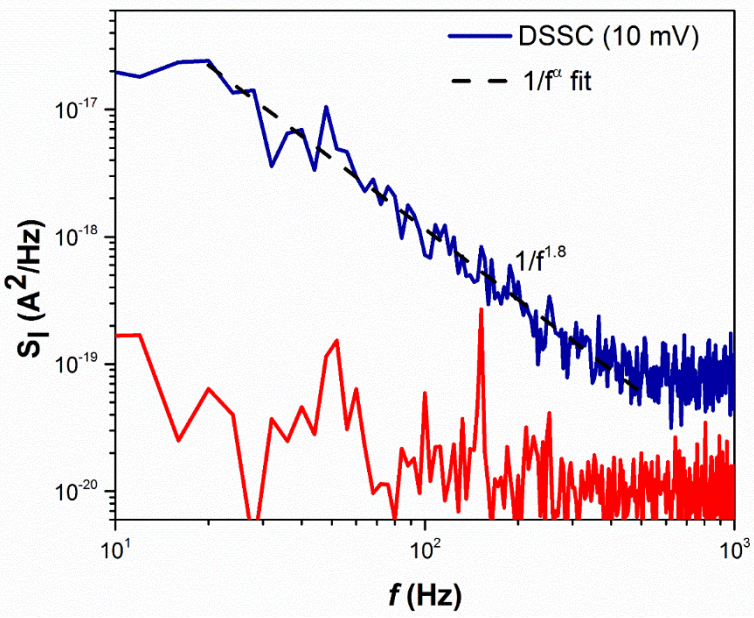

	A	B	C	D
1	Model	overf (User)		
2	Equation	a/x^b		
3	Reduced Chi-Sqr	7.65452E-37		
4	Adj. R-Square	0.91634		
5			Value	Standard Error
6	dsscwb51.2	a	5.5249E-15	1.27868E-15
7		b	1.84064	0.07131

(Result table from the fit for reference)

7. Page 52, figure 3.8

Log-normal like features as observed in the case of degraded DSSC. The peak of the log-normal has its peak in the range between 1 kHz to 10 kHz. From the fitting, it is centered around 2.5 kHz (and not 6.4 kHz).

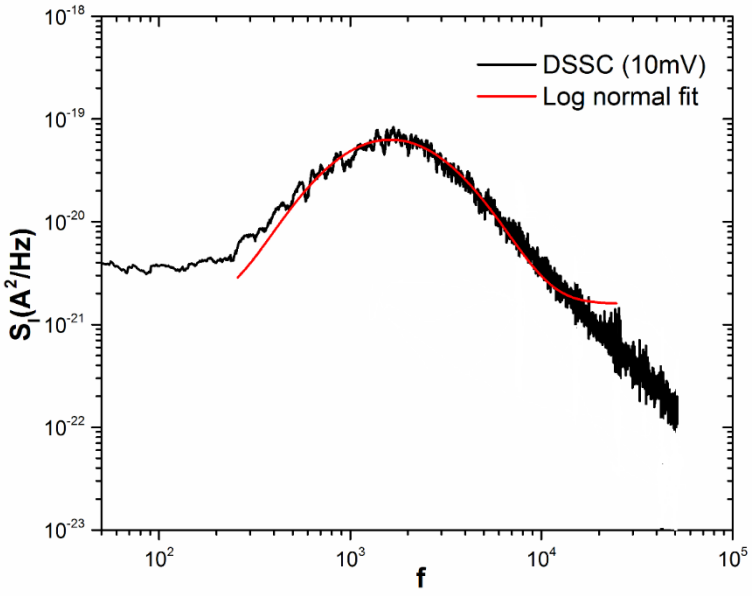

	A	B	C	D
1	Model	LogNormal		
2	Equation	y = y0 + A/(sqrt(2*PI)*w*x)*exp(-(ln(x/xc))^2/(2*w^2))		
3	Reduced Chi-Sqr	6.93039E-42		
4	Adj. R-Square	0.97381		
5			Value	Standard Error
6	Y	y0	1.59582E-21	2.21196E-23
7		xc	2507.81837	2.94513
8		w	0.66008	9.78862E-4
9		A	2.05285E-16	2.51261E-19

(Result table from the fit for reference)

Similar log-normal features are reported in the other systems including organic FETs and organic solar cells. (Reference 114 and 117 in the thesis).

Page63-for the data are shown in figure 4.2-

Variance analysis of the time series for the three different devices is shown in the table below. For each case, 327680 number of data points are used for calculating the net standard deviation. The obtained value of standard deviation for the device 1 is significantly higher than device 3.

(Report table for reference)

ANOVAOneWay (7/17/2017 17:30:38)

Descriptive Statistics

	N Analysis	N Missing	Mean	Standard Deviation	SE of Mean
D1	327680	327669	5.50697E-10	1.76986E-8	3.09182E-11
D2	327680	327669	-3.75248E-11	8.4206E-9	1.47102E-11
D3	327680	327669	5.88055E-10	2.79203E-9	4.87748E-12

One Way ANOVA

Overall ANOVA

	DF	Sum of Squares	Mean Square	F Value	Prob>F
Model	2	8.06913E-14	4.03456E-14	308.81215	0
Error	983037	1.28432E-10	1.30648E-16		
Total	983039	1.28512E-10			

Null Hypothesis: The means of all levels are equal.
Alternative Hypothesis: The means of one or more levels are different.
At the 0.05 level, the population means are significantly different.

Fit Statistics

	R-Square	Coeff Var	Root MSE	Data Mean
	6.27887E-4	31.13834	1.14301E-8	3.67076E-10

Page 80, section 4.8-

TAS experimental setup

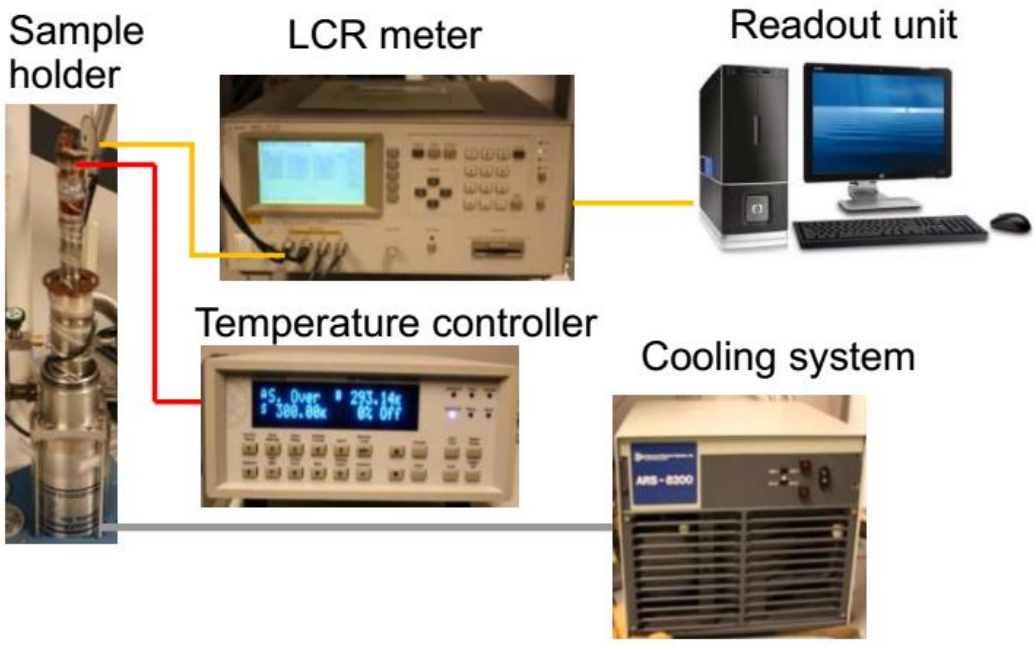

Typical experimental set-up for TAS measurements

Sources

1 http://www.semetrol.com/semetrol-tas.h

2 *Lasse-Vines_Electrical_Spectroscopy.pdf*

http://icds-2015.org/wp-content/uploads/sites/7/2015/07/ICDS2015_

Chapter 4: Normalization Procedure for the histograms

1. First, the y-axis of the time series data (fluctuation values) from all the data sets to be compared are selected together, and a histogram is plotted.

2. The obtained data in the histogram is further analyzed by adding distribution curves. The selected distribution in the current context is ‘normal’.

3.The above step results in two additional columns with distribution (in X-axis) and corresponding normal count (Y-axis). The X-axis represents the fluctuations, and due to normalization, a total number of counts in each case is identical. Now, depending upon the level of fluctuation normally distributed curves with different full-width half maxima (FWHM) can be obtained, and hence the results can be appreciated more conveniently.

(for reference: image showing the step 2)